

Towards Tighter Convex Relaxation of Mixed-Integer Programs: Leveraging Logic Network Flow for Task and Motion Planning

Journal Title
 XX(X):1–35
 ©The Author(s) 2016
 Reprints and permission:
 sagepub.co.uk/journalsPermissions.nav
 DOI: 10.1177/ToBeAssigned
 www.sagepub.com/

SAGE

Xuan Lin¹, Jiming Ren^{*1}, Yandong Luo^{*1}, Weijun Xie², and Ye Zhao¹

Abstract

This paper proposes an optimization-based task and motion planning framework, named “Logic Network Flow,” that integrates temporal logic specifications into mixed-integer programs for efficient robot planning. Inspired by the Graph-of-Convex-Sets formulation, temporal predicates are encoded as polyhedron constraints on each edge of a network flow model, instead of as constraints between nodes in traditional Logic Tree formulations. We further propose a network-flow-based Fourier-Motzkin elimination procedure that removes continuous flow variables while preserving convex relaxation tightness, leading to provably tighter convex relaxations and fewer constraints than Logic Tree formulations. For temporal logic motion planning with piecewise-affine dynamic systems, comprehensive experiments across vehicle routing, multi-robot coordination, and temporal logic control on dynamical systems using point mass and linear inverted pendulum models demonstrate computational speedups of up to several orders of magnitude. Hardware demonstrations with quadrupedal robots validate real-time replanning capabilities under dynamically changing environmental conditions. The project website is at <https://logictnetworkflow.github.io/>.

Keywords

Task and motion planning, temporal logic, mixed-integer programming, graph-of-convex-sets

1 Introduction

Task and motion planning (TAMP) with temporal logic specifications provides formal guarantees for robot motion plan safety and task completion (Plaku and Karaman 2016; Zhao et al. 2024; Li et al. 2021; He et al. 2015; Shamsah et al. 2023). Temporal logics — including Linear Temporal Logic (LTL), Metric Temporal Logic (MTL), and Signal Temporal Logic (STL) — offer a rich formal language for specifying complex robotic tasks, particularly when objectives extend beyond reaching predefined goal locations. LTL specifications are typically addressed through automata-based approaches, whereas MTL and STL constraints are formulated as mixed-integer linear programs (MILPs) (Cardona et al. 2023a; Sun et al. 2022). However, motion planning under temporal logic constraints remains computationally intractable in theory due to its NP-hard nature. In practice, MILP solvers, *e.g.*, via Branch-and-Bound (B&B), frequently solve such problems within a reasonable time, although they still retain worst-case exponential complexity. Despite numerous efforts to improve computational efficiency (Kurtz and Lin 2021, 2022), solving realistically large temporal logic planning problems often requires minutes or even hours, rendering them impractical for real-time robotics applications.

In this paper, we present a novel optimization formulation named “Logic Network Flow (LNF).” Inspired by the Graph-of-Convex-Sets (GCS) formulation (Marcucci 2024), we transform temporal logic specifications into network flow constraints to achieve tighter convex relaxations. Compared to the conventional Logic Tree (LT) approaches (Wolff

et al. 2014; Raman et al. 2014), which place temporal logic predicates at leaf nodes of a tree structure, the novelty of LNF lies in its usage of flow conservation constraints to correlate the predicates placed on the edges of a network flow.

Furthermore, we propose a network-flow-based Fourier-Motzkin procedure that eliminates flow variables, replacing them with a series of inequality constraints that provably tighten the convex relaxations compared to the LT formulations. This effectively projects the original formulation onto a lower-dimensional space, leading to our final formulation that maintains tighter convex relaxations without introducing additional variables. This is in contrast with the GCS formulation (Marcucci 2024), which achieves tighter convex relaxations at the expense of introducing additional variables compared to baseline formulations.

Through achieving tighter convex relaxations without introducing additional variables, our formulation demonstrates better computational performance in the B&B process and faster discovery of better incumbent solutions with computational speedups of up to several orders of magnitude compared to the benchmark methods. In addition, via integrating LNF with dynamic systems, our framework

¹George W. Woodruff School of Mechanical Engineering, Georgia Institute of Technology, USA

²Milton Stewart School of Industrial and Systems Engineering, Georgia Institute of Technology, USA

Corresponding author:

Ye Zhao, Georgia Institute of Technology, Atlanta, GA 30332, USA.
 Email: yezhao@gatech.edu

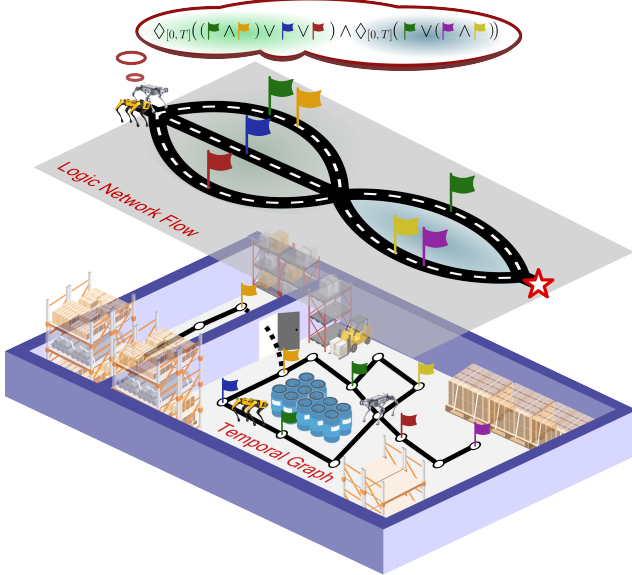


Figure 1. Conceptual illustration of multi-robot coordination in a factory warehouse using Logic Network Flow (LNF). The LNF representation of a conjunctive-disjunctive temporal logic specification is visualized at the top, with colored flags indicating different predicates on the LNF edges. Two quadrupedal robots navigate through the warehouse, visualized at the bottom, with the underlying temporal graph overlaid on the factory floor. Flags on the temporal graph indicate locations where specific task predicates are satisfied, showing the correspondence between the logic specification and physical locations.

offers greater flexibility than traditional motion planning approaches such as (Kuindersma et al. 2016; Marcucci et al. 2023; Lin et al. 2019), which typically require predefined goal states. Instead, our formulation synthesizes motion plans directly from temporal logic specifications, allowing behaviors that cannot be expressed as simply reaching fixed destinations, while still accommodating complex dynamics such as Piecewise Affine (PWA) systems (Sontag 1981).

We evaluate our formulation by comparing it against the standard LT approach for temporal logic motion planning integrated with PWA systems, as reviewed by (Belta and Sadraddini 2019). Specifically, we experiment on robotics problems that often go beyond the simple examples demonstrated in prior temporal logic planning literature, including Vehicle Routing Problems with Time Windows (VRPTW) for multi-robot coordination (Karaman and Frazzoli 2008), optimal motion planning under temporal logic specifications using point mass (Belta and Sadraddini 2019) and linear inverted pendulum models (Gu et al. 2024), and multi-robot search-and-rescue scenarios. The formulation is further validated through hardware experiments with quadrupedal robots demonstrating real-time replanning capabilities under dynamically changing environmental conditions.

Our main contributions are summarized as:

1. A novel optimization formulation, LNF, that provides provably tighter convex relaxations and fewer constraints compared to existing LT approaches, resulting in computational speedups up to orders of magnitude.
2. A network-flow-based Fourier-Motzkin elimination procedure that reduces the number of continuous variables and constraints for our temporal logic

formulations, while being applicable to broader GCS formulations.

3. Methods for integrating LNF with the general class of PWA dynamical systems, including specialized discrete graph formulations.
4. Extensive experiments to validate computational speed advantages in various robotic systems formulated as PWA dynamical systems, as well as hardware demonstrations using quadrupedal robots.

A conference version of this work is presented in (Lin et al. 2025). The current article significantly advances the original paper in several critical aspects. First, we introduce a network-flow-based Fourier-Motzkin elimination procedure that substantially improves computational efficiency by reducing the number of variables and constraints. Second, we extend the framework to handle the general class of PWA dynamical systems under temporal logic constraints, while maintaining the Dynamic Network Flow (DNF) formulation as a specialized formulation for planning on Temporal Graphs. Third, we provide rigorous theoretical analysis including formal proofs that our LNF formulation achieves tighter convex relaxations compared to the LT formulations, as well as proofs of soundness and completeness. Fourth, we provide extensive additional experiments on a variety of systems.

The remainder of this paper is organized as follows. Section 2 reviews prior work on motion planning under temporal logic constraints. Section 3 presents the mathematical preliminaries for formulating temporal logic constraints into MILPs. Section 4 introduces our LNF formulation as well as the network-flow-based Fourier-Motzkin elimination procedure. Section 5 describes general approaches for integrating LNF with PWA systems as well as specialized formulations using DNF. Section 6 presents computational results and experimental validation through simulations and hardware demonstrations. We conclude in Section 8 with a discussion of limitations and future work.

2 Related Work

2.1 Automata-based Methods for Temporal Logic Planning

Originating in software verification (Baier and Katoen 2008), formal methods based on temporal logic provide mathematical guarantees of the correctness of complex task specifications. A range of robotic studies have therefore leveraged temporal-logic-based methods for TAMP, such as control synthesis over dynamic systems (Belta et al. 2017), multi-agent coordination (Kloetzer and Belta 2009), and human-robot interaction (Kress-Gazit et al. 2021).

Automaton construction is a common approach to synthesize the reachability set of a robot to find feasible motion plans that satisfy temporal-logic specifications, where the specification is converted to a finite state machine featuring the actions to satisfy the logical requirements (Gastin and Oddoux 2001). However, building automata leads to significant computational costs, with the automaton size growing exponentially as the specification becomes more complex (Wolff et al. 2014). This scalability

issue becomes particularly challenging for large-scale robotic systems, motivating dedicated algorithms such as (Kantaros and Zavlanos 2020). When limited to a fragment of the LTL specifications, the satisfiability of temporal logic games can be verified in polynomial time complexity with respect to the problem size using reactive GR(1) synthesis (Piterman et al. 2006; Kress-Gazit et al. 2009; Liu et al. 2013), and when satisfiable, the corresponding automaton is constructed. However, the resultant automaton size remains prohibitively large for complex systems and specifications (Liu et al. 2013). While automata-based frameworks focus primarily on finding feasible solutions, researchers have extended them to achieve optimality (Ren et al. 2024; Wolff et al. 2012; Smith et al. 2011; Ulusoy et al. 2013). These methods typically struggle with complex specifications or high-dimensional systems. To address these challenges, Kurtz and Lin (Kurtz and Lin 2023) cast LTL motion planning as a shortest path problem in a GCS, enabling efficient solutions through convex optimization. Finally, these works focus on MTL and STL specifications, whereas generating automata for MTL and STL remains challenging (Brihaye et al. 2017; Raman et al. 2015; Belta and Sadraddini 2019). In contrast, our framework does not require building automata, but directly encodes the logic specifications into a unified optimization formulation, eliminating the exponential growth in representation size of automata approaches.

2.2 Optimization-based Methods for Temporal Logic Planning

Optimization-based methods offer an alternative approach to handling temporal logic specifications. Rather than constructing automata, optimization-based techniques directly encode temporal logic constraints into mathematical programs (Kurtz and Lin 2022; Belta and Sadraddini 2019; Raman et al. 2014; Wolff et al. 2014), and synthesize with underlying dynamic systems using a unified formulation to achieve both logical constraint satisfaction and trajectory optimization. Mixed-Integer Convex Programming (MICP) has emerged as a particularly effective framework for this approach. MICP formulations for temporal logic constraints are fundamentally NP-hard due to their combinatorial nature. However, researchers have developed several approaches to reduce computational complexity.

2.2.1 Smoothing Approximation Methods Smoothing-based methods transform a discrete logical satisfaction problem into a continuous optimization problem, which can be solved by gradient-based techniques. Gilpin et al. (Gilpin et al. 2020) introduce a smooth robustness metric for STL that measures logical soundness on top of the gradient-based method. Mehdipour et al. (Mehdipour et al. 2019) develop an average-based robustness for continuous-time STL specifications that provides a smoother quantitative semantics. Pant et al. (Pant et al. 2018) propose a fly-by-logic approach for multi-drone fleets leveraging smooth approximations to enable real-time control with temporal logic objectives. While this method improves computational speed, it sacrifices the guarantees of completeness.

2.2.2 Binary Variable Reduction Methods Many other studies also focus on improving MICP solver efficiency while maintaining completeness. One approach is to minimize the total number of binary variables. For example, Kurtz and Lin (Kurtz and Lin 2022) propose disjunction encodings that use logarithmic numbers of binary variables, thereby improving scalability for long-horizon specifications.

2.2.3 Convex Relaxation Tightening Methods Another approach focuses on designing MICP formulations with tighter convex relaxations to improve B&B efficiency. Marcucci and Tedrake (Marcucci and Tedrake 2019) compare several formulation approaches for optimal control of PWA systems. Their later work (Marcucci 2024; Marcucci et al. 2023) introduces GCS, designing optimization formulations with tighter convex relaxations for motion planning around obstacles leveraging a structure similar to network flows. The benefits of tighter convex relaxations for motion planning under LTL are further explored by Kurtz and Lin (Kurtz and Lin 2021, 2023).

In this paper, we present Logic Network Flow, a novel formulation that provides provably tighter convex relaxations for temporal logic specifications while maintaining both completeness and soundness guarantees. Our approach significantly improves computational efficiency for temporal logic planning problems compared to existing methods.

2.3 Applications of Temporal Logic Planning to Multi-Robot Coordination and Bipedal Locomotion

Recent years have witnessed increasing applications of temporal logic in robotic motion planning and control (Kress-Gazit et al. 2009; Plaku and Karaman 2016). Among these diverse applications of temporal logic, two particularly interesting research directions have emerged: multi-agent coordination leveraging robot teaming, and integration with complex dynamic models for platforms such as legged robots.

2.3.1 Multi-Robot Coordination Multi-robot coordination under temporal logic specifications has been studied across different types of teaming. For homogeneous teams, researchers have developed specialized approaches for specific platforms: Pant et al. (Pant et al. 2018) and Cardona et al. (Cardona et al. 2023b) utilize temporal logic specifications for coordination of drone swarms, while Kress-Gazit et al. (Kress-Gazit et al. 2008) and Scher et al. (Scher and Kress-Gazit 2020) incorporate car-like behaviors and dynamics for navigation in urban environments or warehouses. Recent work has increasingly focused on heterogeneous teams that combine different robot types to leverage their complementary capabilities (Shamsah et al. 2025; Cao et al. 2022). Schillinger et al. (Schillinger et al. 2018) introduce a framework that simultaneously handles task allocation and motion planning for heterogeneous multi-robot systems under temporal logic specifications. Zhou et al. (Zhou et al. 2022) introduce specific planning strategies for teams combining quadrupedal and wheeled robots.

2.3.2 Motion Planning for Bipedal Locomotion Bipedal locomotion planning has traditionally leveraged

optimization-based approaches with predefined goals, such as (Kuindersma et al. 2016) and (Huang and Grizzle 2023). More recently, researchers have proposed integrating temporal logic with more complicated dynamic models for bipedal locomotion (Shamsah et al. 2023; Jiang et al. 2023). Zhao et al. (Zhao et al. 2022) present a framework for reactive task and motion planning for whole-body dynamic locomotion handling logical specifications. Gu et al. (Gu et al. 2025) propose a signal temporal logic-guided model predictive control approach for bipedal locomotion resilient to external perturbations. Ren et al. (Ren et al. 2025) accelerate STL-based bipedal locomotion planning through Benders Decomposition, separating logical constraints from nonlinear kinematics and dynamics. These works demonstrate that temporal logic can effectively describe complex locomotion tasks while respecting the dynamic constraints of robots. In our work, we further advance this direction by integrating LNF with Linear Inverted Pendulum models, allowing bipedal walking robots to synthesize trajectories under temporal logic constraints on terrains with predefined safe contact regions.

3 Background

3.1 Piecewise-Affine Dynamic Systems

Consider a discrete-time dynamical system in the form of

$$\mathbf{x}_{k+1} = f(\mathbf{x}_k, \mathbf{u}_k) \quad (1)$$

where $\mathbf{x}_k \in \mathcal{X} \subseteq \mathbb{R}^{n_x} \times \mathbb{B}^{n_z}$ represents the state vector, consisting of continuous variables of size n_x and binary variables of size n_z , with $\mathbb{B} = \{0, 1\}$ and $k = 0, 1, \dots, T$ denoting the time steps; $\mathbf{u}_k \in \mathcal{U} \subseteq \mathbb{R}^{n_u}$ represents the control input of size n_u . Given the control input at each time step and the initial state of the trajectory $\mathbf{x}_0 \in \mathcal{X}_0$, where \mathcal{X}_0 is typically a singleton set containing only the initial condition, a run of the system is expressed as $\xi = (\mathbf{x}_0 \mathbf{u}_0)(\mathbf{x}_1 \mathbf{u}_1) \dots$ via rolling out Eqn. (1).

While Eqn. (1) captures general nonlinear dynamics, a wide range of nonlinear dynamic systems can be effectively approximated by Piecewise Affine (PWA) models (Sontag 1981). PWA systems naturally translate into mixed-integer convex programs (MICPs) (Marcucci and Tedrake 2019), making them ideal dynamics representations for our paper. Let $\mathbf{x} = \{\mathbf{x}_0, \dots, \mathbf{x}_T\}$ and $\mathbf{u} = \{\mathbf{u}_0, \dots, \mathbf{u}_{T-1}\}$ represent the state and control trajectories. We first define a collection of polytopes (i.e., bounded polyhedra): $\mathcal{D}_i \triangleq \{(\mathbf{x}_k, \mathbf{u}_k) \mid \mathbf{H}_1^i \mathbf{x}_k + \mathbf{H}_2^i \mathbf{u}_k \leq \mathbf{h}^i\}$, where $i \in \mathcal{I}$ denotes the index set. The dynamics of the discrete-time PWA systems are expressed as:

$$\mathbf{x}_{k+1} = \mathbf{A}^i \mathbf{x}_k + \mathbf{B}^i \mathbf{u}_k \quad (2a)$$

$$\mathbf{H}_1^i \mathbf{x}_k + \mathbf{H}_2^i \mathbf{u}_k \leq \mathbf{h}^i \text{ for some } i \in \mathcal{I} \quad (2b)$$

where $\mathbf{A}^i \in \mathbb{R}^{n_x \times n_x}$ and $\mathbf{B}^i \in \mathbb{R}^{n_x \times n_u}$ are the system matrices, and $\mathbf{H}_1^i \in \mathbb{R}^{n_c \times n_x}$, $\mathbf{H}_2^i \in \mathbb{R}^{n_c \times n_u}$, and $\mathbf{h}^i \in \mathbb{R}^{n_c}$ are the constraint matrices and vector, respectively.

3.2 Temporal Logic Preliminaries

In this paper, we focus on bounded-time temporal logic formulas built upon convex predicates, specifically Metric

Temporal Logic (MTL) and Signal Temporal Logic (STL), where the maximum trajectory length T to determine logic satisfiability is finite. We recursively define the syntax of temporal logic formulas as follows (Belta and Sadraddini 2019): $\varphi := \pi \mid \neg \varphi \mid \varphi_1 \wedge \varphi_2 \mid \varphi_1 \vee \varphi_2 \mid \diamondsuit_{[k_1, k_2]} \varphi \mid \square_{[k_1, k_2]} \varphi \mid \varphi_1 \mathcal{U}_{[k_1, k_2]} \varphi_2$, where the semantics consists of not only boolean operations “and” (\wedge) and “or” (\vee), but also temporal operators “always” (\square), “eventually” (\diamondsuit), and “until” (\mathcal{U}). φ , φ_1 and φ_2 in the definition are formulas, and π is an atomic predicate $\mathcal{X} \rightarrow \mathbb{B}$ whose truth value is defined by the sign of the convex function $g^\pi : \mathcal{X} \rightarrow \mathbb{R}$. We assume the convex function is a combination of linear functions, which can be expressed as $g^\pi(\mathbf{x}_k) = (\mathbf{a}^\pi)^\top \mathbf{x}_k + b^\pi$. Let $\Pi = \{\pi^1, \dots, \pi^{|\Pi|}\}$ be the set of $|\Pi|$ atomic predicates. Define the binary predicate variable $z^{\pi^i} \in \mathbb{B}$ for each predicate π^i at time step k such that:

$$\begin{aligned} (\mathbf{a}^{\pi^i})^\top \mathbf{x}_k + b^{\pi^i} \geq 0 &\Leftrightarrow z^{\pi^i} = 1, \\ (\mathbf{a}^{\pi^i})^\top \mathbf{x}_k + b^{\pi^i} < 0 &\Leftrightarrow z^{\pi^i} = 0 \end{aligned} \quad (3)$$

Let vector \mathbf{z}^π collect these binary predicates across all predicates and time steps into a single vector:

$$\mathbf{z}^\pi = [z^{\pi^1}_0, z^{\pi^2}_0, \dots, z^{\pi^0}_{|\Pi|}, z^{\pi^1}_1, \dots, z^{\pi^0}_{|\Pi|}]^\top \quad (4)$$

A run ξ that satisfies a temporal logic formula φ is denoted as $\xi \models \varphi$. The satisfaction of a formula φ having a state signal \mathbf{x} starting from time step k is defined inductively as in Table 1.

In particular, STL provides a unique capability of admitting a *robustness degree* (Fainekos and Pappas 2009) of how strongly a formula is satisfied by a signal (Belta and Sadraddini 2019). A positive robustness value indicates satisfaction, and the magnitude represents the margin of robustness against disturbances. Table II shows the semantics of the robustness degree of STL.

3.3 Optimization-based Temporal Logic Motion Planning

On the basis of the mathematical foundations of PWA dynamics and temporal logic specifications, we next formulate the optimization problem that integrates these components. We structure the objective function in the form of $f_{\text{obj}}(\xi, \mathbf{z}^\pi) = f_{\text{obj}}(\mathbf{x}, \mathbf{u}, \mathbf{z}^\pi) = \mathbf{x}^\top \mathbf{Q} \mathbf{x} + \mathbf{u}^\top \mathbf{R} \mathbf{u} + \Theta^\top \mathbf{z}^\pi$, where the quadratic terms $\mathbf{x}^\top \mathbf{Q} \mathbf{x} + \mathbf{u}^\top \mathbf{R} \mathbf{u}$ can represent energy consumption, control effort, or maximizing robustness measures. The linear term $\Theta^\top \mathbf{z}^\pi$ rewards the satisfaction of specific predicates. For example, this term can encode preferences for regions in the state space with lower risks of failure.

We present a formal statement of the optimization problem for motion planning and control under temporal logic constraints.

Problem 1. Temporal Logic Motion Planning with PWA Dynamics. *Given a system of the form (2) and a temporal logic specification φ , compute a control input sequence \mathbf{u} such that the resulting trajectory ξ satisfies $\xi \models \varphi$ and $f_{\text{obj}}(\xi, \mathbf{z}^\pi)$ is minimized.*

Nomenclature

System Dynamics

k	Discrete time step, $k = 0, 1, \dots, T$
T	Planning horizon
$\mathbf{x}_k, \mathbf{u}_k$	System state and control input at time step k
ξ	System trajectory (run)
\mathcal{D}_i	i -th polytope region for PWA dynamics
$\mathbf{A}^i, \mathbf{B}^i$	System matrices for mode i
$\mathbf{H}_1^i, \mathbf{H}_2^i, \mathbf{h}^i$	Polytope constraint matrices/vector for mode i

Temporal Logic

φ	Temporal logic formula
π	Atomic predicate
Π	Set of atomic predicates
$z^{\pi_k^i}$	Binary predicate variable for π^i at time step k
z^π	Vector of binary predicates across all predicates and time steps
\wedge, \vee, \neg	Logical AND, OR, NOT
$\square_{[k_1, k_2]}$	Operator “Always”
$\diamond_{[k_1, k_2]}$	Operator “Eventually”
$\mathcal{U}_{[k_1, k_2]}$	Operator “Until”

Logic Tree (LT)

\mathcal{T}^φ	LT for formula φ
z^{φ_i}	Binary variable for internal node φ_i
z^φ	Vector of internal node binary variables

Logic Network Flow (LNF)

\mathcal{F}^φ	LNF for formula φ
\mathcal{G}	Directed graph $(\mathcal{V}, \mathcal{E})$
v_s, v_t	Source and target vertices
$\mathcal{E}_v^{\text{in}}, \mathcal{E}_v^{\text{out}}$	Incoming/outgoing edges of vertex v
\mathcal{P}_e	Predicates associated with edge e
y_e	Binary edge traversal variable
ω_e	Flow variable for edge e
$\mathbf{v}_e^+, \mathbf{v}_e^-$	Artificially designed indicator vectors

Dynamic Network Flow (DNF)

\mathcal{G}_d	Temporal graph
\mathcal{V}_d	Set of vertices in temporal graph representing spatial locations
\mathcal{E}_d	Set of directed edges in temporal graph
T_d, C_d	Travel time and edge capacity functions for each edge
θ_k	Time-varying edge traversal cost
r_e	DNF flow variable
\mathcal{P}^π	Vertices with physical locations satisfying predicate π

Abbreviations

LNF	Logic Network Flow
LT	Logic Tree
DNF	Dynamic Network Flow
LP	Linear Programming
MILP	Mixed-Integer Linear Programming
MICP	Mixed-Integer Convex Programming
MIP	Mixed-Integer Programming
STL	Signal Temporal Logic
MTL	Metric Temporal Logic
PWA	Piecewise-Affine
B&B	Branch and Bound
GCS	Graph-of-Convex-Sets
LIP	Linear Inverted Pendulum
F-M	Fourier-Motzkin (Elimination)

Table 1. Validity semantics of Signal Temporal Logic

$$\begin{aligned}
 (\mathbf{x}, k) \models \varphi_1 \wedge \varphi_2 &\Leftrightarrow (\mathbf{x}, k) \models \varphi_1 \wedge (\mathbf{x}, k) \models \varphi_2 \\
 (\mathbf{x}, k) \models \varphi_1 \vee \varphi_2 &\Leftrightarrow (\mathbf{x}, k) \models \varphi_1 \vee (\mathbf{x}, k) \models \varphi_2 \\
 (\mathbf{x}, k) \models \diamond_{[k_1, k_2]} \varphi &\Leftrightarrow \exists k' \in [k + k_1, k + k_2], (\mathbf{x}, k') \models \varphi \\
 (\mathbf{x}, k) \models \square_{[k_1, k_2]} \varphi &\Leftrightarrow \forall k' \in [k + k_1, k + k_2], (\mathbf{x}, k') \models \varphi \\
 (\mathbf{x}, k) \models \varphi_1 \mathcal{U}_{[k_1, k_2]} \varphi_2 &\Leftrightarrow \exists k' \in [k + k_1, k + k_2], (\mathbf{x}, k') \models \varphi_2 \\
 &\quad \wedge \forall k'' \in [k + k_1, k'] (\mathbf{x}, k'') \models \varphi_1
 \end{aligned}$$

Given the problem statement above, we propose a unified formulation to solve it. The fundamental idea is to design two complementary sets of constraints: one instantiating the temporal logic specifications and the other capturing the PWA system dynamics. The two constraint sets are then composed into a single formulation with the predicate variables z^π coupling both counterparts, such that the dynamics evolve in a manner consistent with the logical requirements. This integrated approach leads to the following optimization formulation:

Table 2. Robustness degree semantics of Signal Temporal Logic

$$\begin{aligned}
 \rho^\pi(\mathbf{x}, k) &= (\mathbf{a}^\pi)^\top \mathbf{x}_k + b^\pi \\
 \rho^{\neg\varphi}(\mathbf{x}, k) &= -\rho^\varphi(\mathbf{x}, k) \\
 \rho^{\varphi_1 \wedge \varphi_2}(\mathbf{x}, k) &= \min(\rho^{\varphi_1}(\mathbf{x}, k), \rho^{\varphi_2}(\mathbf{x}, k)) \\
 \rho^{\varphi_1 \vee \varphi_2}(\mathbf{x}, k) &= \max(\rho^{\varphi_1}(\mathbf{x}, k), \rho^{\varphi_2}(\mathbf{x}, k)) \\
 \rho^{\diamond_{[k_1, k_2]} \varphi}(\mathbf{x}, k) &= \max_{k' \in [k + k_1, k + k_2]} (\rho^\varphi(\mathbf{x}, k')) \\
 \rho^{\square_{[k_1, k_2]} \varphi}(\mathbf{x}, k) &= \min_{k' \in [k + k_1, k + k_2]} (\rho^\varphi(\mathbf{x}, k')) \\
 \rho^{\varphi_1 \mathcal{U}_{[k_1, k_2]} \varphi_2}(\mathbf{x}, k) &= \max_{k' \in [k + k_1, k + k_2]} (\min(\rho^{\varphi_2}(\mathbf{x}, k'), \\
 &\quad \min_{k'' \in [k + k_1, k']} (\rho^{\varphi_1}(\mathbf{x}, k''))))
 \end{aligned}$$

Formulation 1. (Optimization Formulation for Temporal Logic Motion Planning with PWA Dynamics)

$$\begin{aligned}
 &\underset{\xi, \gamma, z^\pi}{\text{minimize}} \quad f_{\text{obj}}(\xi, z^\pi) \\
 \text{s.t.} \quad &\text{Eqn. (2), } \mathbf{x}_0 \in \mathcal{X}_0 \quad (\text{PWA dynamics}) \\
 &\text{Eqn. (3), } \forall k, \forall \pi \in \Pi \quad (\text{Atomic predicates}) \\
 &\mathcal{C}_{\text{logic}}(\gamma, z^\pi) \leq 0 \quad (\text{Temporal logics})
 \end{aligned}$$

The temporal logic module is represented as a set of constraints denoted by $\mathcal{C}_{\text{logic}}(\gamma, z^\pi) \leq 0$. The vector γ comprises the variables specific to the logic formulation (e.g., edge variables in LNF or node variables in LT, as we will introduce later). In the following sections, we will explore different versions for the temporal logic formulations and PWA dynamics that fall under the umbrella of this general optimization structure.

In the next section, we study the LT approach, a conventional method to encode temporal logic constraints into mixed-integer programs. This will provide the foundation for understanding our proposed LNF framework in Section IV.

3.4 Logic Tree

Logic Tree (LT) (Wolff et al. 2014; Raman et al. 2014), also referred to as STL Tree (Kurtz and Lin 2022), STL Parse Tree (Leung et al. 2023), and AND-OR Tree (Sun et al. 2022), is a hierarchical data structure encapsulating temporal logic formulas to facilitate efficient optimization solve. We first provide its definition and an example of translating a temporal logic formula to an LT:

Definition 1. A Logic Tree T^φ constructed from a temporal logic specification φ is defined as a tuple $(\circ, \Pi, \mathcal{N}, \tau)$, where:

- $\circ \in \{\wedge, \vee\}$ denotes the combination type;
- $\Pi = \{\pi^1, \dots, \pi^{|\Pi|}\}$ is the set of $|\Pi|$ predicates associated with each leaf node in the tree T^φ . Each leaf node is assigned a variable $z^{\pi_k^i}$ to indicate its validity.
- $\mathcal{N} = \{T^{\varphi_0}, T^{\varphi_1}, \dots, T^{\varphi_n}\}$ represents the set of $n + 1$ internal nodes having at least one child, where the root node is denoted by $T^\varphi = T^{\varphi_0}$. Each node is associated with a temporal logic formula φ_i and a combination type \circ . Similarly, each internal node is assigned a variable z^{φ_i} to indicate the formula's validity.
- $\tau = \{t^{\varphi_0}, t^{\varphi_1}, \dots, t^{\varphi_n}\}$ is a list of starting times corresponding to each of the temporal logic formulas at the internal nodes and predicates at the leaf nodes.

Example 1. Consider a specification $\diamondsuit_{[0,2]}(\square_{[0,1]}\pi)$ whose corresponding LT is shown in Fig. 2. This tree has 10 nodes, including 6 leaf nodes and 4 internal nodes. The root node has a combination type of disjunction corresponding to the operator \diamondsuit in the formula, and three second-level conjunction nodes correspond to the operator \square in the formula.

Given Definition 1, now we recast Problem 1 as an LT problem:

Problem 1.1. Temporal Logic Motion Planning with PWA Dynamics using Logic Tree. Given a system of the form (2) and a temporal logic formula φ , construct a Logic Tree T^φ according to Definition 1, and then compute a control input sequence u such that the resulting trajectory ξ satisfies $\xi \models \varphi$ and $f_{\text{obj}}(\xi, z^\pi)$ is minimized.

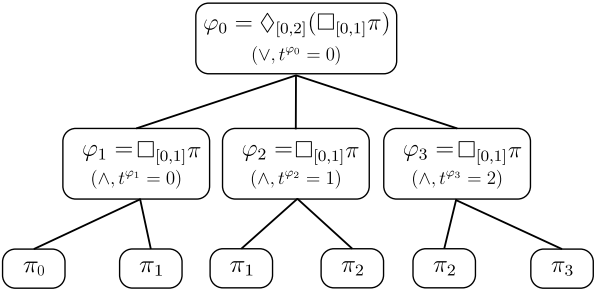


Figure 2. The LT for $\diamondsuit_{[0,2]}(\square_{[0,1]}\pi)$ given in Example 1.

To encode temporal logic constraints represented by an LT into an optimization formulation, the works in (Wolff et al. 2014) and (Raman et al. 2014) propose an MILP where binary variables are assigned to both internal nodes $z^{\varphi_i}, \forall i \in \{0, \dots, n\}$ and leaf nodes $z^{\pi_k^i}, \forall t, i \in \{1, \dots, |\Pi|\}$. For each internal node with a conjunction combination type: $\varphi = \wedge_{i=1}^p \varphi_i$ where φ_i is the suboperand of the child nodes, the following constraints are enforced:

$$z^\varphi \leq z^{\varphi_i}, \quad i = 1, \dots, p \quad (5a)$$

$$z^\varphi \geq 1 - p + \sum_{i=1}^p z^{\varphi_i} \quad (5b)$$

Similarly, for each internal node with a disjunction combination type: $\varphi = \vee_{i=1}^q \varphi_i$, the following constraints are applied:

$$z^\varphi \geq z^{\varphi_i}, \quad i = 1, \dots, q \quad (6a)$$

$$z^\varphi \leq \sum_{i=1}^q z^{\varphi_i} \quad (6b)$$

On the root node, $z^{\varphi_0} = 1$ must hold to ensure the full temporal logic specification is satisfied. By constructing the LT T^φ , we present the following formulation to solve Problem 1.1, which is identical to equation 15 in (Belta and Sadraddini 2019):

Formulation 1.1. (Optimization Formulation for Temporal Logic Motion Planning with PWA Dynamics using Logic Tree)

$$\begin{aligned} & \underset{\xi, z^\varphi, z^\pi}{\text{minimize}} \quad f_{\text{obj}}(\xi, z^\pi) \\ & \text{s.t.} \quad \begin{aligned} & \text{Eqn. (2), } \mathbf{x}_0 \in \mathcal{X}_0 && (\text{PWA dynamics}) \\ & \text{Eqn. (3), } \forall k, \forall \pi \in \Pi && (\text{Atomic predicates}) \\ & \text{Eqn. (5) (6), } \forall T^{\varphi_i} \in \mathcal{N} \quad \left. \begin{aligned} & z^{\varphi_0} = 1 \end{aligned} \right\} && (\text{LT constraints}) \end{aligned} \end{aligned}$$

where $\mathcal{C}_{\text{logic}}$ from Formulation 1 is replaced by the specific LT constraints (5) and (6), and the variables γ are replaced by z^φ , which is given as:

$$z^\varphi = [z^{\varphi_0}, z^{\varphi_1}, \dots, z^{\varphi_n}]^\top \in \mathbb{B}^{n+1} \quad (7)$$

Constraints (5) and (6) guarantee that if all child variables z^{φ_i} claim binary values, then the parent variable z^φ will also take a binary value. By induction, this implies that as long as the leaf variables z^π are binary, all internal

variables z^{φ_i} will be binary as well. Nevertheless, we explicitly impose binary constraints on all variables to ensure mathematical completeness of the formulation. To illustrate this formulation, we apply it to Example 1:

Example 1.1. Example 1 Continued. We present Formulation 1.1 for Example 1. For the disjunction node at φ_0 , (6) translates to:

$$z^{\varphi_0} = 1, \quad z^{\varphi_0} \geq z^{\varphi_i}, i = 1, 2, 3, \quad z^{\varphi_0} \leq \sum_{i=1}^3 z^{\varphi_i}$$

For the conjunction nodes at φ_j , $j \in \{1, 2, 3\}$, (5) translates to:

$$z^{\varphi_j} \leq z^{\pi_k}, \forall k \in I_j, \quad z^{\varphi_j} \geq -1 + \sum_{k \in I_j} z^{\pi_k}$$

where $I_1 = \{0, 1\}$, $I_2 = \{1, 2\}$, and $I_3 = \{2, 3\}$. The constraints above substitute $\mathcal{C}_{\text{logic}}(\gamma, z^{\pi}) \leq 0$.

3.5 Branch and Bound

The problem formulation proposed in this study is an MILP, which is known to be NP-complete (Karp 2010), and Branch and Bound (B&B) is a well-received method to solve MILPs. For a feasible optimization problem, B&B converges to the global optimum; otherwise, it provides a certificate of infeasibility. In this section, we briefly introduce B&B, and refer readers to (Conforti et al. 2014) for a more detailed description.

Consider an MILP with continuous variables $\mathbf{x} \in \mathbb{R}^{n_x}$, binary variables $\mathbf{z} \in \mathbb{B}^{n_z}$, and an optimal objective value LP^* . B&B manages a search tree, where each node corresponds to a linear programming (LP) problem. These LP problems on nodes are created by relaxing some binary variables $\mathbf{z}[j]$, $j = \{1, \dots, n_z\}$ to continuous variables, and imposing bounds on them. The root node of the tree is a linear program LP_0 that relaxes all binary variables to continuous variables.

Each LP_i in the search tree is associated with a lower bound, \underline{LP}_i , on its optimal objective value LP_i^* . Heuristics are applied to effectively obtain upper bounds. The B&B algorithm also keeps an incumbent solution, \overline{LP} , which is the best objective value found so far. This value also serves as an upper bound on LP^* . If no feasible solution has been found up to the current iteration, \overline{LP} is set to $+\infty$. B&B relies on efficiently pruning the search tree using both upper and lower bounds, which ends when \underline{LP}_i is a tight lower bound of LP_i^* , and \overline{LP} is a tight upper bound of LP^* (Conforti et al. 2014).

The relaxation gap of B&B is defined as $G_a = |\overline{LP} - \underline{LP}|/|\overline{LP}|$, where \underline{LP} is the best lower bound among all LP_i . G_a is used to measure the tightness of bounds and the solver will terminate when $G_a = 0$. On a special note, the root relaxation gap is defined as $G_r = |\overline{LP} - LP_0|/|\overline{LP}|$.

4 Logic Network Flow

This section presents the proposed Logic Network Flow (LNF) formulation. Section 4.1 defines LNF and introduces an algorithm to construct the network structure from temporal logic specifications. Section 4.2 develops the

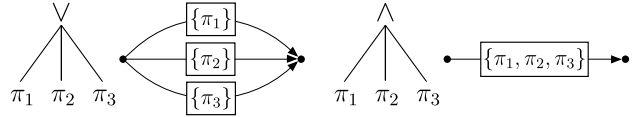


Figure 3. An illustration of the strategy to translate conjunction and disjunction combination types from an LT to an LNF in Algorithm 1.

optimization formulation based on this representation, and Section 4.3 describes a network-flow-based Fourier–Motzkin variable elimination procedure that enhances computational efficiency of the optimization framework.

4.1 Logic Network Flow

Our approach begins with the definition of LNF, a new formulation for encoding temporal logic specifications.

Definition 2. A Logic Network Flow \mathcal{F}^φ from the specification φ is defined as a tuple $(\mathcal{G}, \mathcal{P}, \Pi)$, where:

- $\mathcal{G} = (\mathcal{V}, \mathcal{E})$ is a directed graph with a vertex $v_s \in \mathcal{V}$ be the source vertex and a vertex $v_t \in \mathcal{V}$ be the target vertex.
- $\Pi = \{\pi^1, \dots, \pi^{|\Pi|}\}$ is the set of $|\Pi|$ predicates associated with each leaf node in the tree T^φ (as in Def. 1). The binary vector z^π is defined as (4) representing the truth values of all predicates in Π at given times.
- \mathcal{P} is a collection of sets of n_e ($n_e \leq |\Pi|$) possibly negated predicates that must hold true (or false if negated) to pass through each edge $e \in \mathcal{E}$, defined as $P_e := \{\pi^i | \pi^i \in \Pi \text{ s.t. } z^{\pi^i} = 1 \text{ (or } z^{\pi^i} = 0 \text{ if } \pi^i \text{ is negated)}\} \in \mathcal{P}$.

Given the definition above, we reformulate Problem 1 using LNF.

Problem 1.2. Temporal Logic Motion Planning with PWA Dynamics using Logic Network Flow. Given a system of form (2) and a temporal logic formula φ , construct a Logic Network Flow \mathcal{F}^φ according to Definition 2, and then compute a control input sequence u such that the resulting trajectory ξ satisfies $\xi \models \varphi$ and $f_{\text{obj}}(\xi, z^\pi)$ is minimized.

Let $e \in \mathcal{E}$ denote any edge in the LNF. For each vertex $v \in \mathcal{V}$, $\mathcal{E}_v^{\text{in}}$ is defined as the set of incoming edges to v and $\mathcal{E}_v^{\text{out}}$ as the set of outgoing edges from v . We present Algorithm 1 that translates an LT into an LNF. Meanwhile, a similar approach can also be used to construct LNFs directly from STL specifications. We initialize with $\text{BUILDNODE}(T^{\varphi_0}, v_s, e, P_e)$, where v_s is a source vertex, e is a “dangling” outgoing edge $e \in \mathcal{E}_{v_s}^{\text{out}}$ without any target, and $P_e = \emptyset$ is an empty predicate set for edge e . The algorithm performs a post-order traversal of the logic tree, constructing a new vertex in the LNF when completing a disjunction node (line 13). Directed edges are generated only from a previous disjunction node to nodes built after it, ensuring the post-order traversal forms a topological sorting and the resulting graph is acyclic. The algorithm returns the target vertex v_t . Fig. 3 illustrate the conversion of LTs to LNFs for conjunction and disjunction nodes.

Algorithm 1 BUILDNODE

Input: An LT node T^{φ_i} , a vertex v , an outgoing edge e of v , and a predicate set P_e for edge e .

Output: A vertex v , an outgoing edge e of v , and a predicate set P_e for edge e .

```

1: if  $T^{\varphi_i} = \pi^\varphi$  is a leaf node then
2:   Add  $\pi^\varphi$  to  $P_e$ .
3:   return  $v, e, P_e$ 
4: if  $\circ(T^{\varphi_i}) = \wedge$  then
5:   for each child  $T^{\varphi_j}$  of  $T^{\varphi_i}$  do
6:      $v, e, P_e = \text{BUILDNODE}(T^{\varphi_j}, v, e, P_e)$ 
7:   return  $v, e, P_e$ 
8: if  $\circ(T^{\varphi_i}) = \vee$  then
9:   (Assume  $n$  to be the number of subnodes of  $T^{\varphi_i}$ )
10:  Duplicate  $e, P_e$  for  $n - 1$  times, denote as  $e_j, P_{e,j}$ , where  $j = 1, \dots, n$ .
11:  for each child  $T^{\varphi_j}$  of  $T^{\varphi_i}$  do
12:     $v, e_{o,j}, P_{o,j} = \text{BUILDNODE}(T^{\varphi_j}, v, e_j, P_{e,j})$ 
13:    Initialize a new vertex  $v_{\varphi_i}$ , an outgoing edge  $e_{\varphi_i}$ , and a set  $P_{e_{\varphi_i}} = \emptyset$  for the edge  $e_{\varphi_i}$ 
14:    Assign  $\mathcal{E}_{v_{\varphi_i}}^{\text{in}} = \{e_{o,j}, j = 1, \dots, n\}$ .
15:  return  $v_{\varphi_i}, e_{\varphi_i}, P_{e_{\varphi_i}}$ .
```

4.2 Optimization Formulation

Given a \mathcal{F}^φ , we propose an optimization formulation with a tighter convex relaxation than LT. For each edge $e \in \mathcal{E}$ in the LNF, let $y_e \in \mathbb{B}$ specify if the edge is traversed by the flow, with a total of one unit of flow entering the network (i.e., $\sum_{e \in \mathcal{E}_{v_s}^{\text{out}}} y_e = 1$). In addition, we associate a multi-dimensional continuous flow variable $\omega_e \in [0, 1]^{|\Pi|}$ to each edge, with its in-flow at v_s being z^π . The idea of associating continuous variables with edges in network flow structures stems from the Graph-of-Convex-Sets (GCS) formulation (Marcucci 2024), where continuous flow variables represent dynamic trajectories that must satisfy convex set constraints. Our LNF formulation adapts this concept to the logical domain, where ω_e indicates predicate truth values.

We devise the convex set constraint to instantiate the logical requirements, such that if the in-flow passes through an edge e , we require $\omega_e[i] = 1$ for all non-negated predicate $\pi_i \in P_e$, where π_i is the i^{th} predicate in Π ; for negated predicates $\neg\pi_i \in P_e$, we require $\omega_e[i] = 0$; and for predicates not contained in P_e , no constraint is imposed on $\omega_e[i]$. These requirements can be expressed as two convex set constraints that need to be enforced concurrently:

$$\omega_e \geq y_e \mathbf{v}_e^+, \quad \omega_e \leq \mathbf{1}_{|\Pi|} - y_e \mathbf{v}_e^- \quad (8)$$

where $\mathbf{v}_e^+ \in \mathbb{B}^{|\Pi|}$ and $\mathbf{v}_e^- \in \mathbb{B}^{|\Pi|}$ are artificially designed column vectors to help encode the logical constraints. Specifically, $\mathbf{v}_e^+[i] = 1$ if $\pi_i \in P_e$, and 0 otherwise; and $\mathbf{v}_e^-[i] = 1$ if $\neg\pi_i \in P_e$, and 0 otherwise.

For logical consistency, we also require that if all predicates in the set P_e are satisfied, then the edge e must be traversed ($y_e = 1$). This is identical to constraint (5b):

$$y_e \geq 1 - |P_e| + \sum_{\pi_i \in P_e} z^{\pi_i} + \sum_{\neg\pi_i \in P_e} (1 - z^{\pi_i}) \quad (9)$$

For each vertex $v \in \mathcal{V}$ with the input edges $\mathcal{E}_v^{\text{in}} \subset \mathcal{E}$ and the output edges $\mathcal{E}_v^{\text{out}} \subset \mathcal{E}$, flow conservation constraints are

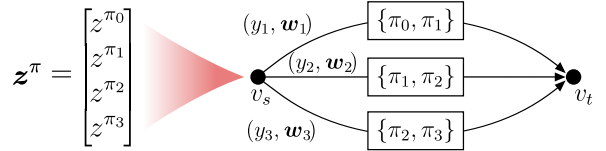


Figure 4. The LNF for $\diamond_{[0,2]}(\square_{[0,1]}\pi)$, given in Example 2.

enforced on both y_e and ω_e :

$$\sum_{e \in \mathcal{E}_v^{\text{in}}} y_e = \sum_{e \in \mathcal{E}_v^{\text{out}}} y_e \quad (10a)$$

$$\sum_{e \in \mathcal{E}_v^{\text{in}}} \omega_e = \sum_{e \in \mathcal{E}_v^{\text{out}}} \omega_e \quad (10b)$$

Flow conservation constraints are also applied to source vertex v_s , where one unit of flow is injected:

$$1 = \sum_{e \in \mathcal{E}_{v_s}^{\text{out}}} y_e \quad (11a)$$

$$z^\pi = \sum_{e \in \mathcal{E}_{v_s}^{\text{out}}} \omega_e \quad (11b)$$

Overall, the LNF formulation aims to direct a continuous in-flow z^π from the source vertex to the target vertex. If z^π reaches the target vertex, then we say the specification φ is satisfied.

Example 2. Consider the same logic specification as in Example 1, whose corresponding LNF is illustrated by Fig. 4. This LNF consists of 3 edges and 2 vertices: v_s and v_t . The variables in the LNF are $[y_1, y_2, y_3]$, $y_i \in \mathbb{B}$, and $[\omega_1, \omega_2, \omega_3]$, $\omega_i \in \mathbb{B}^4$. The top edge is associated with the predicate set $P_1 = \{\pi_0, \pi_1\}$ containing only non-negated predicates, so the first inequality constraint in (8) simplifies to $\omega_1 \geq y_1[1, 1, 0, 0]^\top$. Similar constraints are applied to the other two edges. For the source vertex v_s , the flow conservation constraints are given by $y_1 + y_2 + y_3 = 1$ and $z^\pi = \omega_1 + \omega_2 + \omega_3$.

Given a constructed LNF \mathcal{F}^φ , we reformulate Problem 1 with the LNF framework:

Formulation 1.2. (Optimization Formulation for Temporal Logic Motion Planning with PWA Dynamics using Logic Network Flow)

$$\begin{aligned}
 & \underset{\xi, \mathbf{y}, \omega, z^\pi}{\text{minimize}} \quad f_{\text{obj}}(\xi, z^\pi) \\
 \text{s.t.} \quad & \text{Eqn. (2), } \mathbf{x}_0 \in \mathcal{X}_0 \quad (\text{PWA dynamics}) \\
 & \text{Eqn. (3), } \forall k, \forall \pi \in \Pi \quad (\text{Atomic predicates}) \\
 & \left. \begin{aligned} & \text{Eqn. (8), } \forall e \in \mathcal{E} \\ & \text{Eqn. (10), (11) } \forall v \in \mathcal{V} \end{aligned} \right\} \quad (\text{LNF constraints})
 \end{aligned}$$

Specifically, $\mathcal{C}_{\text{logic}}$ from Formulation 1 is replaced by LNF constraints (8), (10), and (11), and variables γ are replaced by \mathbf{y} and ω , which are defined as:

$$\mathbf{y} = [y_1, y_2, \dots, y_{|\mathcal{E}|}]^\top \in \mathbb{B}^{|\mathcal{E}|} \quad (12a)$$

$$\omega = [\omega_1^\top, \omega_2^\top, \dots, \omega_{|\mathcal{E}|}^\top]^\top \in [0, 1]^{|\mathcal{E}| \cdot |\Pi|} \quad (12b)$$

4.3 Network-flow-based Fourier-Motzkin Elimination

While GCS admits tighter convex relaxations, this comes at the cost of introducing additional continuous flow variables, which in turn may increase the problem size and computational overhead. In (Marcucci et al. 2023), the authors suggest taking advantage of parallel computing to improve the solving speed for the convex relaxations of GCS.

With GCS as the backbone of our established LNF formulation, we further improve its computational efficiency by introducing a novel network-flow-based Fourier–Motzkin procedure that decreases the number of variables in the formulation while preserving the tightness of the relaxation. This procedure eliminates the flow variables ω_e and replaces the flow conservation constraints with inequality constraints. Although this technique could simplify general GCS formulations, in this paper we focus on how it refines our LNF formulation and improves computational performance without resorting to parallel computing.

We present here a simplified Fourier–Motzkin elimination process featuring the major changes from Formulation 1.2. For a rigorous mathematical treatment, we refer readers to Appendix B.

Since constraint (8) already provides explicit bounds on all flow variables ω_e , it can directly be used to eliminate the flow conservation constraints (10b) and (11b). Starting with constraint (11b) for the source vertex, each ω_e on the right-hand side is switched with its corresponding upper and lower bounds from (8). This substitution discards ω_e entirely and creates two sets of inequalities involving only variables z^π and y_e :

$$z^\pi \geq \sum_{e \in \mathcal{E}_{v_s}^{\text{out}}} y_e \mathbf{v}_e^+, \quad z^\pi \leq \sum_{e \in \mathcal{E}_{v_s}^{\text{out}}} \mathbf{1}_{|\Pi|} - y_e \mathbf{v}_e^- \quad (13)$$

Constraints (13) are added to the formulation in place of (11b). Note that (13) is equivalent to (8) and (11b) with respect to the feasible set for z^π , and therefore this variable reduction preserves the tightness of the convex relaxation. See Appendix C for a detailed proof.

We then propagate the flow out of v_s . Consider a vertex v where its full set of input flow variables ω_e , $e \in \mathcal{E}_v^{\text{in}}$, appear on the right-hand side of (11b). These variables can be replaced by the corresponding output flows from v through the flow conservation constraint (10b):

$$z^\pi = \sum_{e \in \mathcal{E}_{v_s}^{\text{out}} \setminus \mathcal{E}_v^{\text{in}}} \omega_e + \sum_{e \in \mathcal{E}_v^{\text{out}}} \omega_e$$

This substitution yields new constraints with the same structure as (11b), but with different ω_e variables on the right-hand side. We then repeat the substitution process described in the previous paragraph, replacing each ω_e with its bounds from (8), resulting in constraints that involve only z^π and y_e . These derived constraints also become part of the formulation.

In addition, inequality constraints are generated between input and output edge variable y_e by combining (8) with flow conservation (10b). When there are non-negated predicates on the input edges and negated predicates on the output

edges, or vice versa, these inequality constraints become:

$$\sum_{e \in \mathcal{E}_v^{\text{in}}} y_e \mathbf{v}_e^+ \leq \sum_{e \in \mathcal{E}_v^{\text{out}}} \mathbf{1}_{|\Pi|} - y_e \mathbf{v}_e^- \quad (14a)$$

$$\sum_{e \in \mathcal{E}_v^{\text{in}}} \mathbf{1}_{|\Pi|} - y_e \mathbf{v}_e^- \geq \sum_{e \in \mathcal{E}_v^{\text{out}}} y_e \mathbf{v}_e^+ \quad (14b)$$

They are indispensable when the same predicate appears with different negation statuses on the input and output edges, as elucidated in Appendix D. These cases can be identified by examining if a predicate has different negation conditions on both sides of a vertex after constructing the LNF.

The flow conservation constraint (10b) is omitted after adding these derived constraints above. We continue this process iteratively, propagating flows through each vertex in the network until reaching v_t , where no further propagation is possible. Fig. 5 illustrates this process on an LNF with a simple structure.

At this point, the flow variables ω_e and their associated constraints in (8), (10b), and (11b) have been completely taken over by inequality constraints between z^π and y_e . This transformation comes to a formulation with significantly fewer continuous variables while retaining the same tightness of convex relaxation as the original formulation presented in Section 4.2.

Example 2.1. Example 2 Continued. We build on Example 2 to demonstrate the variable elimination procedure. The graph consists of two vertices: v_s and v_t . Applying the inequality constraints (8) to the flow conservation constraint at v_s gives $z^\pi = \omega_1 + \omega_2 + \omega_3 \geq y_1[1, 1, 0, 0]^\top + y_2[0, 1, 1, 0]^\top + y_3[0, 0, 1, 1]^\top$. This produces the following set of constraints:

$$\begin{aligned} y_1 + y_2 + y_3 &= 1 \\ y_1 &\leq z^\pi[1], \\ y_1 + y_2 &\leq z^\pi[2], \\ y_2 + y_3 &\leq z^\pi[3], \\ y_3 &\leq z^\pi[4] \end{aligned}$$

For comparison, recall from Example 1.1 that the constraints derived from the three conjunction nodes in the LT formulation are:

$$\begin{aligned} z^{\varphi_1} &\leq z^\pi[1], & z^{\varphi_1} &\leq z^\pi[2], \\ z^{\varphi_2} &\leq z^\pi[2], & z^{\varphi_2} &\leq z^\pi[3], \\ z^{\varphi_3} &\leq z^\pi[3], & z^{\varphi_3} &\leq z^\pi[4] \end{aligned}$$

where the above two formulations share the same y_i and z^{φ_i} . By examining these constraints from LT with the last four constraints in LNF, it is easy to conclude that the LNF formulation yields a tighter convex relaxation.

Remark 1. While this paper focuses on formulating temporal logic specifications, the proposed Fourier–Motzkin elimination process can be applied to simplify many other types of GCS formulations by removing flow variables and improving computational performance without sacrificing relaxation tightness. In Appendix E, we provide an example by applying it to the minimum-time control of discrete-time linear systems from Chapter 10.1 of (Marcucci 2024).

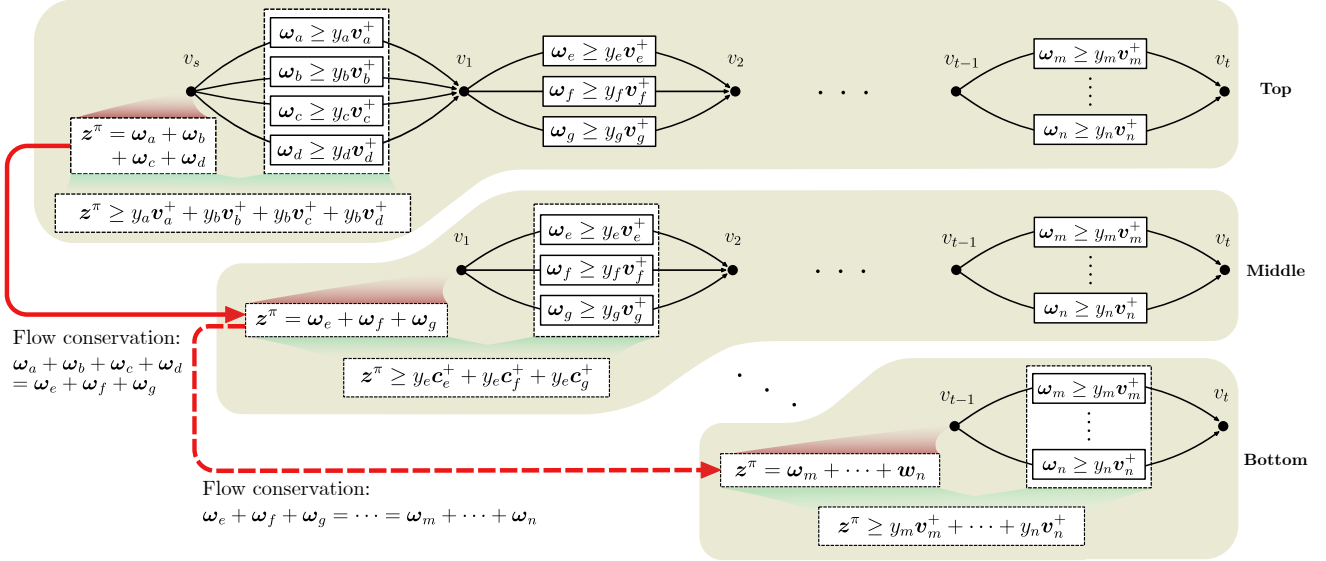


Figure 5. Illustration of the Network-Flow-Based Fourier-Motzkin variable elimination process. *Top*: Starting from source vertex v_s , constraints (8) ($\omega_i \geq y_i v_i^+$, $i = a, b, c, d$) and (11b) ($z^\pi = \sum_{i=a}^d \omega_i$) are replaced by a single inequality (13) ($z^\pi \geq \sum_{i=a}^d y_i v_i^+$), thereby eliminating flow variables ω_a to ω_d . *Middle*: Flow conservation at vertex v ($\sum_{i=a}^d \omega_i = \sum_{j=e}^g \omega_j$) is applied, generating a new constraint with the same structure as (11b) ($z^\pi = \sum_{j=e}^g \omega_j$). When combined with convex set constraints, this yields $z^\pi \geq \sum_{j=e}^g y_j v_j^+$. *Bottom*: This process continues iteratively, propagating flows through the network until reaching target vertex v_t , at which point no further propagation is possible.

4.4 Proof of Tighter Convex Relaxation

Following the empirical example from the previous section, now we present a theorem rigorously proving that the convex relaxations from the LNF formulations are tighter than those from LT formulations. Specifically, we show that for any problem setup including cost coefficients \mathbf{Q} , \mathbf{R} , Θ , and initial conditions \mathbf{x}_0 , the optimal cost of the convex relaxation of LNF is greater than or equal to that of LT. We denote the convex relaxation problems of LNF and LT as LNF-relax and LT-relax, respectively, with their corresponding optimal objective values being $f_{\text{LNF-r}}^*$ and $f_{\text{LT-r}}^*$. The following theorem formalizes this statement:

Theorem 1. *For any given \mathbf{Q} , \mathbf{R} , Θ , and \mathbf{x}_0 , if the convex relaxation problem LNF-relax is feasible with an optimal cost $f_{\text{LNF-r}}^*$, then the convex relaxation problem LT-relax is also feasible with an optimal cost $f_{\text{LT-r}}^* \leq f_{\text{LNF-r}}^*$.*

Proof. Without loss of generality, we assume the logic specification takes the form of $\varphi = \bigwedge_{l=1}^L \bigvee_{m=1}^{M_l} \bigwedge_{n=1}^{N_{m,l}} \pi_{m,n}^l$, where $\pi_{m,n}^l$ is a predicate belonging to Π (possibly negated). This conjunctive-disjunctive form naturally arises from common temporal logic specifications where multiple requirements must be satisfied simultaneously (outer conjunction), each potentially having alternative ways of satisfaction (disjunction), with specific conditions for each alternative (inner conjunction). Any propositional logic formula can be converted to this form through iterative application of distributivity and De Morgan's laws (Jackson and Sheridan 2004). This is reflected in the LT shown in Fig. 6 (A): the root node φ_0 is a conjunction of suboperands φ_l ($l = 1, \dots, L$); each φ_l is a disjunction of formula $\varphi_{m,l}$ ($m = 1, \dots, M_l$), with each formula itself a conjunction of predicates $\pi_{m,n}^l$ ($n = 1, \dots, N_{m,l}$). Building on this conjunctive-disjunctive structure, we formulate the corresponding convex relaxation

problem LT-relax as:

$$\underset{\xi, z^\varphi, z^\pi}{\text{minimize}} \quad \mathbf{x}^\top \mathbf{Q} \mathbf{x} + \mathbf{u}^\top \mathbf{R} \mathbf{u} + \Theta^\top z^\pi$$

s.t. for $l = 1, \dots, L$:

$$z^{\varphi_l} = 1 \quad (15a)$$

$$z^{\varphi_l} \geq z^{\varphi_{m,l}}, \quad m = 1, \dots, M_l \quad (15b)$$

$$z^{\varphi_l} \leq \sum_{m=1}^{M_l} z^{\varphi_{m,l}} \quad (15c)$$

for $m = 1, \dots, M_l$:

$$\begin{aligned} z^{\varphi_{m,l}} &\geq 1 - |P_{m,l}| + \sum_{\pi_j \in P_{m,l}} z^{\pi_j} \\ &+ \sum_{\neg\pi_j \in P_{m,l}} (1 - z^{\pi_j}) \end{aligned} \quad (15d)$$

for $j = 1, \dots, |\Pi|$:

$$z^{\pi_j} \geq z^{\varphi_{m,l}}, \quad \text{if } \pi_j \in P_{m,l} \quad (15e)$$

$$z^{\pi_j} \leq (1 - z^{\varphi_{m,l}}), \quad \text{if } \neg\pi_j \in P_{m,l} \quad (15f)$$

$$(2), \mathbf{x}_0 \in \mathcal{X}_0, \quad (3), \forall k, \forall \pi \in \Pi \quad (15g)$$

where $P_{m,l}$ denotes the set of possibly negated atomic predicates $\{\pi_{m,1}^l, \dots, \pi_{m,N_{m,l}}^l\}$ at the leaf nodes of the suboperand rooted at $\varphi_{m,l}$.

With Algorithm 1, we construct the LNF for φ as shown in Fig. 6 (B). In particular, Algorithm 1 collects all predicates at leaf nodes under each $\varphi_{m,l}$ to constitute a predicate set $P_{m,l}$ for each edge, coinciding with our definition of $P_{m,l}$ in the LT formulation. By applying Fourier-Motzkin elimination to the formulation for this structure via constraint (8), (9), (10) and (11) (detailed process omitted for brevity), we arrive at the convex relaxation problem LNF-relax:

$$\underset{\xi, y, z^\pi}{\text{minimize}} \quad \mathbf{x}^\top \mathbf{Q} \mathbf{x} + \mathbf{u}^\top \mathbf{R} \mathbf{u} + \Theta^\top z^\pi$$

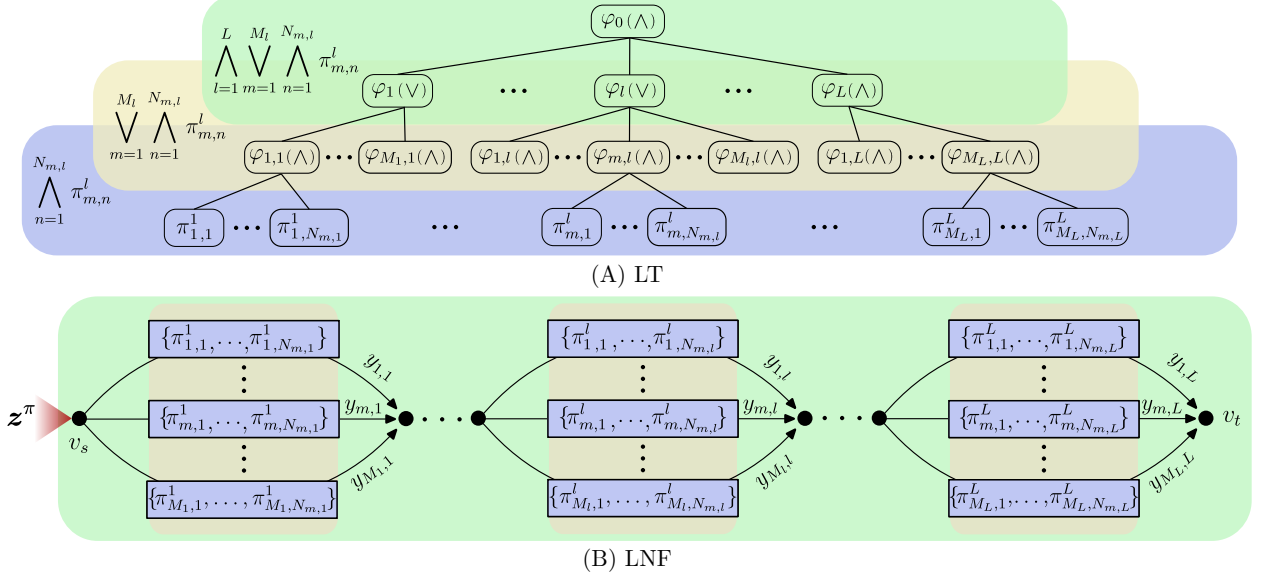


Figure 6. The representations of the conjunctive-disjunctive form $\varphi = \bigwedge_{l=1}^L \bigvee_{m=1}^{M_l} \bigwedge_{n=1}^{N_{m,l}} \pi_{m,n}^l$. (A) LT representation; (B) LNF representation constructed by Algorithm 1.

s.t. for $l = 1, \dots, L$:

$$\sum_{m=1}^{M_l} y_{m,l} = 1$$

for $j = 1, \dots, |\Pi|$:

$$z^{\pi_j} \geq \sum_{\substack{m=1, \dots, M_l \\ \pi_j \in P_{m,l}}} y_{m,l}$$

$$z^{\pi_j} \leq \sum_{\substack{m=1, \dots, M_l \\ \neg \pi_j \in P_{m,l}}} (1 - y_{m,l})$$

for $m = 1, \dots, M_l$:

$$\begin{aligned} y_{m,l} &\geq 1 - |P_{m,l}| + \sum_{\pi_j \in P_{m,l}} z^{\pi_j} \\ &+ \sum_{\neg \pi_j \in P_{m,l}} (1 - z^{\pi_j}) \end{aligned} \quad (16d)$$

$$(2), \mathbf{x}_0 \in \mathcal{X}_0, \quad (3), \forall k, \forall \pi \in \Pi \quad (16e)$$

Let $(\xi^*, \mathbf{y}^*, z^{\pi*})$ be any optimal solution for LNF-relax. We construct a solution for LT-relax by setting $z^\pi = z^{\pi*}$, $\xi = \xi^*$, and $z^{\varphi_{m,l}} = y_{m,l}^*$, $z^{\varphi_l} = 1$ for $l = 1, \dots, L$ and $m = 1, \dots, M_l$. We aim to show that this solution is also feasible for LT-relax and achieves the same objective value, and therefore prove that $f_{\text{LT-r}}^* \leq f_{\text{LNF-r}}^*$.

First, constraint (16a) requests $\sum_{m=1}^{M_l} y_{m,l}^* = 1$, $\forall l = 1, \dots, L$, which simultaneously guarantees the satisfaction of (15a), (15b) and (15c) in LT-relax. Next, we check constraints (15e) and (15f). For non-negated predicates, constraint (16b) implies $z^{\pi_j*} \geq \sum_{m: \pi_j \in P_{m,l}} y_{m,l}^* \geq y_{m,l}^* = z^{\varphi_{m,l}}$ for any $(l, j, m) \in \{(l, j, m) \mid l \in \{1, \dots, L\}, \pi_j \in P_{m,l}\}$, which corresponds to constraint (15e). For negated predicates, constraint (16c) analogously infers the satisfaction of (15f). Last, the dynamics constraints (2) and predicate constraints (3) in (15g) automatically hold true since $(\xi^*, z^{\pi*})$ are the optimal values shared by the both formulations. \square

It is obvious to show that the converse of Theorem 1 does not hold by finding a solution such that $f_{\text{LT-r}}^* < f_{\text{LNF-r}}^*$. Consider a counter-example with arguments $L = 1$ and $M = 2$, predicate sets $P_1 = \{\pi_1, \pi_2\}$ and $P_2 = \{\pi_2, \pi_3\}$, and uniform cost coefficients $\Theta = [1, 1, 1]$. The atomic predicates evaluate conditions on a single integrator system $x_{k+1} = x_k + u_k$ with state and input bounds $|x_k| \leq 1$, $|u_k| \leq 1$. The validity mapping for the predicates are $\pi_1 : x_1 = 1$, $\pi_2 : x_2 = 0$, and $\pi_3 : x_1 = -1$. These predicates are encoded using the following big-M constraints: $2z^{\pi_1} - 1 \leq x_1 \leq 1$ for π_1 , $z^{\pi_2} - 1 \leq x_2 \leq 1 - z^{\pi_2}$ for π_2 , and $-1 \leq x_1 \leq 1 - 2z^{\pi_3}$ for π_3 . LT-relax obtains an optimal solution $(y_1^* = 0.5, y_2^* = 0.5, z^{\pi_1*} = 0.5, z^{\pi_2*} = 0.5, z^{\pi_3*} = 0.5)$ with a cost of $f_{\text{LT-r}}^* = 1.5$. This solution, however, is infeasible for LNF-relax, which instead finds an optimal solution $(y_1^* = 1, y_2^* = 0, z^{\pi_1*} = 1, z^{\pi_2*} = 1, z^{\pi_3*} = 0)$ with a cost of 2. The binary solutions for both formulations achieve a cost of 2, but there is a 25% gap for LT whereas LNF has a zero gap.

Remark 2. The flow conservation constraint plays a key role in tightening the convex relaxation. Intuitively, it “couples” the predicates across different branches of a disjunction node, yielding multiple terms on the right-hand side of inequalities (16b) and (16c). This coupling would not be possible if LT were used as the underlying data structure, since in an LT, each node has only a single parent node, leading to one-to-one inequality constraints as seen in (15e) and (15f).

Remark 3. Formulation (16) is directly implementable in standard MIP solvers for temporal logic specifications in conjunctive-disjunctive form $\varphi = \bigwedge_{l=1}^L \bigvee_{m=1}^{M_l} \bigwedge_{n=1}^{N_{m,l}} \pi_{m,n}^l$. This is the formulation used throughout our experimental evaluation in Section 6.

We also show that the LNF formulation is sound — any solution from the LNF formulation satisfies the original problem specification — and complete — it finds a solution

whenever the specification is satisfiable. The proofs are provided in Appendix F.

4.5 Computational Complexity

The computational complexity of MICPs is dominated by the number of binary variables, with the worst-case computation time exponential in their number. Both LNF and LT formulations introduce binary variables: LNF has edge variables y and atomic predicates z^π ; LT has node variables z^φ and atomic predicates z^π . The atomic predicates z^π appear identically in both formulations, and their dimension is related to the planning horizon length and the number of predicates at each time step.

In addition to z^π , LNF assigns a binary variable y_e to each edge $e \in \mathcal{E}$, resulting in $O(|\mathcal{E}|)$ binary edge variables, where $|\mathcal{E}|$ is the total number of child nodes across all disjunction nodes in its corresponding LT. In contrast to LNF, LT formulation introduces a binary variable z^{φ_i} for each internal node φ_i in the tree. Bounded-time temporal operators like $\diamondsuit_{[t_1, t_2]}$ lead to $t_2 - t_1 + 1$ internal nodes per operator. Therefore, the number of internal variables is proportional to both the number of operators and the size of their associated time bounds. In most practical logic specifications, the additional binary variables introduced by LNF (y) and LT (z^φ) are approximately equal in number. The only exception occurs in cases where edges contain single predicates, where LNF may introduce additional edge variables compared to LT.

Both LNF and LT formulations involve continuous variables ξ associated with the underlying dynamics. Assuming they use the same dynamics formulation, the numbers of these variables are identical. It is worth noting that the Fourier-Motzkin process removes the continuous flow variables ω from the LNF formulation, avoiding the additional computational overhead that would arise if they were retained.

Regarding constraints, LNF incorporates flow conservation constraints (10a) and (11a) for each vertex in \mathcal{V} . The Fourier-Motzkin process also generates $O(|\Pi|)$ inequality constraints per vertex as it propagates the flow from the source v_s vertex-by-vertex towards the target v_t . However, many of these constraints are redundant and can be eliminated. Therefore, while the theoretical number of constraints is $O(|\mathcal{V}| \cdot |\Pi|)$, it typically requires significantly fewer constraints in practice. The number of constraints for LT formulation is also proportional to the number of internal nodes in the tree, as each internal node imposes individual constraints relating its associated variable to its parent. For the specification φ assumed in Theorem 1, within each disjunction section l ($l = 1, \dots, L$), LNF assigns one inequality per unique predicate, resulting in a total of $O(|\Pi|)$ constraints per section and $O(L \cdot |\Pi|)$ constraints overall. In comparison, LT defines one inequality for each instance of a predicate across the M_l conjunctive terms, leading to $O(M_l \cdot |\Pi|)$ constraints per section and $O(\sum_{l=1}^L M_l \cdot |\Pi|)$ constraints overall.

In conclusion, LNF formulations provide tighter convex relaxations compared to LT formulations, while generally not increasing the number of variables and constraints. This typically results in faster solving speeds, as demonstrated in our experimental results in Section 6.

5 Modeling of Dynamic Systems

While the LNF framework provides an efficient representation for temporal logic specifications, its practical application to robotics requires integration with appropriate dynamic system models. In this section, we review a series of existing approaches for modeling robot dynamics that can be integrated with our LNF framework. This integration forms a comprehensive framework, allowing users to select the dynamic system representation that best suits their specific robotic applications.

5.1 Abstraction of Dynamics in Discrete Configuration Space using Dynamic Network Flow

The first approach abstracts the dynamics constraint in Eqn. (1) through a Dynamic Network Flow (DNF) representation (Aronson 1989). A similar strategy has been utilized in (Kurtz and Lin 2021) for motion planning under MTL specifications. This approach begins with constructing a *temporal graph* where the discrete configuration space $\mathcal{X} = \{p_1, p_2, \dots, p_m\}$ is represented by a set of vertices $\{p_1, p_2, \dots, p_m\}$. Each vertex p_i corresponds to a physical location p_i , and the vertices are connected by directed edges (e.g., from p_i to p_j) with associated travel times and costs. This graph structure is then transformed into a DNF by expanding it along the time dimension. Although this concept has appeared in several works (e.g., (Yu and LaValle 2013)), we provide an explicit definition of temporal graph here for completeness.

Definition 3. (*Temporal Graph*) A *Temporal Graph* is a tuple $\mathcal{G}_d = (\mathcal{V}_d, \mathcal{E}_d, T_d, C_d, \theta, \mathcal{V}_s)$, where:

- $\mathcal{V}_d = \{p_1, p_2, \dots, p_m\}$ is a finite set of vertices where each vertex p_i represents a spatial location $p_i \in \mathcal{X}$ in the configuration space.
- $\mathcal{E}_d \subseteq \mathcal{V}_d \times \mathcal{V}_d$ is a set of directed edges, each $e_d = (p_i, p_j) \in \mathcal{E}_d$ corresponding to a movement from location p_i to location p_j .
- $T_d : \mathcal{E}_d \rightarrow \mathbb{R}^+$ is a function that assigns a positive travel time to each edge.
- $C_d : \mathcal{E}_d \rightarrow \mathbb{N}^+$ assigns a positive integer capacity to each edge indicating the maximum number of robots that can traverse the edge at the same time.
- $\theta_k : \mathcal{E}_d \rightarrow \mathbb{R}^+$ is a function that assigns a (potentially time-varying) positive cost to each edge representing the cost of traversing that edge at time step k , including self-loops representing the cost of remaining at a vertex for one time unit at time step k .
- $\mathcal{V}_s \subseteq \mathcal{V}_d$ is a set of source vertices aggregating initial positions of all robots.

Remark 4. Motion planning on temporal graphs under temporal logic constraints is NP-hard. Consider a simple temporal graph with only two vertices, where one vertex represents “true” and the other represents “false.” The robot transitions to, or remains at, the “true” vertex if a

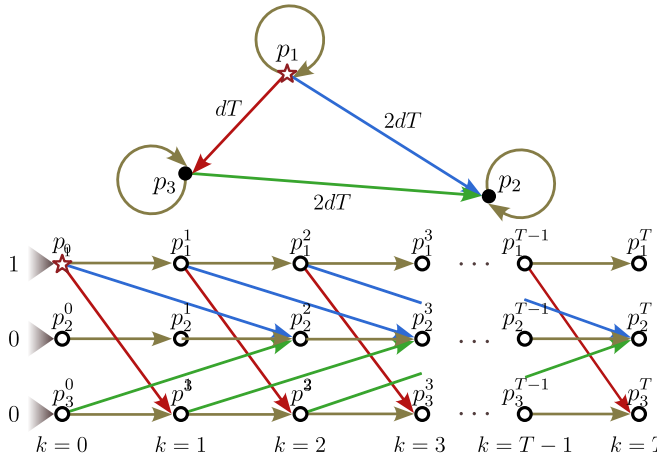


Figure 7. Conversion from a temporal graph to a DNF. *Upper*: A temporal graph consisting of three vertices p_1, p_2, p_3 with travel times $T_d(p_1, p_2) = 2dT$, $T_d(p_1, p_3) = dT$, and $T_d(p_2, p_3) = 2dT$. *Lower*: The converted DNF with time horizon T , where each vertex p_i is expanded into an array of time-indexed vertices $p_i^0, p_i^1, \dots, p_i^T$. Red and green arrows represent robots moving from one location to another, while golden arrows indicate robots staying at the same location. The robot initially starts from vertex p_1 depicted by a star icon.

logical condition is satisfied, and moves to the “false” vertex otherwise. Solving any Boolean satisfiability (SAT) problem then reduces to finding a valid robot trajectory satisfying the encoded logical formula on this specific temporal graph.

A temporal graph can be constructed for a robot system of interest by collecting a library of trajectories offline, followed by building a graph structure based on the library. This is also referred to as experience-based planning (Coleman et al. 2015), where a database stores memorized trajectories that can be retrieved and adapted to generate new trajectories. This setup is particularly beneficial for large configuration spaces that include many invariant constraints, such as planning within a (mostly) static environment.

We first present the construction of a temporal graph for a system involving only a single robot. This simplification obviates the need to consider collision avoidance between robots. It starts with identifying the locations in the configuration space that the STL specifications may require the robot to visit (i.e., those corresponding to atomic predicates for which $z^{\pi_k^i} = 1$). For each pair of locations p_i and p_j , we generate a feasible trajectory that satisfy the robot’s dynamic constraints using motion planning algorithms. Each feasible trajectory matches a directed edge $e = (p_i, p_j)$ in the temporal graph, associated with a travel time $T_d(e)$ representing a (preferably tight) upper bound on the actual traversal time from p_i to p_j , a cost $\theta(e)$ reflecting factors like energy consumption or terrain traversability, and a capacity $C_d(e) = 1$ limiting passage to a single robot. Additionally, we assign a cost $\theta(p_i)$ to each vertex p_i representing the cost of remaining at that location for a unit of time, to capture factors such as weather severity.

With an established temporal graph, we proceed to build a DNF with a time horizon T . For each vertex $p_i \in \mathcal{V}_d$, we index it by discrete time steps to produce a new array of vertices $p_i^0, p_i^1, \dots, p_i^T$, where each p_i^k corresponds to a visiting location p_i at time $k \cdot dT$. The time discretization dT is selected as the greatest common divisor of all travel times

such that $T_d(e)/dT$ take integer values (rounding up $T_d(e)$ if necessary to meet integer multiples of dT). If traversing along an edge $e = (p_i, p_j)$ takes $T_d(e)/dT$ time steps, edges are connected from p_i^k to $p_j^{k+T_d(e)/dT}$, for any k such that $k + T_d(e)/dT \leq T$. Moreover, for each vertex $p_i \in \mathcal{V}_d$ and time step k such that $k + 1 \leq T$, edges are also introduced from p_i^k to p_i^{k+1} , representing the robot’s staying at the same location between consecutive time steps. Fig. 7 illustrates this conversion from a temporal graph to a DNF.

DNF can be formulated as an LP problem, similar to a standard network flow optimization. Let \mathcal{E}_{DNF} denote the set of all edges in the DNF. For each edge $e \in \mathcal{E}_{\text{DNF}}$ corresponding to $(p_i, p_j) \in \mathcal{E}_d$ starting at time step k , we associate a continuous flow variable $r_e \in [0, 1]$, upon which we impose flow conservation constraints on the source vertices \mathcal{V}_s and all other vertices through:

$$\sum_{e \in \mathcal{E}_{p^k}^{\text{in}}} r_e = \sum_{e \in \mathcal{E}_{p^k}^{\text{out}}} r_e, \quad \forall p \in \mathcal{V}_d, \quad k = 1, \dots, T \quad (17a)$$

$$\sum_{e \in \mathcal{E}_{p^0}^{\text{out}}} r_e = 1, \quad \forall p \in \mathcal{V}_s \quad (17b)$$

$$\sum_{e \in \mathcal{E}_{p^0}^{\text{in}}} r_e = 0, \quad \forall p \in \mathcal{V}_d \setminus \mathcal{V}_s \quad (17c)$$

where $\mathcal{E}_{p^k}^{\text{in}}$ and $\mathcal{E}_{p^k}^{\text{out}}$ denote the sets of incoming and outgoing edges, respectively, for vertex p^k .

Also for each edge $e \in \mathcal{E}_{\text{DNF}}$ corresponding to $e' \in \mathcal{E}_d$, the flow incurs a cost $\tilde{\theta}(e) \cdot r_e$, proportional to the amount of flow r_e , where $\tilde{\theta}(e) = \theta_k(e')$. This cost expression applies to both robots moving between different locations in the temporal graph and those remaining at the same locations. Therefore, the overall objective function is:

$$f_{\text{obj}}(\mathbf{r}) = \sum_{e \in \mathcal{E}_{\text{DNF}}} \tilde{\theta}(e) \cdot r_e \quad (18)$$

where $\mathbf{r} = [r_{e_1}, r_{e_2}, \dots, r_{e_{|\mathcal{E}_{\text{DNF}}|}}]^{\top} \in [0, 1]^{|\mathcal{E}_{\text{DNF}}|}$.

To define the atomic predicates in discrete vertex space of DNF, for each predicate π we associate the set $\mathcal{P}^\pi \subseteq \mathcal{V}_d$ containing vertices p whose physical locations in the temporal graph \mathbf{p} satisfy $(\mathbf{a}^\pi)^\top \mathbf{p} + b^\pi \geq 0$. At any time step, the predicate π is considered satisfied if the robot traverses an edge that leads into a vertex in \mathcal{P}^π . This is expressed as:

$$\bigvee_{p \in \mathcal{P}^\pi, e \in \mathcal{E}_{p^k}^{\text{in}}} r_e \Leftrightarrow z^{\pi_k} = 1 \quad (19)$$

In words, the binary edge variables r_e in the DNF, or their disjunctions, can be directly considered as the atomic predicates z^π .

Through constraints (17), DNF defines a special type of dynamics on the discrete space \mathcal{X} . The robot positions evolve following $\mathbf{p}_j^{k+T_d(e_d)/dT} = \mathbf{p}_i^k + \mathbf{u}_k$, where $e_d = (p_i, p_j)$ and \mathbf{u}_k represent the discrete transition chosen at time step k . This discrete transition system can be viewed as a special case of the PWA dynamics. With the DNF formulation, the state variables ξ are now superseded by flow variables \mathbf{r} , and the general atomic predicate (3) is replaced by the constraint (19). We have:

Formulation 1.3. (*Optimization Formulation for Temporal Logic Motion Planning with DNF Dynamics*)

$$\begin{aligned}
 & \text{minimize}_{\mathbf{r}, \gamma, z^\pi} \quad (18) \\
 \text{s.t.} \quad & \text{Eqn. (17)} \quad (\text{DNF dynamics}) \\
 & \text{Eqn. (19), } \forall k, \forall \pi \in \Pi \quad (\text{Atomic predicates}) \\
 & \mathcal{C}_{\text{logic}}(\gamma, z^\pi) \leq 0 \quad (\text{Temporal logics})
 \end{aligned}$$

In the end, we show a lemma arguing that, when z^π is fixed to binary values and at most one unit of flow passing through each vertex in \mathcal{P}^π at any time (which holds by default for single-robot cases), the DNF subset of formulation (1), including the objective function (18), and constraints (17) and (19), possesses a tight LP relaxation. That is, we do not need to explicitly require \mathbf{r} to be binary, as their optimal values will inherently take binary values. This justifies the selection of DNF to represent dynamic models, as when integrated with LNF, it preserves the tightness of the convex relaxation. The proof follows directly from standard network flow theory, so it is omitted for brevity, and readers can refer to Chapter 11.12 of (Ahuja et al. 1994).

Lemma 2. (*Tight LP Relaxation of DNF*) *If at most one unit of flow passes through each vertex in \mathcal{P}^π for any time step, the optimal solution \mathbf{r} of the following formulation takes binary values:*

$$\begin{aligned}
 & \text{minimize}_{\mathbf{r}} \quad (18) \\
 \text{s.t.} \quad & \text{Eqn. (17)} \quad (\text{DNF dynamics}) \\
 & \text{Eqn. (19), } \forall k, \forall \pi \in \Pi \quad (\text{Atomic predicates}) \\
 & z^\pi \text{ fixed to binary values}
 \end{aligned}$$

Remark 5. *Rather than enforcing z^π as binary variables, an alternative is to keep z^π continuous and require the LNF edge variables y_e to be binary, since disjunctions are the source of discrete decisions in the logic structure that requires binary variables. Furthermore, we can employ encoding techniques that use fewer binary variables, such as those in (Kurtz and Lin 2022), where only $\lceil \log_2(n) \rceil$ binary variables are demanded for n disjunctive choices. This reduction in binary variables leads to additional computational speedups.*

5.2 Incorporating Multi-robot Planning with Collision Avoidance on Dynamic Network Flow

Collision avoidance is indispensable in multi-robot motion planning, whether homogeneous (e.g., a team of ground vehicles) or heterogeneous (e.g., ground and aerial platforms, or manipulators mounted at different locations). To address potential conflicts, pairwise collision checking is conducted on the temporal graphs generated from trajectory libraries of different robots. Three types of collision scenarios are identified in our study:

1. *Vertex-to-vertex collisions.* This occurs when two robots attempt to occupy the same spatial location simultaneously, or when two robots attempt to occupy different spatial locations but are too close to each other given the robots' physical dimensions.

2. *Vertex-to-edge collisions.* This occurs when a stationary robot is at a spatial location that interferes with another robot's trajectory.
3. *Edge-to-edge collisions.* This occurs when robots are moving head-to-head along the same path in opposite directions, or robots are moving along different paths but colliding at a finite or infinite number of intersection points given the robots' physical dimensions.

All three types of collisions can be resolved through designing additional constraints in the DNF formulation. Consider R robots in the system, where each robot $l \in \{1, \dots, R\}$ has its own temporal graph $\mathcal{G}_d^l = (\mathcal{V}_d^l, \mathcal{E}_d^l, T_d^l, C_d^l, \theta^l, \mathcal{V}_s^l)$ with corresponding flow variables r_e^l for the edges in the associated DNF. We build a conflict set \mathcal{C} comprising robot-vertex pairs (l, p) and robot-edge pairs (\bar{l}, e) that cannot be active simultaneously. For vertex-to-vertex collisions, \mathcal{C} contains only robot-vertex pairs (l, p) ; for edge-to-edge collisions, only robot-edge pairs (\bar{l}, e) ; and for vertex-to-edge collisions, either type may appear. Inspired by (Yu and LaValle 2016), we apply the following constraint for every such conflict set:

$$\sum_{(l,p) \in \mathcal{C}} \sum_{e \in \mathcal{E}_{p^k}^{\text{in}}} r_e^l + \sum_{(\bar{l},e) \in \mathcal{C}} r_{\bar{e}}^{\bar{l}} \leq 1, \quad \forall k \quad (20)$$

This constraint ensures that at most one element from each conflict set can be active at any given time step, which prevents all three types of collisions.

When the robot team is homogeneous, a single DNF is sufficient to represent all robots. In this scenario, vertex-to-vertex collisions can be avoided by limiting the input degree of each vertex to at most one ($\sum_{e \in \mathcal{E}_{p^k}^{\text{in}}} r_e \leq 1$), while edge-to-edge collisions can be eliminated by setting the edge capacity $C_d(e) = 1$. However, (20) breaks the tight LP relaxation property established in Lemma 2 for single-robot DNF. Therefore, all edge variables r_e^l in (20) must be explicitly set as binary variables.

5.3 Incorporating Dynamics in Continuous Configuration Space

While the prior approaches abstract the dynamics in discrete configuration space as a special case of PWA dynamics, here we present the big-M formulation for the general class of PWA dynamics in continuous configuration space, although alternative formulations, such as the convex hull formulation, also exist. Readers are referred to (Marcucci and Tedrake 2019) for a comprehensive comparison of different PWA formulations.

We model PWA systems using the standard big-M approach (Bemporad and Morari 1999) because it is widely received due to its ease of implementation and general effectiveness with modern MIP solvers, though it can yield loose convex relaxations when the big-M constants are large. For each polytope \mathcal{D}_i , $i \in \mathcal{I}$, we introduce a binary variable $\delta_{i,k}$ to indicate if the system state \mathbf{x}_k and input \mathbf{u}_k at time step k lie within the polytope. The following constraints ensure that exactly one polytope constraint is satisfied for

the system state and control input at any time step:

$$\mathbf{x}_{k+1} - \mathbf{A}^i \mathbf{x}_k - \mathbf{B}^i \mathbf{u}_k \geq - \sum_{j \in \mathcal{I} \setminus \{i\}} \delta_{j,k} \mathbf{M}_1^{ij} \quad (21a)$$

$$\mathbf{x}_{k+1} - \mathbf{A}^i \mathbf{x}_k - \mathbf{B}^i \mathbf{u}_k \leq \sum_{j \in \mathcal{I} \setminus \{i\}} \delta_{j,k} \mathbf{M}_2^{ij} \quad (21b)$$

$$\mathbf{H}_1^i \mathbf{x}_k + \mathbf{H}_2^i \mathbf{u}_k \leq \mathbf{h}^i + \sum_{j \in \mathcal{I} \setminus \{i\}} \delta_{j,k} \mathbf{M}_3^{ij} \quad (21c)$$

$$\sum_{i \in \mathcal{I}} \delta_{i,k} = 1 \quad (21d)$$

The constraints above collectively instantiate the big-M implementation for constraint (2). Constraints (21a), (21b), and (21c) enforce that if polytope \mathcal{D}_i is active ($\delta_{i,k} = 1$), the associated dynamics and domain constraints of mode i are satisfied. Otherwise, when $\delta_{i,k} = 0$, these constraints become inactive due to the big-M terms. Meanwhile, constraint (21d) ensures that only one polytope is active at each time step.

Smaller \mathbf{M}_1^{ij} , \mathbf{M}_2^{ij} , \mathbf{M}_3^{ij} values provide tighter convex relaxations, which generally leads to better computational performance. These values for each pair of modes $(i, j) \in \mathcal{I} \times \mathcal{I}$ can be minimized through:

$$\begin{bmatrix} \mathbf{M}_1^{ij} \\ \mathbf{M}_2^{ij} \\ \mathbf{M}_3^{ij} \end{bmatrix} := \max_{(\mathbf{x}_k, \mathbf{u}_k) \in \mathcal{D}_j} \begin{bmatrix} -(\mathbf{A}^i + \mathbf{A}^j) \mathbf{x}_k - (\mathbf{B}^i + \mathbf{B}^j) \mathbf{u}_k \\ (\mathbf{A}^i - \mathbf{A}^j) \mathbf{x}_k + (\mathbf{B}^i - \mathbf{B}^j) \mathbf{u}_k \\ -\mathbf{h}^i + \mathbf{H}_1^i \mathbf{x}_k + \mathbf{H}_2^i \mathbf{u}_k \end{bmatrix}$$

such that when mode $j \neq i$ is selected ($\delta_{j,k} = 1$), the right-hand sides of constraints (21a), (21b), and (21c) become sufficiently large to render these constraints inactive.

Equation (3) can be used straightforwardly to define atomic predicates for the big-M formulation of PWA. When $\mathbf{H}_2^i = \mathbf{0}$ for all $i \in \mathcal{I}$, the big-M formulation builds a direct connection between binary variables and polytope membership. This is because constraint (21d) enforces that exactly one $\delta_{i,k}$ equals 1, which makes constraint (21c) equivalent to $\mathbf{H}_1^i \mathbf{x}_k \leq \mathbf{h}^i$ when $\delta_{i,k} = 1$. Therefore, by defining $g^{\pi_i}(\mathbf{x}_k) = -\mathbf{H}_1^i \mathbf{x}_k + \mathbf{h}^i$, the binary variable $\delta_{i,k}$ functions exactly same as the predicate variable z^{π_i} .

Combining the big-M formulation for the general class of PWA dynamics with our LNF, we present the complete optimization formulation for Problem 1.2:

Formulation 1.4. (Optimization Formulation for Temporal Logic Motion Planning with Big-M Formulation of PWA Dynamics)

$$\begin{aligned} & \text{minimize}_{\xi, \gamma, z^\pi} f_{\text{obj}}(\xi, z^\pi) \\ \text{s.t.} & \quad \text{Eqn. (21), } \mathbf{x}_0 \in \mathcal{X}_0 \quad (\text{big-M PWA dynamics}) \\ & \quad \text{Eqn. (3), } \forall k, \forall \pi \in \Pi \quad (\text{Atomic predicates}) \\ & \quad \mathcal{C}_{\text{logic}}(\gamma, z^\pi) \leq 0 \quad (\text{Temporal logics}) \end{aligned}$$

Remark 6. Instead of using the full PWA dynamics formulation in (21), we can leverage Bézier curves to model the coordinates of interest for planning (such as CoM position), which can reduce the number of variables and constraints. This approach is used in the GCS formulation (Marcucci et al. 2023) for MIP of motion planning around

obstacles, where the convex hull property of Bézier curves ensures obstacle avoidance. The assignment of predicates follows a similar approach to the DNF formulation in (19), where binary variables indicate which polytope each curve segment occupies. We adopt this approach in our hardware experiments in Section 6.5.

6 Experiments

We conduct comprehensive experiments to evaluate the computational advantages of the LNF formulation compared to the LT formulations. Our experimental evaluation includes four case studies that demonstrate the versatility and scalability of our approach: (i) vehicle routing problems with time windows using DNF models, (ii) multi-robot coordination using pre-computed trajectory libraries, (iii) optimal motion planning with PWA dynamics using big-M formulation, and (iv) hardware experiments demonstrating real-time replanning capabilities with quadrupedal robots in dynamic environments.

For each scenario, we formulate the task specification using both our proposed LNF Formulation 1.1 and the baseline LT Formulation 1.2, comparing their performance across the convex relaxation tightness measured by the root relaxation gap, and the computational efficiency measured by solution times. We conduct multiple trials with randomized parameters to ensure statistical significance. For a comprehensive comparison, we evaluate both formulations using two state-of-the-art MIP solvers: Gurobi 12.0 and CPLEX 22.1.1.0, both with default settings. All experiments were conducted on a computer with 12th Gen Intel Core i7-12800H CPU and 16GB RAM.

6.1 Path Planning on Temporal Graph Formulated as Dynamic Network Flow

First, we evaluate our LNF formulation on temporal graphs formulated as DNF, as described in Section 5.1. The first experiment involves multi-target scenarios where one robot needs to visit at least one target from each of several target groups. This experiment follows (Kurtz and Lin 2021), which provides a direct comparison baseline. We benchmark our proposed Formulation 1.3 against the LT formulation used in that paper, which is identical to our LT formulation in Formulation 1.1.

To build the environment, we construct a 16×16 grid world with randomly scattered targets and obstacles. The center of each grid cell corresponds to a vertex in the temporal graph. The robot is able to travel from one cell to an adjacent cell horizontally or vertically, which forms an edge in the temporal graph taking $2dT$, or travel diagonally to an adjacent cell, which builds an edge taking $3dT$. Following (Kurtz and Lin 2021), we vary the number of target groups N_g from 2 to 5, set the planning horizon to $10N_g$ time steps, and place $2N_g$ obstacles in the environment. The robot must visit at least one target among each group while avoiding all obstacles. This temporal logic specification is given by:

$$\square_{[0,T]} \neg \text{obstacle} \wedge \bigwedge_{k=1}^{N_g} \left[\diamondsuit_{[0,T]} \left(\bigvee_{l=1}^{N_t} \text{target}_k^l \right) \right] \quad (22)$$

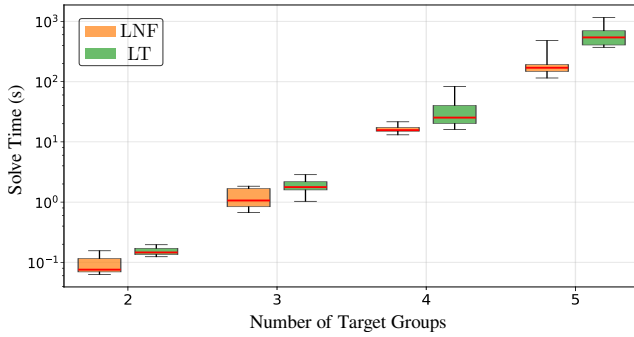


Figure 8. Scalability comparison between the LNF and LT formulations for multi-target scenarios with varying number of target groups N_g . x -axis: number of target groups (N_g); y -axis: solving time to prove global optimality (seconds).

where target_k^l denotes the l -th target in group k . We have $N_t = 3$ targets per group, and T is the planning horizon.

Results We conduct multiple trials for each N_g , with positions of targets and obstacles randomly sampled within the grid world, and edge costs sampled uniformly from $[0, 1]$ to model varying traversal difficulties. The results for solving time to prove global optimality are collected in Fig. 8, where each box plot shows the median (horizontal red line), upper and lower quartiles (colored box) and full range (whiskers).

For smaller problem sizes ($N_g = 2, 3$), all solving times of the baseline formulation are within a few seconds, which is consistent with (Kurtz and Lin 2021). However, our proposed LNF formulation demonstrates consistent speedups across all problem sizes. For problems of smaller sizes such as $N_g = 2, 3$, LNF achieves a median solving time 2× faster than LT. As problem size increases, the improvement becomes more significant: for $N_g = 5$, LNF achieves a 3× speedup with a median time of 170 s compared to 540 s for LT. We attribute the superior performance of LNF to the significantly tighter convex relaxations. The average root relaxation gaps for LNFs are 10.16%, 24.27%, 37.46%, 51.78% for $N_g = 2, 3, 4, 5$ respectively, while those for LTs are 31.05%, 46.81%, 56.49%, 65.89%. This shows LNF consistently achieves relaxation gaps tighter than LT for each problem size. This allows the B&B process to prune the tree more efficiently and avoid unnecessary branching by detecting earlier if certain nodes are not worth further exploration.

The second set of experiments considers the Vehicle Routing Problems with Time Windows (VRPTW), where a fleet of R homogeneous robots must visit specific locations within their designated time windows $[0, T]$ and obey temporal constraints. Each location has a required service duration. To build a realistic environment, we segment the map into polygons and shrink them to create paths and intersections. Each intersection corresponds to one vertex in the temporal graph, and each path represents an edge. The travel time for each path is computed by dividing the travel distance by a constant speed. An example of such an environment and the resulting planned paths is shown in Fig. 9.

We examine two variants of specifications. The first specification requires at least one robot to visit each location within its time window and execute the task for a specified

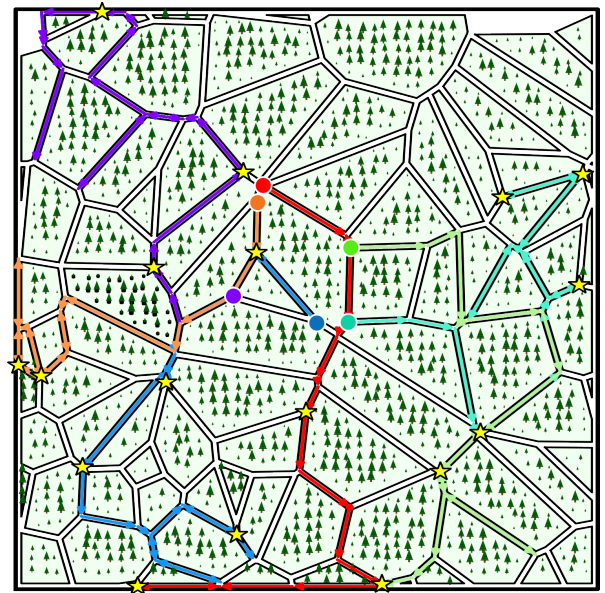


Figure 9. Example VRPTW environment with planned robot trajectories. The designated locations are shown by yellow stars. The initial positions of the robots are marked by the colored circles. Different colored paths represent trajectories for different robots visiting designated locations within their time windows.

duration:

$$\varphi_{\text{vrptw}} = \bigwedge_{t=1}^K \bigvee_{r=1}^R (\diamondsuit_{[0, T]} \square_{[0, 2]} \pi_k^{r, t}) \quad (23)$$

where $\pi_k^{r, t}$ is a predicate indicating robot r is at the target location specified for task t at time step k .

The second specification captures sequencing dependencies between robots, where one robot must first reach a location — like pressing a button — before another can access a different location, such as passing through a door. This coordination is expressed as:

$$\varphi_{\text{sequential}} = \bigwedge_{i=1}^{N_{\text{seq}}} \bigvee_{r_1, r_2 \in R} ((\neg \pi_k^{r_2, B^i} \mathcal{U} \pi_k^{r_1, A^i}) \wedge (\diamondsuit_{[0, T]} \square_{[0, 2]} \pi_k^{r_2, B^i})) \quad (24)$$

where $\pi_k^{r_1, A^i}$ indicates robot r_1 is at location A^i , $\pi_k^{r_2, B^i}$ indicates robot r_2 is at location B^i , R is the set of all robots, and N_{seq} denotes the number of sequential dependencies. For each sequential constraint i , there must exist some pairs of robots (r_1, r_2) such that robot r_2 eventually reaches location B^i , but the “until” operator \mathcal{U} ensures that robot r_2 cannot reach location B^i until robot r_1 has reached location A^i .

We conduct a series of experiments with increasing problem size. The first scenario involves 3 robots serving 9 tasks over a planning horizon of $T = 50$ on a temporal graph containing 93 vertices and 264 edges. We then scale up to 6 robots handling 18 tasks with $T = 70$ on a temporal graph containing 182 vertices and 534 edges. Random experiments are run across 50 trials for each problem setup to ensure statistical significance. Task locations are randomly selected from the vertices of our graph model. To model varying traversal difficulty, we assign random costs to the edges of the DNF following a uniform distribution in $[0, 1]$, where

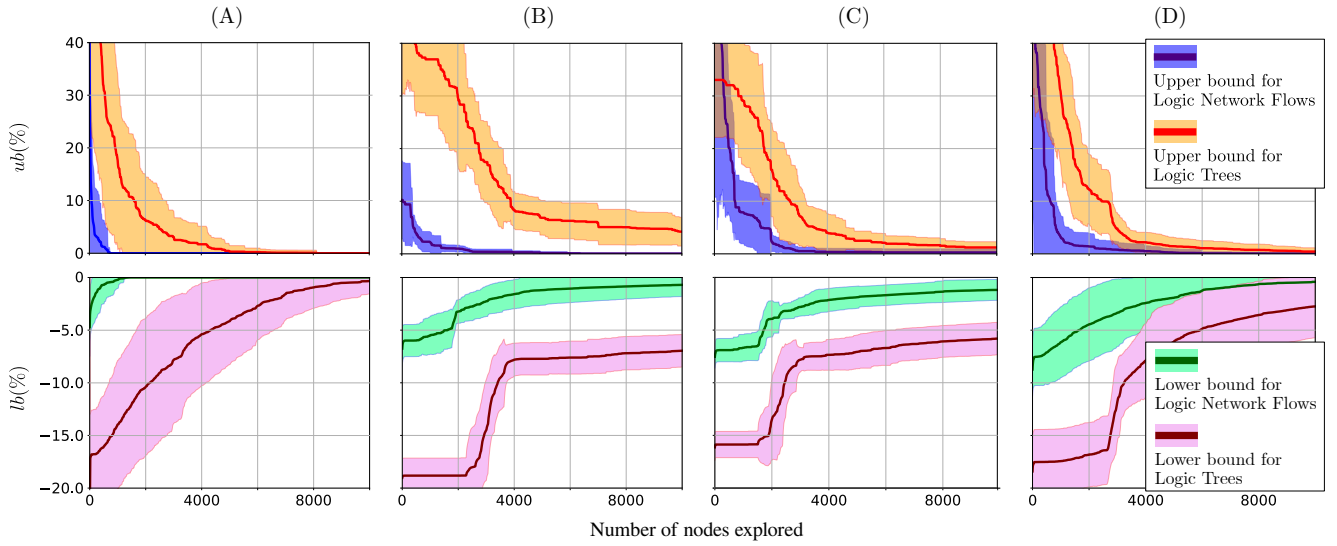


Figure 10. Solved upper and lower bounds plotted against the number of nodes explored during the B&B process for four tasks, demonstrating the comparison between LNF and LT. Shaded regions show the variance. In general, LNF discovers the same bound by exploring less number of nodes. Four figures on the top show the upper bounds in percentage values, computed by $(\text{upper_bound} - \text{global_optimum})/\text{global_optimum} \times 100\%$. The bottom four figures show the lower bounds in percentage values, computed by $(\text{lower_bound} - \text{global_optimum})/\text{global_optimum} \times 100\%$. (A) shows φ_{vrptw} with 3 Robots, 9 Tasks and $T = 50$; (B) shows φ_{vrptw} with 6 Robots, 18 Tasks and $T = 70$; (C) shows $\varphi_{\text{sequential}}$ with 3 Robots, 9 Tasks and $T = 50$; and (D) shows $\varphi_{\text{sequential}}$ with 6 Robots, 18 Tasks and $T = 60$.

higher costs represent more traversal difficulties, such as rougher terrain or higher wind gusts. We also introduce costs uniformly sampled from $[0, 1]$, assigned to the self-loop edges. This represents costs incurred even when a robot remains stationary, such as extreme environmental temperature. Similar to the previous experiment, we compare our LNF formulation against (Kurtz and Lin 2021).

Results Table 3 and 4 show the computational results for φ_{vrptw} and $\varphi_{\text{sequential}}$ specifications, respectively, across different problem sizes over 50 trials. The table reports the number of binary and continuous variables, and the number of constraints for each specification using LNF and LT formulations. The row “ G_r ” records the root relaxation gap between the relaxed MILP formulations and the global optimal solution as explained in Section 3.5. By analyzing the solver logs, we track several key performance metrics: “T-Find (10% gap)” denotes the time to discover a solution within 10% of optimality, “T-Find (optimal)” shows when the global optimal solution is first found, “T-Prove (10% gap)” indicates the time to prove a 10% optimality gap, and “T-Prove (optimal)” represents the total time to prove global optimality. Due to the exponential worst-case complexity leading to high variance in solving times, all timing results are reported as *median \pm median absolute deviation*. In addition, Fig. 10 shows the upper and lower bounds discovered by the Gurobi solver, plotted against the number of nodes explored during the B&B process. These plots demonstrate the efficacy of discovering bounds through the B&B process, regardless of the size of convex relaxations.

Our results indicate that optimization with LNFs is more effective than that with LTs in finding better upper and lower bounds, which is evidenced by the significant reduction in the number of nodes explored to achieve bounds of the same quality. We again attribute this to the tighter

convex relaxations allowing the B&B algorithm to prune the search tree more efficiently and avoid unnecessary exploration of suboptimal regions. This efficacy enables LNF formulations to solve consistently faster than LTs across all problem sizes tested, achieving tenfold speedups overall. Remarkably, for all 200 instances tested (50 trials across four different planning problems), LNF demonstrates faster solving speeds than LT. We also note that the network-based Fourier-Motzkin (F-M) elimination process is essential to the significant speedup. As shown in Table 3, the F-M elimination reduces the number of continuous variables by orders of magnitude (e.g., from 1,524,490 to 48,994 for the 6-robot VRPTW case), while maintaining the same relaxation tightness. Our preliminary work (Lin et al. 2025) shows that LNF formulations without F-M elimination outperform LT for problems with approximately 10^4 continuous variables. However, LT becomes faster for larger problem scales due to its fewer continuous variables. The F-M elimination addresses this limitation by reducing the number of variables and constraints by orders of magnitude, and therefore maintaining LNF’s computational advantage even for large-scale problems. Importantly, the solver tends to find high-quality solutions (within 10% of optimality) much faster than proving global optimality, which may be sufficient for many practical applications requiring real-time planning.

6.2 Path Planning with Trajectory Libraries: A Search and Rescue Application

We showcase a practical application of our framework combining LNF and DNF with a multi-robot search and rescue scenario, where three bipedal robots coordinate to complete multiple missions simultaneously in a disastrous environment. We demonstrate that our LNF formulation of logic specifications discovers optimal coordination plans

Table 3. Computation results for specification φ_{vrptw} with different problem sizes in 50 trials (timeout limit: 10,000 seconds)

		φ_{vrptw} 3 Robots, 9 Tasks, T=50				φ_{vrptw} 6 Robots, 18 Tasks, T=70			
		LNF	LNF-w/o F-M	LT	Speed -up	LNF	LNF-w/o F-M	LT	Speed -up
# of binary vars		245	245	245	N.A.	1242	1242	1242	N.A.
# of cont. vars		17645	242800	17656	N.A.	48994	1524490	49013	N.A.
# of constr.		9614	241264	11897	N.A.	26376	1527738	32283	N.A.
G_r (%)		6.7	6.7	31.2		8.1	8.1	38.0	
		\pm	\pm	\pm	N.A.	\pm	\pm	\pm	N.A.
		3.1	3.1	4.3		2.0	2.0	1.7	
Gurobi	T-Find (10% gap)	1.1	266.0	5.7		49.2	2580.9	1178.8	
		\pm	\pm	\pm	5×	\pm	\pm	\pm	24×
		0.4	89.5	2.3		5.3	1161.4	244.9	
	T-Find (optimal)	1.8	643.8	22.6		570.0			
		\pm	\pm	\pm	12×	\pm	<i>Timeout</i>	<i>Timeout</i>	>18×
		0.6	329.1	14.9		245.9			
	T-Prove (10% gap)	1.2	337.7	22.4		49.4	3675.0	1990.6	
		\pm	\pm	\pm	19×	\pm	\pm	\pm	40×
		0.4	117.3	14.5		6.5	893.3	810.0	
	T-Prove (optimal)	1.7	1202.6	52.9		779.2			
		\pm	\pm	\pm	31×	\pm	<i>Timeout</i>	<i>Timeout</i>	>13×
		0.8	849.9	34.6		409.8			
CPLEX	T-Prove (optimal)	13.0		4475.7		1127.0			
		\pm	<i>Timeout</i>	\pm	344×	\pm	<i>Timeout</i>	<i>Timeout</i>	>9×
		9.6		3501.7		566.0			

Table 4. Computation results for specification $\varphi_{\text{sequential}}$ with different problem sizes in 50 trials (timeout limit: 10,000 seconds)

		$\varphi_{\text{sequential}}$ 3 Robots, 9 Tasks, T=50				$\varphi_{\text{sequential}}$ 6 Robots, 18 Tasks, T=60			
		LNF	LNF-w/o F-M	LT	Speed -up	LNF	LNF-w/o F-M	LT	Speed -up
# of binary vars		475	475	475	N.A.	1035	1035	1035	N.A.
# of cont. vars		16903	235403	16914	N.A.	41967	1085247	41986	N.A.
# of constr.		9853	243678	21361	N.A.	23637	1113762	53889	N.A.
G_r (%)		16.7	16.7	37.2		18.4	18.4	40.1	
		\pm	\pm	\pm	N.A.	\pm	\pm	\pm	N.A.
		2.7	2.7	3.7		2.0	2.0	1.9	
Gurobi	T-Find (10% gap)	10.1	320.8	59.8		62.2	418.6	600.5	
		\pm	\pm	\pm	6×	\pm	\pm	\pm	10×
		4.3	51.9	30.3		16.7	177.5	314.7	
	T-Find (optimal)	32.6	1345.6	339.7		432.5			
		\pm	\pm	\pm	10×	\pm	<i>Timeout</i>	<i>Timeout</i>	>23×
		20.0	626.5	158.6		127.0			
	T-Prove (10% gap)	14.1	893.7	226.3		195.8	1970.3	1833.9	
		\pm	\pm	\pm	16×	\pm	\pm	\pm	9×
		6.8	387.4	59.1		80.2	29.7	728.2	
	T-Prove (optimal)	55.5	2694.0	437.2		1664.2			
		\pm	\pm	\pm	8×	\pm	<i>Timeout</i>	<i>Timeout</i>	>6×
		38.5	1017.9	234.7		1105.7			
CPLEX	T-Prove (optimal)	42.1		595.7		5837.0			
		\pm	<i>Timeout</i>	\pm	14×	\pm	<i>Timeout</i>	<i>Timeout</i>	>2×
		17.6		276.7		2553.0			

significantly faster than the baseline LT approach, enabling rapid mission planning for time-critical applications such as disaster response.

The experiment runs on a $100 \text{ m} \times 100 \text{ m}$ disaster zone covering multiple mission sites including crashed airplanes, factory plants or woods on fire, a search crew base camp, a helicopter landing zone, and multiple obstacles, as illustrated in Fig. 11 (A). The mission objective is to coordinate three bipedal robots to execute: (1) search and rescue operations by reaching two aircraft crash sites to rescue survivors and transport them to the helicopter for medical evacuation, (2) retrieval of critical equipment from two damaged factory plants back to the base camp, and (3) wildfire extinguishing tasks, all within specified time windows. Let $\pi_k^{i,j}$ denote the predicate that the i^{th} robot, $i \in \{1, 2, 3\}$, is at location j at time step k , where the locations include: p_1 (*Factory1*), p_2 (*Factory2*), p_3 (*Airplane1*), p_4 (*Airplane2*), p_5 (*Forest1*), p_6 (*Forest2*), p_7 (*Camp*), and p_8 (*Helicopter*). The task specification for the overall mission is designed as:

$$\phi_{\text{mission}} = \bigwedge_{j=1}^5 \phi_{\text{mission}(j)}$$

where the factory and airplane rescue missions require one robot visiting the task locations, staying there for a specified duration to complete the operations, and then transporting the survivors or retrieving equipment back to the designated search crew base within the time window T_w :

$$\phi_{\text{mission}(j)} = \bigvee_{i=1}^3 \left(\diamond_{[0,T]} \left(\square_{[0,4]} \pi_k^{i,p_j} \wedge \square_{[T_w, T_w+4]} \pi_k^{i,p_{\text{dest}(j)}} \right) \right)$$

where $j \in \{1, 2, 3, 4\}$ corresponds to $p_{\text{dest}(1)} = p_6$, $p_{\text{dest}(2)} = p_6$, $p_{\text{dest}(3)} = p_7$, $p_{\text{dest}(4)} = p_7$, respectively. The fire extinguishing mission requires the robot to visit the forest areas and stay for a period of time to extinguish the fire:

$$\phi_{\text{mission}5} = \left(\bigvee_{i=1}^3 \diamond_{[0,T]} \square_{[0,4]} \pi_k^{i,p_4} \right) \wedge \left(\bigvee_{i=1}^3 \diamond_{[0,T]} \square_{[0,4]} \pi_k^{i,p_5} \right)$$

To construct a DNF for this environment, the map is discretized into a 10×10 grid, excluding grid points that overlap with obstacles. The remaining points serve as vertices in the temporal graph. We build an offline-generated trajectory library to connect these vertices on the map. For each grid vertex, nonlinear trajectory optimizations are employed to find collision-free paths connecting a vertex to all reachable neighboring vertices. Specifically, we optimize dynamically feasible footstep sequences based on the Linear Inverted Pendulum (LIP) model (Koolen et al. 2012). Each obstacle is conservatively approximated as a circular region that circumscribes it, and obstacle avoidance is enforced by constraining the robot's CoM trajectory to remain outside these circle regions. We select a discretization of time of $dT = 16$ seconds to ensure reasonable edge traversal time steps and maintain a manageable planning horizon $T = 50$ and $T_w = 25$. Since each robot undertakes independent

mission plans, we construct 3 separate DNFs to find a path for each robot. Each DNF contains 87 vertices and 470 edges per time step. The full optimization formulation includes 726 binary variables, 81,456 continuous variables, and 26,964 constraints.

The objective function is designed to incorporate two types of risk-aware locomotion costs: one models the risk of falls, which is associated with terrain roughness, and the other is related to time-varying overheating risk that measures the potential for mechanical or electronic failure due to severe fire intensity. The first cost is imposed when the robot moves from one site to the next, while the second is imposed regardless of the robot's motion status (i.e., either in motion or standing pose). To model the terrain roughness, we leverage multi-modal Gaussian distributions randomly placed on the map that range from zero to the maximum roughness level. Fig. 11 (B) and (C) show two roughness distribution examples.

To account for the first type of costs, roughness values are queried along the robot's trajectory path. The probability of failure is assumed to be scaled proportionally to the terrain roughness, and then integrated along the path. We then convert it to log-probability space, making the risks additive across trajectory segments. The terrain cost for each edge is computed as the negative log-probability of successful traversal:

$$\theta_{\text{traversal}}(e) = -\log(1 - p_{\text{fail}}(e))$$

where $p_{\text{fail}}(e)$ represents the probability of failure for the traverse of the edge e based on the roughness of the terrain.

To measure the second type of risk, we model disaster sources centered at each fire location, with severity decreasing exponentially with distance. These costs vary over time, following distinct evolution patterns as shown in Fig. 11 (D): The factories exhibit pulsing behavior due to periodic chemical explosions, aircraft crash sites show increasing fire intensity, and forest fires display diminishing intensity over time. Fig. 11 (D) also shows the spatial distribution of the risk of overheating at the beginning. The cost function sums the severity contributions of all disaster sources at each vertex and time step. The probability of failure is proportional to the severity with an appropriate scaling factor. The cost of staying at the vertex v at time step k is:

$$\theta_{\text{hold}}(v, k) = -\log(1 - p_{\text{fail}}(v, k))$$

where $p_{\text{fail}}(v, k)$ is the probability of failure due to overheating at the vertex v at time step k .

Results We compare LNF and LT formulations solved by Gurobi 12.0 on two problem instances with different terrain roughness patterns. The solved trajectories are shown in Fig. 11 (B) and (C). As expected, both formulations find the same globally optimal solution, with their key distinction in computational efficiency. In the first terrain configuration, the optimal solution assigns Robot 1 to handle the forest fire missions first, then to retrieve equipment from the first factory house, and finally to return to the base camp. Robot 3 sequentially investigates both crash sites to rescue survivors and transports them to the helicopter landing zone. While *Factory2* is located near the aircraft crash sites, assigning all nearby tasks to Robot 3 would exceed the time constraints.

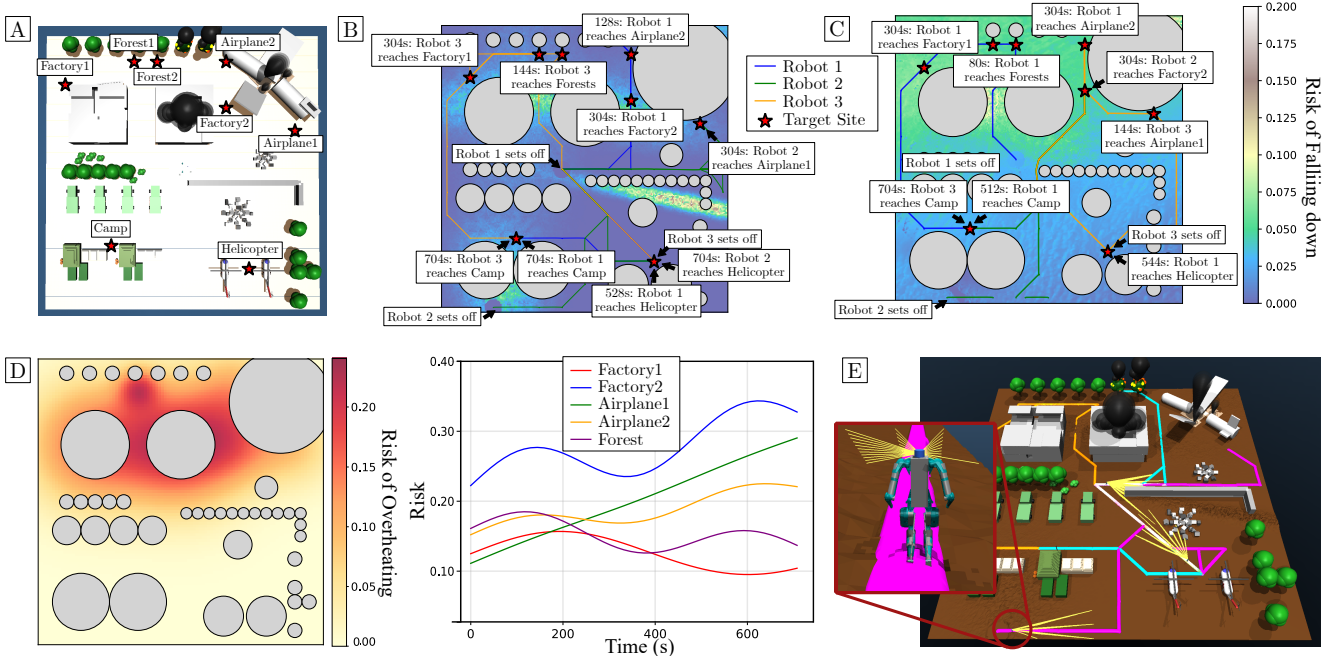


Figure 11. Search and rescue mission planning with three bipedal robots in a disaster environment. (A) Overview of the 100×100 m disaster zone containing mission targets: crashed airplane at (40 m, 16 m), factory houses on fire at (-40 m, 32 m) and (16 m, 24 m), trees on fire at (-8 m, 40 m) and (-16 m, 40 m), search crew base camp at (-24 m, -24 m), and helicopter landing zone at (24 m, -32 m). Red stars indicate target locations, with walls, debris, and trees serving as obstacles. (B,C) Optimized robot trajectories for two terrain profiles with distinct roughness patterns. Color intensity represents risk of falling due to terrain roughness. Three robots start from (-8 m, 0 m), (-24 m, -24 m), and (24 m, -32 m) respectively, with arrival times labeled at each target. (D) Spatial distribution of overheating risk across the disaster zone at $t = 0$. The accompanying plot on the right shows the time-varying overheating risk profiles for different locations: *Factory1*, *Factory2*, *Airplane1*, *Airplane2*, *Forest1*, and *Forest2*. (E) MuJoCo simulation of bipedal robot Digit executing planned trajectory using ALIP-based controller. Planned paths are shown in light blue, orange, and magenta.

Therefore, Robot 2 is tasked with the second factory house rescue mission. Time spent near *Factory1* is minimized because of its high terrain roughness.

In contrast, the optimal task assignment and paths for the second terrain are adjusted to avoid the highly rough terrain region in the middle-right of the map. As a result, Robot 3, which was previously assigned airplane rescue tasks, now takes over the forest fire missions and factory house operations. This shift causes Robot 1 to be reassigned to airplane rescue operations and the *Factory2* mission. Since the disaster severity grows at the airplane crash sites, the robots prioritize these missions to avoid prolonged exposure to escalating risks. On the other hand, because the factories demonstrate periodic risk patterns, the robots intelligently avoid high-risk areas by waiting until the danger subsides before accessing those regions.

The computational results again reveal a significant performance advantage of LNF over LT. For the first terrain configuration, LNF achieves $4\times$ speedups in both global optimality (165 s vs 632 s) and 10%-optimal solutions (39 s vs 165 s). For the second terrain configuration, LNF finds the global optimum in 69 seconds while LT exceeds 3000 seconds (over $40\times$ faster), and achieves $5\times$ speedup for 10%-optimal solutions (44 s vs 213 s). These results highlight that LNF's tighter convex relaxations (58% and 68%, versus 90% and 91% for LT) enabling the solver to find lower-risk robot paths within a shorter time.

Additionally, we simulate the search and rescue scenario in a MuJoCo environment (see the attached video

submission). The bipedal robots use controllers based on the Angular Momentum Linear Inverted Pendulum model (Gong and Grizelle 2022) to execute the planned paths, as shown in Fig. 11 (E). This implementation exhibits that the optimized trajectories are realistically tractable for bipedal systems to navigate complex environments while maintaining balance and satisfying all temporal logic specifications.

6.3 Optimal Motion Planning with PWA System using Point Mass Model

We evaluate our LNF formulation on motion planning with PWA dynamics under STL specifications. In this section, we feature a simple point mass model as the underlying dynamic system, where the system state is $\mathbf{x}_k = [x_k, y_k, \dot{x}_k, \dot{y}_k]^\top \in \mathbb{R}^4$ representing the 2D position and velocity of the robot. The control input $\mathbf{u}_k = [u_{x,k}, u_{y,k}]^\top \in \mathbb{R}^2$ represents the input forces in the x and y directions. We design two environments of increasing complexity: the first environment is a $6 \text{ m} \times 5 \text{ m}$ workspace which is decomposed into 8 collision-free convex regions, and the second environment is an $11 \text{ m} \times 5 \text{ m}$ workspace divided into 15 collision-free convex regions, as shown in Fig. 12. We adopt the big-M formulation (21) for collision-avoidance constraints and introduce binary variables $\delta_{i,k} \in \{0, 1\}$ to indicate whether the robot occupies region i at time step k . This guarantees that at each time step the robot's position lies within exactly one convex region.

The temporal logic specifications involve sequential dependency constraints with multiple target pairs. For

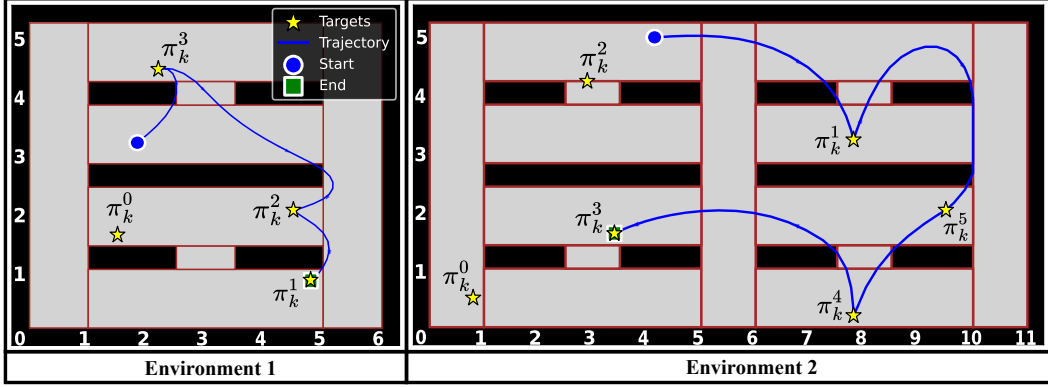


Figure 12. Point mass navigation environments used for evaluating hybrid dynamics under temporal logic specifications. Gray regions represent collision-free areas, yellow stars indicate target points, and the blue trajectory shows the optimized path from start (blue circle) to end (green square) position satisfying the sequential dependency constraints.

Environment 1, we randomly sample 4 targets from different convex regions and create 2 sequential pairs, while environment 2 includes 6 targets constituting 3 sequential pairs. The specification for Environment 1 is:

$$\begin{aligned} \phi_{M1} = & (\neg \pi_k^0 \cup \pi_k^1) \wedge (\neg \pi_k^2 \cup \pi_k^3) \wedge \diamond_{[0,T]} \pi_k^1 \wedge \diamond_{[0,T]} \pi_k^3 \wedge \\ & (\diamond_{[0,T]} \square_{[0,3]} \pi_k^0 \vee \diamond_{[0,T]} \square_{[0,3]} \pi_k^2) \end{aligned} \quad (25)$$

where π_k^i denotes the predicate encoding that the robot visits the target point i at time step k , requiring that target 1 must be visited before target 0, and target 3 before target 2. The specification also requires the robot to visit all prerequisite targets (π_k^1 and π_k^3) and at least one of the subsequent targets (π_k^0 or π_k^2) must eventually be visited and dwelled at for 3 time steps. Environment 2 extends this pattern with

$$\begin{aligned} \phi_{M2} = & (\neg \pi_k^0 \cup \pi_k^1) \wedge (\neg \pi_k^2 \cup \pi_k^3) \wedge (\neg \pi_k^4 \cup \pi_k^5) \wedge \\ & \diamond_{[0,T]} \pi_k^1 \wedge \diamond_{[0,T]} \pi_k^3 \wedge \diamond_{[0,T]} \pi_k^5 \wedge \\ & (\diamond_{[0,T]} \square_{[0,3]} \pi_k^0 \vee \diamond_{[0,T]} \square_{[0,3]} \pi_k^2 \vee \diamond_{[0,T]} \square_{[0,3]} \pi_k^4) \end{aligned} \quad (26)$$

adding a third sequential pair while maintaining the disjunctive choice between subsequent targets. We use a discretization time step of $dT = 0.5$ seconds with planning horizons of $T = 60$ time steps for both environments.

To ensure fair comparisons, we execute 50 trials for each environment, with initial conditions randomly sampled on the map but within a specified convex region. We also build a target visit cost Θ , incurring the cost of visiting each target, uniformly sampled between 0 and 1, modeling preferences for specific task completion locations and times due to factors such as lower operational risk. The state cost matrix is $Q = \mathbf{0}$ and the control cost matrix is $R = \text{diag}([1, 1])$ to penalize the control input. We compare our LNF formulation with the baseline LT formulation using the big M method, which aligns with optimization-based formulations for temporal logic control, as presented in Eqn. 15 in (Belta and Sadraddini 2019).

Results The results for point mass navigation in two environments are shown in the first (ϕ_{M1}) and second (ϕ_{M2}) columns of Table 6. Similar to previous experiments, we report the number of binary and continuous variables, constraints, root relaxation gap, and various timing metrics. In addition, we present speed summary results that indicate the number of trials (out of 50) where LNF is faster,

LT is faster, or the performance is similar (within a 20% difference).

For the point-mass environments, LNF outperforms LT across both problem sizes. In environment 1 (ϕ_{M1}), LNF achieves better root relaxation gaps (36.5% vs 41.0%) and demonstrates clear computational advantages, with LNF being faster in 44 of 50 trials compared to only two trials where LT is faster. The speedups range from $2.5 \times$ to $3.0 \times$ across different timing metrics. Environment 2 (ϕ_{M2}) shows a similar pattern, but with slightly reduced advantages as problem complexity increases: LNF is faster in 36 of 50 trials versus 4 for LT, with 10 trials showing a similar computational speed. The speedups remain substantial at $1.7 \times$ to $3.3 \times$, though LT slightly outperforms LNF in finding the optimal solution ($0.9 \times$ speedup for T-Find optimal).

6.4 Optimal Motion Planning with PWA System using Inverted Pendulum Model

To further evaluate more realistic robot models, we study bipedal footstep planning using a 3-D LIP model (Deits and Tedrake 2014). While existing LIP-based approaches such as (Deits and Tedrake 2014) typically plan optimal footsteps towards predefined goal states, our framework generates footstep sequences to reach several locations of interest under temporal logic specifications. The system state $\mathbf{x}_k = [x, y, \dot{x}, \dot{y}, \theta]^\top \in \mathbb{R}^5$ includes the CoM position, velocity, and heading angle. The control input $\mathbf{u}_k = [u_x, u_y, \omega]^\top \in \mathbb{R}^3$ represents the footstep placement relative to the CoM in the x and y directions, and the angular velocity for the heading angle change. We use the discrete time LIP dynamics developed by (Narkhede et al. 2022), where the dynamics represent walking-step-to-walking-step evolution of the robot’s CoM:

For $i \in \{x, y\}$:

$$\begin{bmatrix} s_{k+1}^i \\ \dot{s}_{k+1}^i \end{bmatrix} = \begin{bmatrix} 1 & \frac{1}{\omega} \sinh(\omega dT) \\ 0 & \cosh(\omega dT) \end{bmatrix} \begin{bmatrix} s_k^i \\ \dot{s}_k^i \end{bmatrix} + \begin{bmatrix} 1 - \cosh(\omega dT) \\ -\omega \sinh(\omega dT) \end{bmatrix} u_k^i \quad (27a)$$

$$\theta_{k+1} = \theta_k + dT \omega_k \quad (27b)$$

The discrete transition from the k^{th} step to the $k+1^{\text{th}}$ step represents a contact transition, where H is the CoM

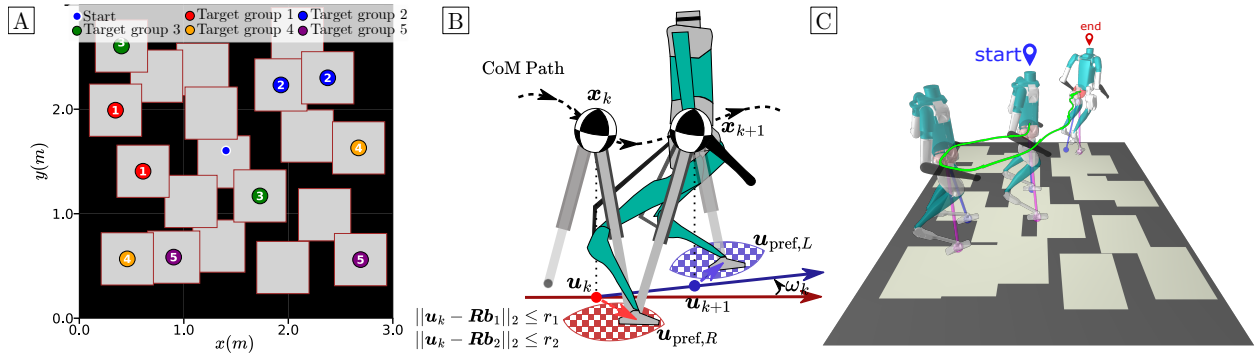


Figure 13. Bipedal locomotion planning with Linear Inverted Pendulum (LIP) dynamics under STL specifications. (A) Environment setup: The $3 \text{ m} \times 3 \text{ m}$ workspace is decomposed into 20 safe contact regions ($0.5 \text{ m} \times 0.5 \text{ m}$ squares with overlap, shown in light gray). Five target groups are defined, each containing 2 regions labeled with matching colors and numbers 1-5. The STL specification requires the robot to visit at least one target region from each group. (B) Kinematic feasibility constraints: Footstep placement is constrained by the intersection of two circles representing the reachable regions for left and right feet, with preferred footstep positions $u_{\text{pref},(L/R)}$ indicated. (C) Planning results: The optimized center-of-mass (CoM) trajectory is shown as a green curve, with the bipedal walking gait illustrated using LIP models superimposed along the trajectory. Each LIP model shows the CoM position (center) and corresponding left and right foot contact locations.

height, $\omega = \sqrt{g/H}$ is the natural frequency of the pendulum, and dT is the time interval between consecutive footsteps. We introduce additional binary variables to discretize the heading angle into $n_\theta = 4$ segments, approximating sinusoidal functions using piecewise linear functions (Deits and Tedrake 2014):

$$\sum_{q=1}^{n_\theta} \lambda_{k,q} = 1, \quad \lambda_{k,q} \in \{0, 1\} \quad (28a)$$

$$\theta_{\min,q} - M(1 - \lambda_{k,q}) \leq \theta_k \leq \theta_{\max,q} + M(1 - \lambda_{k,q}) \quad (28b)$$

$$|s_t - (m_{s,q}\theta_k + b_{s,q})| \leq M(1 - \lambda_{k,q}) \quad (28c)$$

$$|c_t - (m_{c,q}\theta_k + b_{c,q})| \leq M(1 - \lambda_{k,q}) \quad (28d)$$

where $\lambda_{k,q}$ indicates if the segment q is active at time step k , $s_k = \sin(\theta_k)$ and $c_k = \cos(\theta_k)$, $[\theta_{\min,q}, \theta_{\max,q}]$ define the angular range for the segment q , and $(m_{s,q}, b_{s,q}), (m_{c,q}, b_{c,q})$ are the linear approximation coefficients for sine and cosine functions, respectively, within segment q .

For each foot, two circular bounds b_1 and b_2 , with radius r_1 and r_2 , are used to delineate feasible regions for footstep placement. The contact location u_k must stay within the intersection of these two circles:

$$\|u_k - \mathbf{R}(\theta_k)b_1\|_2 \leq r_1 \quad \text{and} \quad \|u_k - \mathbf{R}(\theta_k)b_2\|_2 \leq r_2 \quad (29)$$

To ensure safe locomotion, we define 20 discrete foot contact regions within which the robot can safely place its footsteps. Regions outside these designated areas are considered unsafe due to factors such as slippery surfaces, excessively rough terrain, or unsteppable objects. These safe regions are uniformly distributed within a $3 \text{ m} \times 3 \text{ m}$ workspace with some overlap. The safe contact regions are represented as light gray boxes in Fig. 13 (A). We enforce the restriction that each footstep must be placed within one of these predefined safe regions.

The PWA dynamics formulation for safe bipedal locomotion incorporates several constraint types: LIP dynamics (27), kinematic feasibility (29), discretized

Table 5. Key parameters for the LIP experiment

Parameter	Symbol	Value
Height of COM	H	1.0 m
Time discretization interval	dT	0.5 s
Natural frequency	ω	$\sqrt{g/H} = 3.13 \text{ rad/s}$
Preferred left/right footstep	$u_{\text{pref},(L/R)}$	$[0, \pm 0.15] \text{ m}$
Circle 1 center (left/right foot)	b_1	$[0, \pm 1]^\top \text{ m}$
Circle 2 center (left/right foot)	b_2	$[0, \mp 2.5]^\top \text{ m}$
Circle 1 radius	r_1	0.9 m
Circle 2 radius	r_2	3.1 m

orientation (28), and safe contact regions that ensure foot placement occurs within predefined safe areas using big-M constraints.

Additionally, we predefine desired contact positions $u_{\text{pref},(L/R)}$ relative to CoM for each foot to maintain nominal foot placement. Fig. 13 (B) illustrates the feasible footstep region defined by the intersection of the kinematic constraint circles along with these preferred contact positions. The objective function minimizes the deviation between actual footstep placements and these preferred positions, while also incorporating region occupancy costs:

$$f_{\text{obj}} = \sum_{k=0}^{N-1} \|u_k - u_{\text{pref},(L/R)}\|^2 + \Theta^\top z^\pi \quad (30)$$

Similar to all previous experiments, Θ represents the predicate costs uniformly sampled from $[0, 1]$, modeling preferences for specific task completion locations and times due to factors such as lower operational risk. The key parameters for the LIP model are summarized in Table 5.

The temporal logic specification requires the bipedal robot to visit at least one target location from each of five distinct target groups within the planning horizon of $T = 25$ time steps with $dT = 0.5$ seconds. Each target location corresponds to a specific safe contact region, and the robot must walk at least two footsteps into the selected region to complete the visit. Each group contains 2 target regions. This

Table 6. Computation results for PWA with temporal logic specifications in 50 trials (timeout limit: 10,000 seconds)

		ϕ_{M1} T=60, 4 targets			ϕ_{M2} T=60, 6 targets			ϕ_{LIP} T=25, 10 targets		
		LNF	LT	Speed-up	LNF	LT	Speed-up	LNF	LT	Speed-up
# bin. vars		732	732	N.A.	1281	1281	N.A.	624	624	N.A.
# cont. vars		598	602	N.A.	715	720	N.A.	497	503	N.A.
# constr.		6899	14724	N.A.	11847	23261	N.A.	3300	3778	N.A.
G_r (%)		36.5	41.0		54.0	57.3		14.4	34.8	
		±	±	N.A.	±	±	N.A.	±	±	N.A.
		12.2	9.9		8.8	9.4		6.6	7.3	
Gurobi	T-Find (10%)	2.1	5.7		2.9	4.9		17.6	23.0	
		±	±	2.7 ×	±	±	1.7 ×	±	±	1.3 ×
		0.9	2.1		1.4	0.4		6.6	18.7	
	T-Find (opt)	7.2	18.0		32.8	28.4		111.8	99.6	
		±	±	2.5 ×	±	±	0.9 ×	±	±	0.9 ×
	T-Prove (10%)	5.8	11.7		26.6	23.6		76.5	70.1	
		32.9	88.6		98.7	323.0		31.7	37.5	
		±	±	2.7 ×	±	±	3.3 ×	±	±	1.2 ×
	T-Prove (opt)	26.2	67.6		76.2	279.4		28.9	33.3	
		48.0	142.2		138.2	348.0		163.5	115.6	
		±	±	3.0 ×	±	±	2.5 ×	±	±	0.7 ×
		37.2	101.6		103.9	299.0		126.9	87.3	
CPLEX	T-Prove (opt)	483.9	894.6		Timeout	Timeout	N.A.	Timeout	Timeout	N.A.
		±	±	1.8 ×	Timeout	Timeout	N.A.	Timeout	Timeout	N.A.
		228.3	232.8							
Speed summary		LNF faster	LT faster	Similar	LNF faster	LT faster	Similar	LNF faster	LT faster	Similar
		44/50	2/50	4/50	36/50	4/50	10/50	23/50	20/50	7/50

Note: Speed comparison criteria: faster indicates >20% speedup, similar speed indicates <20% difference.

specification is formulated as:

$$\phi_{LIP} = \bigwedge_{i=1}^5 \left(\bigvee_{j \in G_i} \diamondsuit_{[0,T]} \square_{[0,1]} \pi_k^j \right) \quad (31)$$

where G_i represents the set of region indices in the target group i (with $|G_i| = 2$ for each group), and π_k^j denotes the predicate indicating the robot occupies region j at time step k . The target group assignments are illustrated in Fig. 13 (A). Similar to the point mass case, we randomly generate 50 trials by uniformly sampling initial positions within one of the safe regions. For each problem, we solve using our LNF formulation and benchmark against the baseline LT formulation.

Results The optimized locomotion plan, including the center-of-mass trajectory and a few footstep placements, is shown in Fig. 13 (C). Computational efficiency results are presented in the third column (ϕ_{LIP}) of Table 6. While LNF continues to achieve significantly tighter root relaxation gaps (14.4% vs 34.8%), the computational advantages become more modest compared to the point mass cases. The speed summary shows a nearly even split: LNF is faster in 23 out of 50 trials, LT is faster in 20 trials, and 7 trials show similar performance. Individual timing metrics reveal speedups ranging from 0.7× to 1.3×, indicating that neither method consistently outperforms the other. This diminished computational advantage occurs because the complex hybrid dynamics formulation—including piecewise linear trigonometric approximations, kinematic feasibility

constraints, and footstep placement restrictions—becomes the primary computational bottleneck. While LNF’s tighter logic formulation still provides benefits, the dynamics constraints now dominate the overall solution time, limiting the impact of logic formulation improvements on total computational performance.

Discussion These results on hybrid dynamic systems such as point mass and LIP, combined with our earlier planning experiments on temporal graph structures, reveal a clear trend: the simpler the dynamic model is, the greater advantage our LNF formulation provides. In the graph-based planning problems, where dynamics are abstracted as simple transitions between discrete states, LNF achieved the most substantial speedups of up to several orders of magnitude. The point mass navigation problem with big-M constraints represents an intermediate complexity, showing 2-3× speedups. The LIP model for locomotion, with its complex trigonometric approximations, shows the most modest improvements despite the tighter relaxation gaps. These results suggest that LNF’s computational benefits are most pronounced when temporal logic constraints constitute the primary computational bottleneck. When dynamics become complex, decomposition approaches such as Benders Decomposition (Ren et al. 2025) can still leverage LNF’s computational advantages, where LNF can handle the temporal logic and simplified dynamics in the master problem while delegating complex dynamics to subproblems.

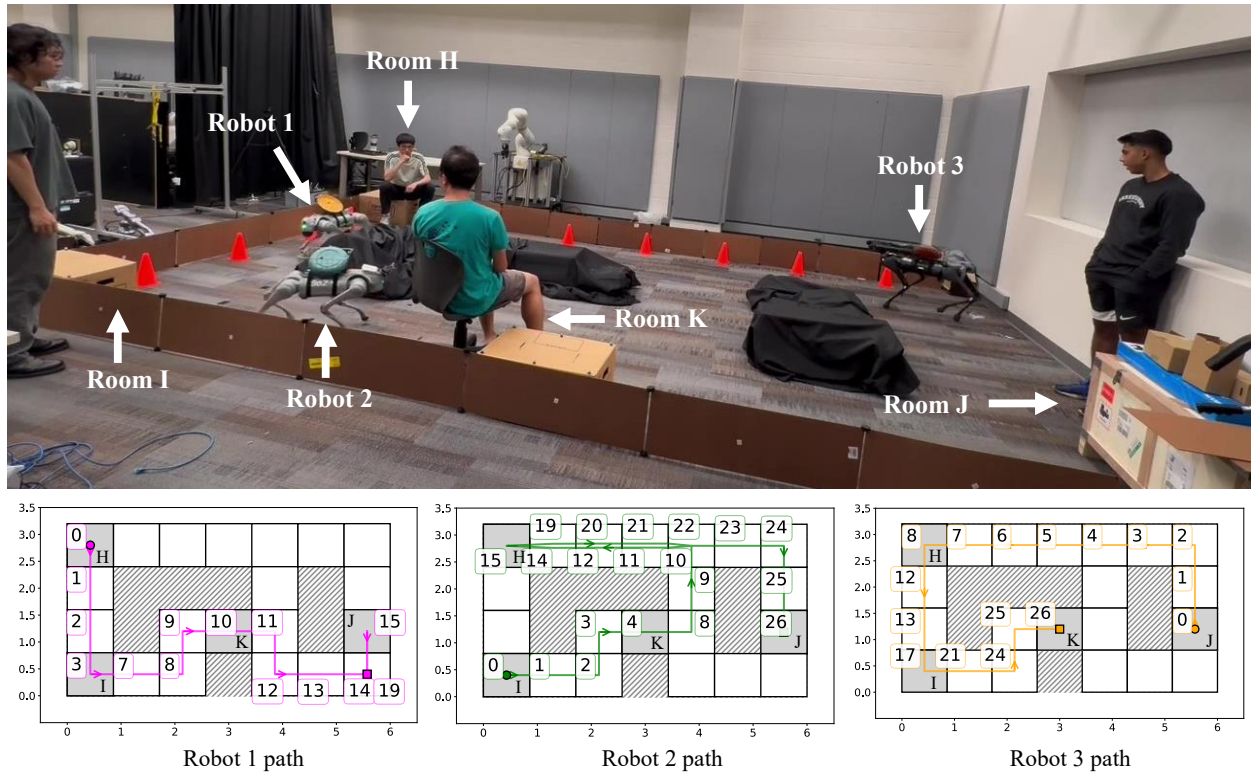


Figure 14. Top: Physical robot demonstration setup showing three robots with labeled task rooms H, I, J, and K. Bottom: Computed trajectories for Robot 1 (magenta), Robot 2 (green), and Robot 3 (orange) with time annotations ($k = 0$ to 29) showing the planned paths through the grid. Arrows indicate direction of motion along each path.

6.5 Real-Time Replanning with Multiple Quadrupedal Robots

We demonstrate the temporal logic motion planning as well as the real-time replanning capabilities of our LNF framework with two hardware experiments. The first experiment involves three quadrupedal robots targeting object delivery tasks with sequential ordering and collision avoidance requirements (see Fig. 14). The second experiment studies a single quadrupedal robot that must visit a disjunction of targets while dynamically avoiding unforeseen triangular traffic cones detected by an onboard camera (see Fig. 15), showing instant replanning capabilities under dynamically changing environmental conditions.

The hardware experiments are run by Unitree quadrupedal robots with an overhead motion capture system providing real-time robot position and orientation status. The robots navigate in a confined workspace populated with static obstacles. A Euclidean-space PID controller regulates the linear velocities in the horizontal plane and the yaw angular velocity to accurately track the planned trajectories.

For the first experiment in Fig. 14, we implement Formulation 1.3 for multi-robot coordination. We set up a workspace with dimensions $6 \text{ m} \times 3 \text{ m}$, discretized into 21 regions of equal size. The environment designated four areas, labeled H, I, J, and K, to represent spots where the staff collect different components to assemble products. Three quadrupedal robots carry the necessary objects with delivery deadlines T_1 , T_2 , and T_3 , respectively. The robots start from the designated positions: Robot 1 at room H, Robot 2 at room I, and Robot 3 at room J. The assembly processes require robots to arrive at each room in a specific sequence to

ensure proper assembly: room H requires Robot 3 to arrive first, followed by Robot 2; room I requires Robot 1 to be the first one to show up and then Robot 3, room J requires Robot 1 first followed by Robot 2, and room K requires Robot 2 first followed by Robot 3. For each visit, the robot stays for 2 time units to allow the staff to pick up the object from the robots. The temporal logic specification of this task is:

$$\begin{aligned} \phi_{\text{task}} = & (\Diamond_{[0, T_1]} \Box_{[0, 2]} \pi_k^{1 \rightarrow I}) \wedge (\Diamond_{[0, T_1]} \Box_{[0, 2]} \pi_k^{1 \rightarrow J}) \wedge \\ & (\Diamond_{[0, T_2]} \Box_{[0, 2]} \pi_k^{2 \rightarrow H}) \wedge (\Diamond_{[0, T_2]} \Box_{[0, 2]} \pi_k^{2 \rightarrow J}) \wedge \\ & (\Diamond_{[0, T_2]} \Box_{[0, 2]} \pi_k^{2 \rightarrow K}) \wedge (\Diamond_{[0, T_3]} \Box_{[0, 2]} \pi_k^{3 \rightarrow H}) \wedge \\ & (\Diamond_{[0, T_3]} \Box_{[0, 2]} \pi_k^{3 \rightarrow I}) \wedge (\Diamond_{[0, T_3]} \Box_{[0, 2]} \pi_k^{3 \rightarrow K}) \wedge \\ & (\neg \pi_k^{2 \rightarrow H} \mathcal{U} \pi_k^{3 \rightarrow H}) \wedge (\neg \pi_k^{2 \rightarrow J} \mathcal{U} \pi_k^{1 \rightarrow J}) \wedge \\ & (\neg \pi_k^{3 \rightarrow I} \mathcal{U} \pi_k^{1 \rightarrow I}) \wedge (\neg \pi_k^{3 \rightarrow K} \mathcal{U} \pi_k^{2 \rightarrow K}) \end{aligned}$$

where $\pi_k^{1 \rightarrow I}$ represents Robot 1 visiting room I at time step k , and so on.

The four rooms are positioned in separate locations connected by narrow hallways with a T-shaped junction at the center. Robots need to coordinate their passing order at the junction to avoid congestion. We assign costs to both the robot's movement through hallways and its waiting time in rooms. These time-varying costs reflect factors such as rooms having limited staff availability at certain times (e.g., during breaks) and hallways experiencing varying congestion throughout the day.

In the first experiment, three Unitree quadruped robots are deployed to execute the planned trajectories, where each robot is assigned a temporal graph. Each cell in Fig. 14

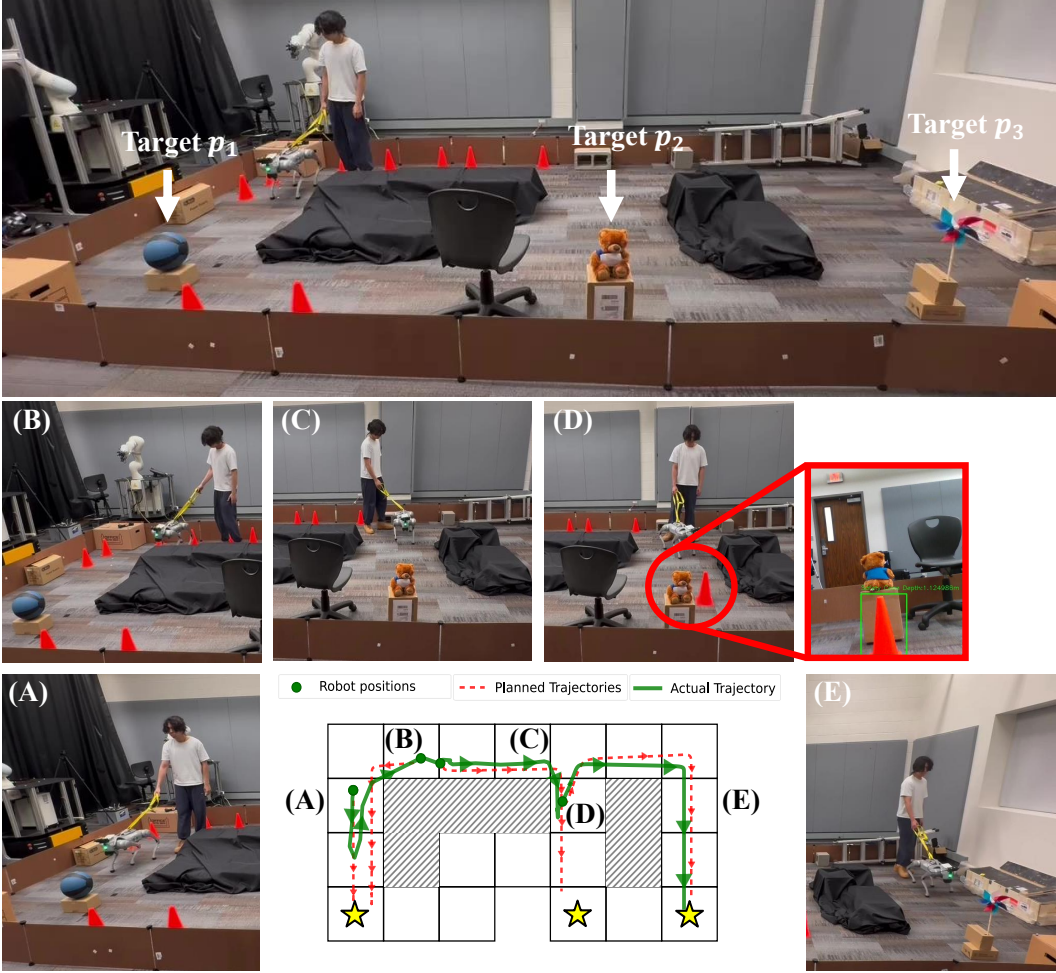


Figure 15. A quadrupedal robot navigates toward three potential target locations (p_1, p_2, p_3) with continuous replanning under STL specifications. The central trajectory plot shows the robot’s planned paths (red dotted lines) at several key instants with green dots indicating robot positions, and actual executed trajectory (green solid line). (A) The robot initially plans a path toward target p_1 . (B) A human operator physically drags the robot backward, and the replanning drives the robot toward target p_2 (C) as a more optimal choice given the new position. (D) A cone obstacle is placed in the robot’s path, which is recognized by the onboard RGB-D camera (highlighted in red box), making target p_2 infeasible. (E) The robot automatically replans and successfully reaches the new optimal goal, i.e., target p_3 .

is represented by a vertex in the graph. Adjacent cells are connected by edges. We set the capacity of any edge to 1 such that two robots cannot simultaneously traverse the same edge or occupy the same cell. We choose a planning horizon $T = 30$ and build the according DNF. To prevent collisions between robots, we implement the conflict set constraints described in Section V-B. Specifically, we define conflict sets for each vertex containing robot-vertex pairs that prevent multiple robots from occupying the same location, and conflict sets for each bidirectional edge containing robot-edge pairs that prevent head-to-head collisions, then enforcing (20).

Results We solve the problem using Gurobi 12.0, which contains 6,054 variables (5,655 binary, 399 continuous) and 5,829 constraints. The optimizer finds the globally optimal trajectories for all three robots within 8 seconds, as shown in Fig. 14. In addition, we deploy the optimized trajectories on real quadrupedal robots (see the submission video). The hardware demonstration validates that the robots successfully deliver components following the sequential ordering constraints and timing requirements specified in

the STL specification, while avoiding collisions with other robots.

For the second experiment, we use the exactly same environment as the first experiment and implement LNF integrated with a continuous configuration space PWA system for real-time temporal logic replanning. A single quadrupedal robot must select from 3 disjunctive goals. Rather than using Formulation 1.4, we use Bézier curves to model the robot’s CoM trajectory, as remarked in Remark 6. Only CoM motion is needed to plan paths for quadrupedal robots, and using Bézier curves reduces problem dimensionality by representing smooth trajectories through a small number of control points. Note that the specific choice of dynamics formulation does not affect the validation of our method, as the LNF is the core contribution that we validate.

We use two Bézier curves: one degree-3 Bézier curve for $x - y$ position and one degree-1 curve for time scaling, to model robot motion. Collision avoidance with the environment is ensured through the convex hull property of Bézier curves. The formulation includes initial position and velocity constraints enforced through the 0th and 1st order

derivatives of the position Bézier curve, which also enforces the robot's initial orientation by assuming it aligns with the velocity direction. This approach significantly reduces problem dimensionality by representing smooth trajectories through a small number of control points. For details of the Bézier curve formulation, we refer readers to the work in (Marcucci et al. 2023).

Integration with LNF is achieved using binary edge variables y_{ij}^k as predicate variables, similar to the DNF formulation in (19). To enable this mapping, we add constraints ensuring that traversing each region takes a fixed duration Δt , so that the discrete time steps of y_{ij}^k correspond to actual time intervals $[k\Delta t, (k+1)\Delta t]$. In future work, we plan to relax this uniform timing constraint to allow variable region traversal times. We designate 3 target regions p_1 , p_2 , p_3 , and the STL specification requires the robot to visit at least one of them with a minimum dwell time. The temporal logic specification is:

$$\phi_{\text{replanning}} = \bigvee_{i \in \{p_1, p_2, p_3\}} \diamondsuit_{[0, T]} \square_{[0, 1]} \pi_k^i \quad (32)$$

The planner runs in a model predictive control fashion, continuously replanning as initial conditions and the environment change. We introduce two types of disturbances to demonstrate adaptive goal selection based on optimization feasibility and cost: manual perturbations where a person drags the robot to different locations, and traffic control cone obstacles suddenly showing up during robot motion. The Go2 robot is equipped with an Intel RealSense RGB-D camera, which detects cone positions in the 3D space. The cone positions are transformed into global coordinates using the robot's own pose, providing the absolute location of cones in the environment. The replanning algorithm then adds constraints $y_{ij}^k = 0, \forall k$ to any edge entering cells within a 1-meter blocking radius of the cone, removing those regions from the feasible path options. The objective function minimizes the path length while applying an exponential time penalty α^k ($\alpha > 1$) for delayed goal completion. Specifically, when the robot reaches the goal region and remains there at time step k , a penalty of α^k is added to the objective, discouraging late arrivals at target locations. The optimization model is built only once and resolved with changing initial conditions, leveraging Gurobi's internal warm-start capability to accelerate the computation. The warm-start provides a speedup of around 10% for this specific case.

Results We conduct multiple trials as demonstrated in the submitted video, where the robot initially plans to pursue a goal and automatically switches targets due to human interference and dynamic obstacles. Throughout the process, the planner continuously operates and generates a series of trajectories in real-time. Fig. 15 shows one representative behavior. Initially, the planner drives the robot toward target 1 (subfigure (A)). When a person drags the robot back significantly, moving it farther from target 1 (subfigure (B)), the robot automatically switches to pursue target 2 as that new target becomes more optimal (subfigure (C)). During the approach to target 2, a person places a cone obstacle in the robot's path, making target 2 infeasible (subfigure (D)). The robot quickly responds and redirects itself to target 3 instead

(subfigure (E)). Overall, the system maintains a 2 – 10 Hz replanning frequency.

It is worth noting that the continuous replanning demonstrated here is designed to showcase the system's rapid response capabilities. In practice, event-driven replanning triggered by obstacle detection or human intention recognition would be more appropriate, as our current implementation can introduce unnecessary replanning causing the robot to oscillate between different trajectories.

7 Discussion

7.1 LNF Performance with Solver Presolve and Heuristics

Modern MIP solvers employ presolve techniques — such as the introduction of valid inequalities — to tighten formulations and reduce the number of variables and constraints. These procedures benefit both LNF and LT formulations. In our experiments, the reported convex relaxation gaps are measured after presolve, as they reflect the actual formulations processed by the solver. Our experiments demonstrate that the advantages of LNF formulations, endowed by their tighter convex relaxations and reduced number of constraints, hold consistently with or without presolve.

While LNF provides tighter relaxations, MIP solvers continue to rely on heuristics to identify feasible binary solutions. Although we have not systematically investigated this, a hybrid formulation incorporating LT constraints (15e) and (15f) into the LNF formulation may potentially enhance solver heuristics for handling complex logic specifications.

7.2 Reduction of Memory Usage

Though we do not comprehensively evaluate memory efficiency across all problem instances, for many test cases, we observe a reduction in memory usage when using LNF compared to LT formulations. For the point mass navigation model ϕ_{M1} in Section 6.3, we monitor CPU and memory usage using the standard monitoring tool `psrecord`. Although memory usage generally grows during solving for both formulations, LNF consistently exhibits lower consumption for the most of the cases.

In a typical scenario of ϕ_{M1} , LNF solve the problem in 65 seconds with peak memory usage of approximately 450 MB occurring at the end of its solving process. At the same instant, LT has already consumed 550 MB while still searching for the solution. Moreover, LT ultimately requires 610 seconds to solve the problem, with memory consumption reaching 872 MB at termination.

This reduction is due to a combination of fewer constraints in the problem formulation and the faster solving time. The smaller model size requires less memory for storage, while the faster solving time implies that fewer B&B nodes to be managed during the optimization process. With these reduced memory requirements, LNF models are better suited for embedded applications on mobile robots where computational resources are limited.

8 Conclusion and Future Work

In this paper, we present LNF, a novel optimization formulation that encodes temporal logic specifications as network flow constraints inspired by the GCS framework, along with a network-flow-based Fourier-Motzkin elimination procedure that projects the formulation onto a lower-dimensional space. LNF achieves provably tighter convex relaxations compared to the standard LT approach while reducing the number of constraints. Experimental results demonstrate computational speedups ranging from $2 - 3 \times$ for complex dynamics to orders of magnitude for Temporal-Graph-based planning problems. Hardware experiments with quadrupedal robots validate the framework's real-time replanning capabilities under dynamically changing environmental conditions.

Future research directions include integrating LNF with decomposition approaches such as Benders Decomposition (Ren et al. 2025), where LNF focuses on solving simplified dynamics in the master problem while complicated dynamics are handled in subproblems. Additionally, developing theoretical bounds on the expected relaxation improvement for specific problem classes would provide more performance guarantees. The network-flow-based Fourier-Motzkin elimination procedure also shows promise for simplifying other GCS formulations beyond temporal logic, suggesting broader applicability across motion planning and hybrid control problems.

Acknowledgements

The authors are grateful to Prof. Samuel Coogan for his valuable support and guidance throughout this work. The authors would also like to thank the members of the Laboratory for Intelligent Decision and Autonomous Robots (LIDAR) and other colleagues at the Georgia Institute of Technology for their valuable discussions and assistance with the experiments.

Author Contributions

All authors contributed to the study. Xuan Lin: Conceptualization, Methodology, Formal analysis, Investigation, Software, Project administration, Writing – original draft. Jiming Ren: Methodology, Software, Visualization, Writing – review & editing. Yandong Luo: Investigation, Software, Writing – review & editing. Weijun Xie: Supervision. Ye Zhao: Funding acquisition, Resources, Supervision. All authors reviewed and approved the final version of the manuscript.

Ethical Considerations

Not applicable.

Consent to Participate

Not applicable.

Consent for Publication

Not applicable.

Declaration of conflicting interests

The author(s) declared no potential conflicts of interest with respect to the research, authorship, and/or publication of this article.

Funding

The author(s) disclosed receipt of the following financial support for the research, authorship, and/or publication of this article: This work was supported in part by the Office of Naval Research (ONR) under Grant N000142312223; in part by the National Science Foundation (NSF) under Grant IIS-1924978, Grant CMMI-2144309, and Grant FRR-2328254.

References

Ahuja RK, Magnanti TL and Orlin JB (1994) *Network flows: theory, algorithms and applications*. Prentice hall.

Aronson JE (1989) A survey of dynamic network flows. *Annals of Operations Research* 20(1): 1–66.

Baier C and Katoen JP (2008) *Principles of model checking*. MIT press.

Belta C and Sadraddini S (2019) Formal methods for control synthesis: An optimization perspective. *Annual Review of Control, Robotics, and Autonomous Systems* 2(1): 115–140.

Belta C, Yordanov B and Gol EA (2017) *Formal methods for discrete-time dynamical systems*, volume 89. Springer.

Bemporad A and Morari M (1999) Control of systems integrating logic, dynamics, and constraints. *Automatica* 35(3): 407–427.

Brihaye T, Geeraerts G, Ho HM and Monmege B (2017) MightyL: A compositional translation from mtl to timed automata. In: *Proceedings of International Conference on Computer Aided Verification*. Springer, pp. 421–440.

Cao ME, Ni X, Warnke J, Han Y, Coogan S and Zhao Y (2022) Leveraging heterogeneous capabilities in multi-agent systems for environmental conflict resolution. In: *2022 IEEE International Symposium on Safety, Security, and Rescue Robotics (SSRR)*. IEEE, pp. 94–101.

Cardona GA, Kamale D and Vasile CI (2023a) Mixed integer linear programming approach for control synthesis with weighted signal temporal logic. In: *Proceedings of ACM International Conference on Hybrid Systems: Computation and Control*. Association for Computing Machinery.

Cardona GA, Leahy K and Vasile CI (2023b) Temporal logic swarm control with splitting and merging. In: *2023 IEEE International Conference on Robotics and Automation (ICRA)*. IEEE, pp. 12423–12429.

Coleman D, Sucan IA, Moll M, Okada K and Correll N (2015) Experience-based planning with sparse roadmap spanners. In: *2015 IEEE International Conference on Robotics and Automation (ICRA)*. IEEE, pp. 900–905.

Conforti M, Cornuéjols G, Zambelli G, Conforti M, Cornuéjols G and Zambelli G (2014) *Integer programming models*. Springer.

Deits R and Tedrake R (2014) Footstep planning on uneven terrain with mixed-integer convex optimization. In: *2014 IEEE-RAS international conference on humanoid robots*. IEEE, pp. 279–286.

Fainekos GE and Pappas GJ (2009) Robustness of temporal logic specifications for continuous-time signals. *Theoretical Computer Science* 410(42): 4262–4291.

Gastin P and Oddoux D (2001) Fast ltl to büchi automata translation. In: *Computer Aided Verification: 13th International Conference, CAV 2001 Paris, France, July 18–22, 2001 Proceedings* 13. Springer, pp. 53–65.

Gilpin Y, Kurtz V and Lin H (2020) A smooth robustness measure of signal temporal logic for symbolic control. *IEEE Control Systems Letters* 4(1): 10–14.

Systems Letters 5(1): 241–246.

Gong Y and Grizzle JW (2022) Zero dynamics, pendulum models, and angular momentum in feedback control of bipedal locomotion. *Journal of Dynamic Systems, Measurement, and Control* 144(12): 121006.

Gu Z, Guo R, Yates W, Chen Y, Zhao Y and Zhao Y (2024) Walking-by-logic: Signal temporal logic-guided model predictive control for bipedal locomotion resilient to external perturbations. In: *2024 IEEE International Conference on Robotics and Automation (ICRA)*. IEEE, pp. 1121–1127.

Gu Z, Zhao Y, Chen Y, Guo R, Leestma JK, Sawicki GS and Zhao Y (2025) Robust-locomotion-by-logic: Perturbation-resilient bipedal locomotion via signal temporal logic guided model predictive control. *IEEE Transactions on Robotics*.

He K, Lahijanian M, Kavraki LE and Vardi MY (2015) Towards manipulation planning with temporal logic specifications. In: *2015 IEEE international conference on robotics and automation (ICRA)*. IEEE, pp. 346–352.

Huang JK and Grizzle JW (2023) Efficient anytime clif reactive planning system for a bipedal robot on undulating terrain. *IEEE Transactions on Robotics* 39(3): 2093–2110.

Jackson P and Sheridan D (2004) Clause form conversions for boolean circuits. In: *International Conference on Theory and Applications of Satisfiability Testing*. Springer, pp. 183–198.

Jiang J, Coogan S and Zhao Y (2023) Abstraction-based planning for uncertainty-aware legged navigation. *IEEE Open Journal of Control Systems* 2: 221–234.

Kantaros Y and Zavlanos MM (2020) Stylus*: A temporal logic optimal control synthesis algorithm for large-scale multi-robot systems. *The International Journal of Robotics Research* 39(7): 812–836.

Karaman S and Frazzoli E (2008) Vehicle routing problem with metric temporal logic specifications. In: *2008 47th IEEE conference on decision and control*. IEEE, pp. 3953–3958.

Karp RM (2010) *Reducibility among combinatorial problems*. Springer.

Kloetzer M and Belta C (2009) Automatic deployment of distributed teams of robots from temporal logic motion specifications. *IEEE Transactions on Robotics* 26(1): 48–61.

Kooleen T, De Boer T, Rebula J, Goswami A and Pratt J (2012) Capturability-based analysis and control of legged locomotion, part 1: Theory and application to three simple gait models. *The international journal of robotics research* 31(9): 1094–1113.

Kress-Gazit H, Conner DC, Choset H, Rizzi AA and Pappas GJ (2008) Courteous cars. *IEEE Robotics & Automation Magazine* 15(1): 30–38.

Kress-Gazit H, Eder K, Hoffman G, Admoni H, Argall B, Ehlers R, Heckman C, Jansen N, Knepper R, Křetínský J, Levy-Tzedek S, Li J, Murphey T, Riek L and Sadigh D (2021) Formalizing and guaranteeing human-robot interaction. *Communications of the ACM* 64(9): 78–84.

Kress-Gazit H, Fainekos GE and Pappas GJ (2009) Temporal-logic-based reactive mission and motion planning. *IEEE transactions on robotics* 25(6): 1370–1381.

Kuindersma S, Deits R, Fallon M, Valenzuela A, Dai H, Permenter F, Kooleen T, Marion P and Tedrake R (2016) Optimization-based locomotion planning, estimation, and control design for the atlas humanoid robot. *Autonomous robots* 40: 429–455.

Kurtz V and Lin H (2021) A more scalable mixed-integer encoding for metric temporal logic. *IEEE Control Systems Letters* 6: 1718–1723.

Kurtz V and Lin H (2022) Mixed-integer programming for signal temporal logic with fewer binary variables. *IEEE Control Systems Letters* 6: 2635–2640.

Kurtz V and Lin H (2023) Temporal logic motion planning with convex optimization via graphs of convex sets. *IEEE Transactions on Robotics*.

Leung K, Aréchiga N and Pavone M (2023) Backpropagation through signal temporal logic specifications: Infusing logical structure into gradient-based methods. *The International Journal of Robotics Research* 42(6): 356–370. DOI:10.1177/02783649221082115.

Li S, Park D, Sung Y, Shah JA and Roy N (2021) Reactive task and motion planning under temporal logic specifications. In: *2021 IEEE International Conference on Robotics and Automation (ICRA)*. IEEE, pp. 12618–12624.

Lin X, Ren J, Coogan S and Zhao Y (2025) Optimization-based task and motion planning under signal temporal logic specifications using logic network flow. In: *2025 IEEE International Conference on Robotics and Automation (ICRA)*. IEEE, pp. 12565–12571.

Lin X, Zhang J, Shen J, Fernandez G and Hong DW (2019) Optimization based motion planning for multi-limbed vertical climbing robots. In: *2019 IEEE/RSJ International Conference on Intelligent Robots and Systems (IROS)*. IEEE, pp. 1918–1925.

Liu J, Ozay N, Topcu U and Murray RM (2013) Synthesis of reactive switching protocols from temporal logic specifications. *IEEE Transactions on Automatic Control* 58(7): 1771–1785.

Marcucci T (2024) *Graphs of Convex Sets with Applications to Optimal Control and Motion Planning*. PhD Thesis, MASSACHUSETTS INSTITUTE OF TECHNOLOGY.

Marcucci T, Petersen M, von Wrangel D and Tedrake R (2023) Motion planning around obstacles with convex optimization. *Science robotics* 8(84): eadf7843.

Marcucci T and Tedrake R (2019) Mixed-integer formulations for optimal control of piecewise-affine systems. In: *Proceedings of ACM International Conference on Hybrid Systems: Computation and Control*. pp. 230–239.

Mehdipour N, Vasile CI and Belta C (2019) Average-based robustness for continuous-time signal temporal logic. In: *Proceedings of IEEE Conference on Decision and Control*. IEEE, pp. 5312–5317.

Narkhede KS, Kulkarni AM, Thanki DA and Poulakakis I (2022) A sequential mpc approach to reactive planning for bipedal robots using safe corridors in highly cluttered environments. *IEEE Robotics and Automation Letters* 7(4): 11831–11838.

Pant YV, Abbas H, Quaye RA and Mangharam R (2018) Fly-by-logic: Control of multi-drone fleets with temporal logic objectives. In: *2018 ACM/IEEE 9th International Conference on Cyber-Physical Systems (ICCP)*. IEEE, pp. 186–197.

Piterman N, Pnueli A and Sa'ar Y (2006) Synthesis of reactive (1) designs. In: *Verification, Model Checking, and Abstract Interpretation: 7th International Conference, VMCAI 2006, Charleston, SC, USA, January 8–10, 2006. Proceedings* 7. Springer, pp. 364–380.

Plaku E and Karaman S (2016) Motion planning with temporal-logic specifications: Progress and challenges.

AI communications 29(1): 151–162.

Raman V, Donzé A, Sadigh D, Murray RM and Seshia SA (2015) Reactive synthesis from signal temporal logic specifications. In: *Proceedings of the 18th international conference on hybrid systems: Computation and control*. pp. 239–248.

Raman V, Maasoumy M and Donzé A (2014) Model predictive control from signal temporal logic specifications: A case study. In: *Proceedings of ACM SIGBED International Workshop on Design, Modeling, and Evaluation of Cyber-Physical Systems*. pp. 52–55.

Ren J, Lin X, Mineyev R, Feigh KM, Coogan S and Zhao Y (2025) Accelerating signal-temporal-logic-based task and motion planning of bipedal navigation using benders decomposition. *arXiv preprint arXiv:2508.13407*.

Ren J, Miller H, Feigh KM, Coogan S and Zhao Y (2024) Ltl-d*: Incrementally optimal replanning for feasible and infeasible tasks in linear temporal logic specifications. In: *2024 IEEE/RSJ International Conference on Intelligent Robots and Systems (IROS)*. IEEE, pp. 4495–4502.

Scher G and Kress-Gazit H (2020) Warehouse automation in a day: from model to implementation with provable guarantees. In: *2020 IEEE 16th International Conference on Automation Science and Engineering (CASE)*. IEEE, pp. 280–287.

Schillinger P, Bürger M and Dimarogonas DV (2018) Simultaneous task allocation and planning for temporal logic goals in heterogeneous multi-robot systems. *The international journal of robotics research* 37(7): 818–838.

Shamsah A, Gu Z, Warnke J, Hutchinson S and Zhao Y (2023) Integrated task and motion planning for safe legged navigation in partially observable environments. *IEEE Transactions on Robotics*.

Shamsah A, Jiang J, Yoon Z, Coogan S and Zhao Y (2025) Terrain-aware model predictive control of heterogeneous bipedal and aerial robot coordination for search and rescue tasks. In: *2025 IEEE International Conference on Robotics and Automation (ICRA)*. IEEE, pp. 12352–12358.

Smith SL, Tůmová J, Belta C and Rus D (2011) Optimal path planning for surveillance with temporal-logic constraints. *The International Journal of Robotics Research* 30(14): 1695–1708.

Sontag E (1981) Nonlinear regulation: The piecewise linear approach. *IEEE Transactions on automatic control* 26(2): 346–358.

Sun D, Chen J, Mitra S and Fan C (2022) Multi-agent motion planning from signal temporal logic specifications. *IEEE Robotics and Automation Letters* 7(2): 3451–3458.

Ulusoy A, Smith SL, Ding XC, Belta C and Rus D (2013) Optimality and robustness in multi-robot path planning with temporal logic constraints. *The International Journal of Robotics Research* 32(8): 889–911.

Wolff EM, Topcu U and Murray RM (2012) Optimal control with weighted average costs and temporal logic specifications. *Proc. of Robotics: Science and Systems VIII* (2012).

Wolff EM, Topcu U and Murray RM (2014) Optimization-based trajectory generation with linear temporal logic specifications. In: *Proceedings of IEEE International Conference on Robotics and Automation*. IEEE, pp. 5319–5325.

Yu J and LaValle SM (2013) Multi-agent path planning and network flow. In: *Algorithmic Foundations of Robotics X: Proceedings of Workshop on the Algorithmic Foundations of Robotics*. Springer, pp. 157–173.

Yu J and LaValle SM (2016) Optimal multirobot path planning on graphs: Complete algorithms and effective heuristics. *IEEE Transactions on Robotics* 32(5): 1163–1177.

Zhao Y, Li Y, Sentis L, Topcu U and Liu J (2022) Reactive task and motion planning for robust whole-body dynamic locomotion in constrained environments. *The International Journal of Robotics Research* 41(8): 812–847.

Zhao Z, Chen S, Ding Y, Zhou Z, Zhang S, Xu D and Zhao Y (2024) A survey of optimization-based task and motion planning: From classical to learning approaches. *IEEE/ASME Transactions on Mechatronics*.

Zhou Z, Lee DJ, Yoshinaga Y, Balakirsky S, Guo D and Zhao Y (2022) Reactive task allocation and planning for quadrupedal and wheeled robot teaming. In: *2022 IEEE 18th International Conference on Automation Science and Engineering (CASE)*. IEEE, pp. 2110–2117.

A Index to Multimedia Extensions

Archives of IJRR multimedia extensions published prior to 2014 can be found at <http://www.ijrr.org>; after 2014 all videos are available on the IJRR YouTube channel at <http://www.youtube.com/user/ijrrmultimedia>

Table of Multimedia Extensions

Extension	Media Type	Description
1	Video	Demonstrations of experimental results, including: (1) Multi-robot search and rescue using trajectory libraries; (2) Bipedal locomotion planning with Linear Inverted Pendulum dynamics under temporal logic constraints; (3) Hardware demonstrations on multiple quadrupedal robots temporal logic planning; (4) Hardware demonstrations on a single quadrupedal robot real-time re-planning under disturbances.

B Rigorous Process of Network-flow-based Fourier-Motzkin Elimination

In this appendix, we present the rigorous F-M elimination procedure that projects the original GCS-inspired formulation onto a lower-dimensional space with fewer continuous variables and constraints. Through systematic variable elimination, this process generates a formulation that is mathematically equivalent to the original model, preserving the same feasible region and optimal solution, and maintaining the same tightness of convex relaxation.

Consider the flow variables ω_e for edges $e \in \mathcal{E}_{v_s}^{\text{out}}$ originating from the source vertex v_s . We eliminate these edge flow variables one edge at a time, treating each $\omega_e \in [0, 1]^{\Pi^1}$ as a batch to be removed.

For edge $e_1 \in \mathcal{E}_{v_s}^{\text{out}}$ that connects to vertex v_1 , we collect all constraints involving ω_{e_1} . From the convex set constraints

(8), and the flow conservation at source (11b), we have:

$$\begin{aligned} y_{e_1} \mathbf{v}_{e_1}^+ &\leq \omega_{e_1} \leq \mathbf{1}_{|\Pi|} - y_{e_1} \mathbf{v}_{e_1}^- \\ z^\pi &= \omega_{e_1} + \sum_{e \in \mathcal{E}_{v_s}^{\text{out}} \setminus \{e_1\}} \omega_e \end{aligned} \quad (33)$$

Let v_1 denote the vertex that e_1 enters, i.e., $e_1 \in \mathcal{E}_{v_1}^{\text{in}}$. From the flow conservation constraint (10b) at v_1 :

$$\omega_{e_1} + \sum_{e \in \mathcal{E}_{v_1}^{\text{in}} \setminus \{e_1\}} \omega_e = \sum_{e \in \mathcal{E}_{v_1}^{\text{out}}} \omega_e$$

Collecting all constraints involving ω_{e_1} , we have the following lower bounds:

$$\omega_{e_1} \geq y_{e_1} \mathbf{v}_{e_1}^+ \quad (34a)$$

$$\omega_{e_1} \geq z^\pi - \sum_{e \in \mathcal{E}_{v_s}^{\text{out}} \setminus \{e_1\}} \omega_e \quad (34b)$$

$$\omega_{e_1} \geq \sum_{e \in \mathcal{E}_{v_1}^{\text{out}}} \omega_e - \sum_{e \in \mathcal{E}_{v_1}^{\text{in}} \setminus \{e_1\}} \omega_e \quad (34c)$$

and upper bounds:

$$\omega_{e_1} \leq \mathbf{1}_{|\Pi|} - y_{e_1} \mathbf{v}_{e_1}^- \quad (35a)$$

$$\omega_{e_1} \leq z^\pi - \sum_{e \in \mathcal{E}_{v_s}^{\text{out}} \setminus \{e_1\}} \omega_e \quad (35b)$$

$$\omega_{e_1} \leq \sum_{e \in \mathcal{E}_{v_1}^{\text{out}}} \omega_e - \sum_{e \in \mathcal{E}_{v_1}^{\text{in}} \setminus \{e_1\}} \omega_e \quad (35c)$$

Following standard F-M elimination, variables ω_{e_1} are cancelled by requiring that each lower bound must be less than or equal to each upper bound. The constraint $y_{e_1} \mathbf{v}_{e_1}^+ \leq \mathbf{1}_{|\Pi|} - y_{e_1} \mathbf{v}_{e_1}^-$ is always satisfied by construction when $y_{e_1} \in \{0, 1\}$ and $\mathbf{v}_{e_1}^+, \mathbf{v}_{e_1}^-$ have disjoint non-zero entries. Therefore, we obtain the following 5 meaningful constraints:

$$y_{e_1} \mathbf{v}_{e_1}^+ \leq z^\pi - \sum_{e \in \mathcal{E}_{v_s}^{\text{out}} \setminus \{e_1\}} \omega_e \quad (36a)$$

$$z^\pi - \sum_{e \in \mathcal{E}_{v_s}^{\text{out}} \setminus \{e_1\}} \omega_e \leq \mathbf{1}_{|\Pi|} - y_{e_1} \mathbf{v}_{e_1}^- \quad (36b)$$

$$y_{e_1} \mathbf{v}_{e_1}^+ \leq \sum_{e \in \mathcal{E}_{v_1}^{\text{out}}} \omega_e - \sum_{e \in \mathcal{E}_{v_1}^{\text{in}} \setminus \{e_1\}} \omega_e \quad (36c)$$

$$\sum_{e \in \mathcal{E}_{v_1}^{\text{out}}} \omega_e - \sum_{e \in \mathcal{E}_{v_1}^{\text{in}} \setminus \{e_1\}} \omega_e \leq \mathbf{1}_{|\Pi|} - y_{e_1} \mathbf{v}_{e_1}^- \quad (36d)$$

$$z^\pi - \sum_{e \in \mathcal{E}_{v_s}^{\text{out}} \setminus \{e_1\}} \omega_e = \sum_{e \in \mathcal{E}_{v_1}^{\text{out}}} \omega_e - \sum_{e \in \mathcal{E}_{v_1}^{\text{in}} \setminus \{e_1\}} \omega_e \quad (36e)$$

The original flow conservation constraint (11b) is replaced by (36a) and (36b). When we proceed to eliminate ω_{e_2} for $e_2 \in \mathcal{E}_{v_s}^{\text{out}} \setminus \{e_1\}$, (36b) provides lower bounds on ω_{e_2} that replace (34b):

$$\omega_{e_2} \geq z^\pi - (\mathbf{1}_{|\Pi|} - y_{e_1} \mathbf{v}_{e_1}^-) - \sum_{e \in \mathcal{E}_{v_s}^{\text{out}} \setminus \{e_1, e_2\}} \omega_e \quad (37)$$

Constraint (36a) provides upper bounds that replace (35b):

$$\omega_{e_2} \leq z^\pi - y_{e_1} \mathbf{v}_{e_1}^+ - \sum_{e \in \mathcal{E}_{v_s}^{\text{out}} \setminus \{e_1, e_2\}} \omega_e \quad (38)$$

When combining with ω_{e_2} 's own convex set constraints, the F-M elimination produces new constraints where the bounds from v_s now include both $y_{e_1} \mathbf{v}_{e_1}^+$ and $y_{e_2} \mathbf{v}_{e_2}^+$ in the lower bounds, and both $(\mathbf{1}_{|\Pi|} - y_{e_1} \mathbf{v}_{e_1}^-)$ and $(\mathbf{1}_{|\Pi|} - y_{e_2} \mathbf{v}_{e_2}^-)$ in the upper bounds. The same pattern continues for the rest of the edges in $\mathcal{E}_{v_s}^{\text{out}}$: each elimination adds the corresponding $y_e \mathbf{v}_e^+$ terms to the lower bound and $(\mathbf{1}_{|\Pi|} - y_e \mathbf{v}_e^-)$ terms to the upper bound. After eliminating all edges from v_s , we obtain exactly constraint (13) from the main text:

$$z^\pi \geq \sum_{e \in \mathcal{E}_{v_s}^{\text{out}}} y_e \mathbf{v}_e^+, \quad z^\pi \leq \sum_{e \in \mathcal{E}_{v_s}^{\text{out}}} (\mathbf{1}_{|\Pi|} - y_e \mathbf{v}_e^-) \quad (39)$$

Furthermore, the original constraint (10b) at v_1 is replaced by (36c) and (36d). As in the proof of Theorem 1, we assume all edges from v_s enter the same vertex v_1 , i.e., $\mathcal{E}_{v_s}^{\text{out}} = \mathcal{E}_{v_1}^{\text{in}}$ (see Fig. 5). With this assumption, constraint (36d) provides lower bounds on ω_{e_2} that replace (34c):

$$\omega_{e_2} \geq \sum_{e \in \mathcal{E}_{v_1}^{\text{out}}} \omega_e - (\mathbf{1}_{|\Pi|} - y_{e_1} \mathbf{v}_{e_1}^-) - \sum_{e \in \mathcal{E}_{v_1}^{\text{in}} \setminus \{e_1, e_2\}} \omega_e \quad (40)$$

Constraint (36c) provides upper bounds that replace (35c):

$$\omega_{e_2} \leq \sum_{e \in \mathcal{E}_{v_1}^{\text{out}}} \omega_e - y_{e_1} \mathbf{v}_{e_1}^+ - \sum_{e \in \mathcal{E}_{v_1}^{\text{in}} \setminus \{e_1, e_2\}} \omega_e \quad (41)$$

The same pattern continues for the rest of the edges in $\mathcal{E}_{v_s}^{\text{out}}$. After eliminating all edges from v_s (which are also all edges entering v_1), we obtain:

$$\sum_{e \in \mathcal{E}_{v_1}^{\text{in}}} y_e \mathbf{v}_e^+ \leq \sum_{e \in \mathcal{E}_{v_1}^{\text{out}}} \omega_e \leq \sum_{e \in \mathcal{E}_{v_1}^{\text{in}}} (\mathbf{1}_{|\Pi|} - y_e \mathbf{v}_e^-) \quad (42)$$

In addition, the equality constraint (36e) simplifies to:

$$z^\pi = \sum_{e \in \mathcal{E}_{v_1}^{\text{out}}} \omega_e \quad (43)$$

The elimination process up to $\mathcal{E}_{v_s}^{\text{out}}$ removes (8) for edges $e \in \mathcal{E}_{v_s}^{\text{out}}$, (11b) at v_s , (10b) at v_1 , and replace them with the new constraints (39), (42), and (43).

We proceed to exclude the flow variables ω_e for edges $e \in \mathcal{E}_{v_1}^{\text{out}}$. Consider an edge $e'_1 \in \mathcal{E}_{v_1}^{\text{out}}$ that connects to vertex v_2 . We have the following constraints involving this edge e'_1 : constraints (42), (43), and the original flow conservation constraint (10b) at the subsequent vertex v_2 . Under a similar assumption as before that all edges outgoing from v_1 enter the same vertex v_2 , i.e., $\mathcal{E}_{v_1}^{\text{out}} = \mathcal{E}_{v_2}^{\text{in}}$, we obtain bounds similar to those for ω_{e_1} with substitutions $e_1 \rightarrow e'_1$, $v_s \rightarrow v_1$, and $v_1 \rightarrow v_2$. Specifically, we have three lower bounds analogous to (34a), (34b), and (34c), three upper bounds analogous to (35a), (35b), and (35c), plus one additional lower bound and one additional upper bound from (42):

$$\omega_{e'_1} \geq \sum_{e \in \mathcal{E}_{v_1}^{\text{in}}} y_e \mathbf{v}_e^+ - \sum_{e \in \mathcal{E}_{v_1}^{\text{out}} \setminus \{e'_1\}} \omega_e \quad (44a)$$

$$\omega_{e'_1} \leq \sum_{e \in \mathcal{E}_{v_1}^{\text{in}}} (\mathbf{1}_{|\Pi|} - y_e \mathbf{v}_e^-) - \sum_{e \in \mathcal{E}_{v_1}^{\text{out}} \setminus \{e'_1\}} \omega_e \quad (44b)$$

For the first three lower bounds and first three upper bounds, the F-M elimination process at vertex v_1 gives the same results as at the source vertex v_s , generating constraints analogous to (39), (42), and (43).

However, in this case we have additional bounds (44a) and (44b), which generate 4 additional constraints:

$$y_{e'_1} \mathbf{v}_{e'_1}^+ \leq \sum_{e \in \mathcal{E}_{v_1}^{\text{in}}} (\mathbf{1}_{|\Pi|} - y_e \mathbf{v}_e^-) - \sum_{e \in \mathcal{E}_{v_1}^{\text{out}} \setminus \{e'_1\}} \omega_e \quad (45a)$$

$$\sum_{e \in \mathcal{E}_{v_1}^{\text{in}}} y_e \mathbf{v}_e^+ - \sum_{e \in \mathcal{E}_{v_1}^{\text{out}} \setminus \{e'_1\}} \omega_e \leq \mathbf{1}_{|\Pi|} - y_{e'_1} \mathbf{v}_{e'_1}^- \quad (45b)$$

$$\sum_{e \in \mathcal{E}_{v_1}^{\text{in}}} y_e \mathbf{v}_e^+ \leq z^\pi \leq \sum_{e \in \mathcal{E}_{v_1}^{\text{in}}} (\mathbf{1}_{|\Pi|} - y_e \mathbf{v}_e^-) \quad (45c)$$

$$\sum_{e \in \mathcal{E}_{v_1}^{\text{in}}} y_e \mathbf{v}_e^+ \leq \sum_{e \in \mathcal{E}_{v_2}^{\text{out}}} \omega_e \leq \sum_{e \in \mathcal{E}_{v_1}^{\text{in}}} (\mathbf{1}_{|\Pi|} - y_e \mathbf{v}_e^-) \quad (45d)$$

We first observe that (45c) is redundant, as it is identical to constraint (39) given our assumption that $\mathcal{E}_{v_s}^{\text{out}} = \mathcal{E}_{v_1}^{\text{in}}$.

Additionally, constraint (45d) is independent of any other flow variables in $\mathcal{E}_{v_1}^{\text{out}}$, and has a similar form to constraint (42) from the elimination at v_s , with the only difference being that $\sum_{e \in \mathcal{E}_{v_2}^{\text{out}}} \omega_e$ replaces $\sum_{e \in \mathcal{E}_{v_1}^{\text{out}}} \omega_e$.

Regarding constraints (45a) and (45b), when we proceed to get rid of $\omega_{e'_2}$ for $e'_2 \in \mathcal{E}_{v_1}^{\text{out}} \setminus \{e'_1\}$, they provide bounds on $\omega_{e'_2}$. When combining with $\omega_{e'_2}$'s own convex set constraints, the F-M elimination yields new constraints where $y_{e'_2} \mathbf{v}_{e'_2}^+$ is added to the accumulated lower bounds and $(\mathbf{1}_{|\Pi|} - y_{e'_2} \mathbf{v}_{e'_2}^-)$ is added to the accumulated upper bounds. The same pattern continues for the rest of the edges $e \in \mathcal{E}_{v_1}^{\text{out}}$. After eliminating all edges from $\mathcal{E}_{v_1}^{\text{out}}$, we obtain two constraints in the form of (14) in the main content.

The elimination process up to $\mathcal{E}_{v_1}^{\text{out}}$ removes constraints (8) for edges $e \in \mathcal{E}_{v_1}^{\text{out}}$, (43) at v_1 , and (10b) at v_2 , retains (42) from the previous step at v_s , and replaces them with new constraints similar to (39), (42), and (43) (with v_s replaced by v_1 and v_1 replaced by v_2), along with (14).

Continuing this elimination process through the network until reaching the final vertex before v_t , denoted v_{t-1} , we systematically eliminate all convex set constraints (8) for edges $e \in \mathcal{E}$, all flow conservation constraints (10b) at vertices $v \in \mathcal{V} \setminus \{v_s, v_t\}$, and the input flow constraint (11b) at v_s .

At each intermediate vertex v_i , we also obtain new constraints analogous to (42), but with $\sum_{e \in \mathcal{E}_{v_i}^{\text{out}}} \omega_e$ in place of $\sum_{e \in \mathcal{E}_{v_1}^{\text{out}}} \omega_e$. These constraints collect the bounds from all previous vertices. When we reach v_{t-1} , the flow conservation ensures $\sum_{e \in \mathcal{E}_{v_{t-1}}^{\text{out}}} \omega_e = z^\pi$. At this point, all these accumulated constraints become redundant as they simply provide bounds on z^π that have already been captured by (39) derived at each v_i , and therefore can be eliminated from the final formulation.

We finally obtain constraints in the form of (39) at each vertex $v \in \mathcal{V} \setminus \{v_t\}$, and constraints in the form of (14) at each vertex $v \in \mathcal{V} \setminus \{v_s, v_t\}$, thus achieving the simplified formulation presented in Section 4.3 of the main text.

C Flow Variable Elimination Preserves the Convex Relaxation Tightness

In this section, we present a lemma showing that replacing constraint (8) and (11b) with (13) preserves the tightness of the convex relaxation.

Lemma 3. *Consider the following optimization problem (denoted by problem A) with flow variables:*

$$\begin{aligned} & \text{minimize}_{z^\pi, y_e, \omega_e \text{ for } e \in \mathcal{E}_{v_s}^{\text{out}}, \xi, \text{ other } y, \omega} f_{\text{obj}}(\xi, z^\pi) \\ & \text{s.t.} \quad z^\pi = \sum_{e \in \mathcal{E}_{v_s}^{\text{out}}} \omega_e \end{aligned} \quad (\text{A1})$$

$$\omega_e \geq y_e \mathbf{v}_e^+, \quad \forall e \in \mathcal{E}_{v_s}^{\text{out}} \quad (\text{A2})$$

other constraints

z^π, y_e are binary variables

This problem has the same tightness of convex relaxation as the following problem after flow variable elimination (denoted by problem B):

$$\begin{aligned} & \text{minimize}_{z^\pi, y_e \text{ for } e \in \mathcal{E}_{v_s}^{\text{out}}, \xi, \text{ other } y, \omega} f_{\text{obj}}(\xi, z^\pi) \\ & \text{s.t.} \quad z^\pi \geq \sum_{e \in \mathcal{E}_{v_s}^{\text{out}}} y_e \mathbf{v}_e^+ \\ & \quad \text{other constraints} \\ & \quad z^\pi, y_e \text{ are binary variables} \end{aligned} \quad (\text{B1})$$

Proof. Consider the convex relaxation of problems A and B, where the binary constraints are removed. We show that the optimal cost $f_A^* = f_B^*$.

To establish that $f_A^* \geq f_B^*$, consider an optimal solution to problem A that satisfies constraints (A1) and (A2). Since constraints (A1) and (A2) can be combined to obtain constraint (B1), any feasible solution to problem A provides a feasible solution to problem B with the same values for all shared variables, including $z^{\pi*}$ and y_e^* . Therefore, $f_A^* \geq f_B^*$.

We next show that $f_A^* \leq f_B^*$. Consider an optimal solution to problem B containing variables $(z^{\pi*}, y_e^*, \dots)$ that satisfy constraint (B1). We show that there exist flow variables ω_e such that $(z^{\pi*}, y_e^*, \omega_e, \dots)$ satisfies constraints (A1) and (A2) of problem A.

To construct such ω_e , define the slack variable $\delta = z^{\pi*} - \sum_{e \in \mathcal{E}_{v_s}^{\text{out}}} y_e^* \mathbf{v}_e^+ \geq 0$, where the inequality follows from (B1). Let $\omega_e = y_e^* \mathbf{v}_e^+ + \delta / |\mathcal{E}_{v_s}^{\text{out}}|$. This construction satisfies constraint (A1):

$$\begin{aligned} \sum_{e \in \mathcal{E}_{v_s}^{\text{out}}} \omega_e &= \sum_{e \in \mathcal{E}_{v_s}^{\text{out}}} (y_e^* \mathbf{v}_e^+ + \delta / |\mathcal{E}_{v_s}^{\text{out}}|) \\ &= \sum_{e \in \mathcal{E}_{v_s}^{\text{out}}} y_e^* \mathbf{v}_e^+ + \delta = z^{\pi*} \end{aligned}$$

and constraint (A2):

$$\omega_e = y_e^* \mathbf{v}_e^+ + \delta / |\mathcal{E}_{v_s}^{\text{out}}| \geq y_e^* \mathbf{v}_e^+$$

Since the objective function is independent of ω_e , any optimal solution to problem B gives a feasible solution to problem A with the same objective value. Therefore, $f_A^* \leq f_B^*$. \square

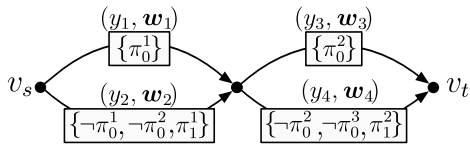


Figure 16. LNF representation for the formula $(\neg z^2 U z^1) \wedge (\neg z^3 U z^2)$ with time steps $k \in \{0, 1\}$.

D Example of Non-trivial Constraints from Flow Conservation

In this appendix, we present a simple example illustrating how non-trivial constraints arise during the F-M process when the same predicate appears with different negation statuses in an LNF.

Consider a system with three predicates z^1, z^2, z^3 , and two time steps $k \in \{0, 1\}$. The specification consists of the temporal logic formula $\varphi = (\neg z^2 U z^1) \wedge (\neg z^3 U z^2)$. For the formula $\neg z^2 U z^1$, the system satisfies this if either $z_0^1 = 1$, or $z_0^1 = 0, z_0^2 = 0$, and $z_1^1 = 1$. For the formula $\neg z^3 U z^2$, the system satisfies this if either $z_0^2 = 1$, or $z_0^2 = 0, z_0^3 = 0$, and $z_1^2 = 1$. Observe that z_0^2 appears with opposite negation status in the two temporal logic formulas. Fig. 16 shows the LNF for this case.

Let $z^\pi = [z_0^1, z_0^2, z_0^3, z_1^1, z_1^2, z_1^3]^\top$, with each edge denoted by y_i and ω_i , $i = 1, \dots, 4$. The convex set constraints (8) are:

$$\begin{aligned} \omega_1 &\geq y_1 \cdot [1, 0, 0, 0, 0, 0]^\top \\ \omega_2 &\geq y_2 \cdot [0, 0, 0, 1, 0, 0]^\top \\ \omega_2 &\leq \mathbf{1}_6 - y_2 \cdot [1, 1, 0, 0, 0, 0]^\top \\ \omega_3 &\geq y_3 \cdot [0, 1, 0, 0, 0, 0]^\top \\ \omega_4 &\geq y_4 \cdot [0, 0, 0, 0, 1, 0]^\top \\ \omega_4 &\leq \mathbf{1}_6 - y_4 \cdot [0, 1, 1, 0, 0, 0]^\top \end{aligned}$$

The flow conservation constraints (10), (11) are:

$$\begin{aligned} 1 &= y_1 + y_2 = y_3 + y_4 \\ z^\pi &= \omega_1 + \omega_2 = \omega_3 + \omega_4 \end{aligned}$$

By applying F-M elimination to the flow conservation constraint $\omega_1 + \omega_2 = \omega_3 + \omega_4$, we substitute the lower bounds to one side and the upper bounds to the other side. This generates the two inequality constraints in (14):

$$\begin{aligned} y_1 \cdot [1, 0, 0, 0, 0, 0]^\top + y_2 \cdot [0, 0, 0, 1, 0, 0]^\top \\ \leq \mathbf{1}_6 - y_4 \cdot [0, 1, 1, 0, 0, 0]^\top \\ y_3 \cdot [0, 1, 0, 0, 0, 0]^\top + y_4 \cdot [0, 0, 0, 0, 1, 0]^\top \\ \leq \mathbf{1}_6 - y_2 \cdot [1, 1, 0, 0, 0, 0]^\top \end{aligned}$$

The only non-trivial inequality comes from examining the second component (corresponding to $z_0^2 = 0$) in the second inequality:

$$y_3 \leq 1 - y_2 \quad (46)$$

Constraint (46) requests that we cannot simultaneously select edge 2 (which requires $z_0^2 = 0$) and edge 3 (which requires $z_0^2 = 1$).

This example shows that when predicates appear with different negation statuses, combining flow conservation constraints (10b) with convex set constraints (8) can generate non-trivial inequalities.

E Fourier-Motzkin Elimination for GCS Formulation of Minimum-Time Linear Control

In this appendix, we provide an example demonstrating how the proposed F-M elimination process can be applied to simplify GCS formulations for problems beyond temporal logic planning. We illustrate this by applying the F-M elimination to the minimum-time control problem for discrete-time linear systems with double integrator dynamics, following the example from Chapter 10.1 of (Marcucci 2024). Consider the discrete-time linear dynamical system:

$$\mathbf{s}_{k+1} = \mathbf{A}\mathbf{s}_k + \mathbf{B}\mathbf{a}_k \quad (47)$$

where $\mathbf{s}_k \in \mathbb{R}^n$ and $\mathbf{a}_k \in \mathbb{R}^m$ are the system state and control action at time step $k \in \mathbb{Z}_{\geq 0}$. For the double integrator dynamics with discretization step 0.01, the system matrices are:

$$\mathbf{A} = \begin{bmatrix} 1 & 0.01 \\ 0 & 1 \end{bmatrix}, \quad \mathbf{B} = \begin{bmatrix} 0 \\ 0.01 \end{bmatrix} \quad (48)$$

Given initial conditions $\mathbf{s}_0 = \hat{\mathbf{s}}$, the goal is to drive the system to a target set $\mathcal{T} = \{0\}$ (origin) in the minimum number of time steps $k \leq \bar{K}$, subject to constraints $(\mathbf{s}_k, \mathbf{a}_k) \in \mathcal{D}$ where \mathcal{D} is a compact convex set. For this problem, we specify \mathcal{D} by element-wise bounds $\mathbf{s}_{\text{lb}} \leq \mathbf{s}_k \leq \mathbf{s}_{\text{ub}}$ and $\mathbf{a}_{\text{lb}} \leq \mathbf{a}_k \leq \mathbf{a}_{\text{ub}}$, where $\mathbf{s}_{\text{lb}}, \mathbf{s}_{\text{ub}} \in \mathbb{R}^n$ and $\mathbf{a}_{\text{lb}}, \mathbf{a}_{\text{ub}} \in \mathbb{R}^m$.

Following (Marcucci 2024), the GCS formulation constructs a graph with vertices $\mathcal{V} = \{0, 1, \dots, \bar{K} - 1, t\}$ where each vertex $v = 0, \dots, \bar{K} - 1$ has outgoing edges to vertex $v + 1$ and to the target vertex t . The formulation introduces binary edge variables $y_e \in \{0, 1\}$ indicating if edge e is traversed, and continuous variables representing state-control pairs $(\mathbf{s}_v, \mathbf{a}_v) \in \mathcal{D}$ at each vertex, with the state $\mathbf{s}_0 = \hat{\mathbf{s}}$ at the source vertex and $\mathbf{s}_t \in \mathcal{T}$ at the target vertex t . Figure 17 illustrates this graph structure.

The complete GCS formulation is:

$$\text{minimize} \quad 1 + \sum_{k=0}^{\bar{K}-2} y_k \quad (49a)$$

$$\text{s.t.} \quad y_0 + y'_0 = 1 \quad (49b)$$

$$y_{\bar{K}-1} = 0 \quad (49c)$$

$$\forall k = 0, \dots, \bar{K} - 2 : \quad (49d)$$

$$y_{k+1} + y'_{k+1} = y_k \quad (49e)$$

$$\sigma_0 + \sigma'_0 = \hat{\mathbf{s}} \quad (49f)$$

$$\forall k = 0, \dots, \bar{K} - 1 : \quad (49g)$$

$$y_k \mathbf{s}_{\text{lb}} \leq \sigma_k \leq y_k \mathbf{s}_{\text{ub}}$$

$$y_k \mathbf{a}_{\text{lb}} \leq \alpha_k \leq y_k \mathbf{a}_{\text{ub}}$$

$$y'_k \mathbf{s}_{\text{lb}} \leq \sigma'_k \leq y'_k \mathbf{s}_{\text{ub}}$$

$$y'_k \mathbf{a}_{\text{lb}} \leq \alpha'_k \leq y'_k \mathbf{a}_{\text{ub}}$$

$$\forall k = 0, \dots, \bar{K} - 2 :$$

$$\mathbf{A}\sigma_k + \mathbf{B}\alpha_k = \sigma_{k+1} + \sigma'_{k+1} \quad (49h)$$

$$\forall k = 0, \dots, \bar{K} - 1 :$$

$$\mathbf{A}\sigma'_k + \mathbf{B}\alpha'_k = 0 \quad (49i)$$

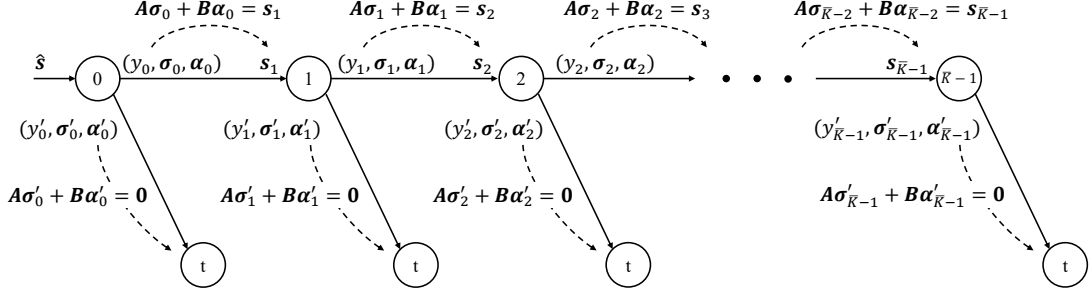


Figure 17. GCS representation for minimum-time control. The graph structure shows vertices $\{0, 1, \dots, \bar{K} - 1, t\}$ with edge variables y_k and y'_k , flow variables $\sigma_k, \alpha_k, \sigma'_k, \alpha'_k$, initial state \hat{s} at vertex 0, and target state at vertex t .

where y_k is the edge variable from vertex k to vertex $k + 1$, y'_k is the edge variable from vertex k to the target vertex t . The variables σ_k, α_k are the state and control flow variables paired with y_k , while σ'_k, α'_k are the state and control flow variables paired with y'_k . The actual system state and control at time step k are reconstructed as:

$$(s_k, a_k) = (\sigma_k, \alpha_k) + (\sigma'_k, \alpha'_k) \quad (50)$$

For comparison, the baseline formulation used by (Marcucci 2024) is:

$$\text{minimize} \quad 1 + \sum_{k=0}^{\bar{K}-2} y_k \quad (51a)$$

$$\text{s.t.} \quad s_0 = \hat{s} \quad (51b)$$

$$s_{\bar{K}} = \mathbf{0} \quad (51c)$$

$$a_{lb} \leq a_0 \leq a_{ub} \quad (51d)$$

$$\forall k = 1, \dots, \bar{K} - 2 : \quad (51d)$$

$$y_{k-1}s_{lb} \leq s_k \leq y_{k-1}s_{ub}$$

$$y_{k-1}a_{lb} \leq a_k \leq y_{k-1}a_{ub}$$

$$\forall k = 0, \dots, \bar{K} - 1$$

$$s_{k+1} = As_k + Ba_k \quad (51e)$$

While GCS achieves tighter convex relaxations than the baseline formulation, this advantage comes at the cost of additional flow variables. These extra variables offset the benefits of tighter relaxations, resulting in no computational speed improvement over the baseline for this problem. However, by applying F-M elimination, we can remove the flow variables from the GCS formulation while preserving the relaxation tightness, resulting in a formulation with nearly the same number of variables as the baseline but with tighter convex relaxations.

Since this problem involves linear dynamics as described in (47), the flow conservation constraints propagate the dynamics through the network flow structure via equations (49f) and (49g). However, eliminating the flow variables would disrupt this dynamic propagation. To preserve the dynamic propagation, we reintroduce state and control variables s_k and a_k that satisfy the dynamics (47) and their bounds (51d). The state variables are labeled at each vertex in Fig. 17.

Starting with $k = 0$, we systematically eliminate the flow variables $\sigma_0, \alpha_0, \sigma'_0$, and α'_0 . The constraints involving these variables include the initial state constraint (49d),

the dynamics constraints (49f) and (49g) at $k = 0$, and the convex bounds (49e) at $k = 0$. Since the dynamics constraints naturally involve $A\sigma_0, B\alpha_0, A\sigma'_0$, and $B\alpha'_0$, we multiply the bounds by A or B accordingly to align with these compound terms. This multiplication preserves inequality directions for the double integrator system since all elements of A and B are non-negative. The resulting aligned constraints are:

$$A\sigma_0 + A\sigma'_0 = A\hat{s} \quad (52a)$$

$$A\sigma_0 + B\alpha_0 = s_1 \quad (52b)$$

$$A\sigma'_0 + B\alpha'_0 = \mathbf{0} \quad (52c)$$

$$y_0 As_{lb} \leq A\sigma_0 \leq y_0 As_{ub} \quad (52d)$$

$$y'_0 As_{lb} \leq A\sigma'_0 \leq y'_0 As_{ub} \quad (52e)$$

$$y_0 Ba_{lb} \leq B\alpha_0 \leq y_0 Ba_{ub} \quad (52f)$$

$$y'_0 Ba_{lb} \leq B\alpha'_0 \leq y'_0 Ba_{ub} \quad (52g)$$

We begin by canceling out σ_0 . Applying the standard F-M procedure, all lower and upper bounds for $A\sigma_0$ from the aligned constraints are enumerated, then valid inequalities are generated by requiring each lower bound to be less than or equal to each upper bound. This process yields the following non-trivial constraints:

$$y_0 As_{lb} + A\sigma'_0 \leq A\hat{s} \quad (53a)$$

$$y_0 As_{lb} \leq s_1 - B\alpha_0 \quad (53b)$$

$$A\hat{s} - A\sigma'_0 \leq y_0 As_{ub} \quad (53c)$$

$$A\hat{s} - A\sigma'_0 \leq s_1 - B\alpha_0 \quad (53d)$$

$$s_1 - B\alpha_0 \leq y_0 As_{ub} \quad (53e)$$

$$s_1 - B\alpha_0 \leq A\hat{s} - A\sigma'_0 \quad (53f)$$

Next, we eliminate α_0 using the constraints from (53) along with the convex bounds (52f) for $B\alpha_0$. Applying F-M elimination gives the following non-trivial constraints:

$$y_0 Ba_{lb} - A\sigma'_0 \leq Ba_0 \quad (54a)$$

$$Ba_0 \leq -A\sigma'_0 + y_0 Ba_{ub} \quad (54b)$$

Following that, we remove σ'_0 using the constraints from (54) along with the convex bounds (52e) and the dynamics constraint (52c). Applying F-M elimination gives the following non-trivial constraints:

$$y'_0 As_{lb} + Ba_0 \leq y_0 Ba_{ub} \quad (55a)$$

$$y'_0 As_{lb} \leq -B\alpha'_0 \quad (55b)$$

Table 7. Minimum-time control for double integrator on 63 initial conditions

Formulation	Variables (Binary, Continuous)	Constraints	Relaxation Gap (%) Mean [Min, Max]	Solving Time (s) Mean [Max]
GCS (49)	(500, 1500)	4251	33.4 [4.1, 64.8]	0.32 [2.27]
F-M Simplified GCS (57)	(500, 752)	2499	33.5 [4.1, 64.8]	0.08 [0.45]
Baseline (51)	(250, 752)	1994	40.7 [19.1, 68.5]	0.07 [0.78]

$$\begin{aligned}
\mathbf{A}\hat{\mathbf{s}} - y_0\mathbf{A}\mathbf{s}_{\text{ub}} &\leq -\mathbf{B}\boldsymbol{\alpha}'_0 & (55\text{c}) \\
y_0\mathbf{B}\mathbf{a}_{\text{lb}} &\leq \mathbf{B}\mathbf{a}_0 + y'_0\mathbf{A}\mathbf{s}_{\text{ub}} & (55\text{d}) \\
y_0\mathbf{B}\mathbf{a}_{\text{lb}} &\leq \mathbf{B}\mathbf{a}_0 - \mathbf{B}\boldsymbol{\alpha}'_0 & (55\text{e}) \\
-\mathbf{B}\boldsymbol{\alpha}'_0 &\leq y'_0\mathbf{A}\mathbf{s}_{\text{ub}} & (55\text{f}) \\
-\mathbf{B}\boldsymbol{\alpha}'_0 &\leq \mathbf{A}\hat{\mathbf{s}} - y_0\mathbf{A}\mathbf{s}_{\text{lb}} & (55\text{g}) \\
-\mathbf{B}\boldsymbol{\alpha}'_0 + \mathbf{B}\mathbf{a}_0 &\leq y_0\mathbf{B}\mathbf{a}_{\text{ub}} & (55\text{h})
\end{aligned}$$

Among these inequalities, constraints (55a) and (55d) are valid inequalities for the final formulation.

Finally, we eliminate $\boldsymbol{\alpha}'_0$ from (55) (other than (55a) and (55d)) along with the convex bounds (52g). F-M gives two additional valid inequalities:

$$\mathbf{A}\hat{\mathbf{s}} + y'_0\mathbf{B}\mathbf{a}_{\text{lb}} \leq y_0\mathbf{A}\mathbf{s}_{\text{ub}} \quad (56\text{a})$$

$$y_0\mathbf{A}\mathbf{s}_{\text{lb}} \leq \mathbf{A}\hat{\mathbf{s}} + y'_0\mathbf{B}\mathbf{a}_{\text{ub}} \quad (56\text{b})$$

Constraints (56a) and (56b), together with (55a), and (55d), form the complete set of valid inequalities that tightens the formulation for $k = 0$.

Following an identical pattern, we repeat this elimination process to remove flow variables $\boldsymbol{\sigma}_k$, $\boldsymbol{\alpha}_k$, $\boldsymbol{\sigma}'_k$, and $\boldsymbol{\alpha}'_k$ for $k = 1, 2, \dots, \bar{K} - 1$. After completing the elimination at all time steps, we obtain the F-M simplified GCS formulation:

$$\begin{aligned}
\text{minimize} \quad & 1 + \sum_{k=0}^{\bar{K}-2} y_k \\
\text{s.t.} \quad & y_0 + y'_0 = 1 & (57\text{a}) \\
& y_{\bar{K}-1} = 0 & (57\text{b}) \\
& \forall k = 0, \dots, \bar{K} - 2 : \\
& \quad y_{k+1} + y'_{k+1} = y_k & (57\text{c}) \\
& \quad s_0 = \hat{\mathbf{s}}, \quad s_{\bar{K}} = \mathbf{0} & (57\text{d}) \\
& \quad \mathbf{a}_{\text{lb}} \leq \mathbf{a}_0 \leq \mathbf{a}_{\text{ub}} & (57\text{e}) \\
& \quad \forall k = 1, \dots, \bar{K} - 2 : \\
& \quad y_{k-1}\mathbf{s}_{\text{lb}} \leq \mathbf{s}_k \leq y_{k-1}\mathbf{s}_{\text{ub}} & (57\text{f}) \\
& \quad y_{k-1}\mathbf{a}_{\text{lb}} \leq \mathbf{a}_k \leq y_{k-1}\mathbf{a}_{\text{ub}} & (57\text{g}) \\
& \quad \forall k = 0, \dots, \bar{K} - 1 : \\
& \quad s_{k+1} = \mathbf{A}\mathbf{s}_k + \mathbf{B}\mathbf{a}_k & (57\text{h}) \\
& \quad \forall k = 0, \dots, \bar{K} - 1 : \\
& \quad y'_k\mathbf{A}\mathbf{s}_{\text{lb}} + \mathbf{B}\mathbf{a}_k \leq y_k\mathbf{B}\mathbf{a}_{\text{ub}} & (57\text{i}) \\
& \quad y_k\mathbf{B}\mathbf{a}_{\text{lb}} \leq y'_k\mathbf{A}\mathbf{s}_{\text{ub}} + \mathbf{B}\mathbf{a}_k & (57\text{j}) \\
& \quad \mathbf{A}\mathbf{s}_k + y'_k\mathbf{B}\mathbf{a}_{\text{lb}} \leq y_k\mathbf{A}\mathbf{s}_{\text{ub}} & (57\text{k}) \\
& \quad y_k\mathbf{A}\mathbf{s}_{\text{lb}} \leq \mathbf{A}\mathbf{s}_k + y'_k\mathbf{B}\mathbf{a}_{\text{ub}} & (57\text{l})
\end{aligned}$$

Comparing (57) with the baseline (51), we observe that the network flow structure used by GCS effectively introduces constraints (57c) and (57h)–(57k) that tighten the formulation upon the baseline. During our tests, we

find that the tightening effect of constraints (57h)–(57k) is minimal, hence we exclude them from our experimental formulation. The major tightening effect comes from (57c), which implicitly enforces the valid inequality $y_{k+1} \leq y_k$. Through F-M elimination, we obtain (57), a formulation equivalent to (49) but with significantly fewer variables and constraints.

We use Gurobi 12.0 to run 63 experiments on a grid of initial conditions spanning positions from -0.8 to 0.8 (at 0.2 intervals), velocities from -0.75 to 0.75 (at 0.25 intervals), and time horizon $\bar{K} = 250$. We compare the GCS (49), F-M simplified GCS (57), and baseline (51) formulations. The results are shown in Table 7. F-M simplified GCS achieves a 33.5% mean relaxation gap, nearly identical to the original GCS formulation's 33.4%, with the 0.1% difference attributable to excluding the tightening constraints (57h)–(57k). The baseline formulation exhibits a substantially weaker mean relaxation gap of 40.7%. The number of continuous variables in (57) is identical to the baseline (51), and significantly less than the original GCS. The additional constraints (57c) increase the number of constraints over the baseline. In terms of computation time, the F-M simplification increases the solving time over the original GCS. While the average solving time for the F-M simplified formulation is comparable to the baseline, the maximum solving time is less.

Our F-M procedure presented in this appendix has limitations. It requires that the state matrices \mathbf{A} and \mathbf{B} contain only non-negative elements, and that the convex bounds (49e) can be easily written to isolate the flow variables. These conditions do not hold for the general class of GCS formulations, though coordinate transformations might extend applicability in some cases. When these conditions are satisfied, we have a pipeline to identify strong valid inequalities for the specific problem class: starting with GCS to obtain tight convex relaxations, then applying F-M elimination to remove the flow variables.

F Soundness and Completeness

In this appendix, we provide soundness and completeness guarantees for our LNF formulation. For all proofs presented, we assume that the temporal logic specifications can be expressed in disjunctive normal form: $\varphi = \bigvee_{m=1}^M \bigwedge_{n=1}^{N_m} \pi_{m,n}$, where $\pi_{m,n}$ represents a possibly negated predicate. This is a standard assumption, as any propositional logic formula can be converted to this form through iterative application of distributivity and De Morgan's laws (Jackson and Sheridan 2004).

F.1 Soundness

Theorem 4. *If the complete formulation returns solution $(\xi, \mathbf{y}, \mathbf{z}^\pi)$, then the solution \mathbf{z}^π satisfies the temporal logic formula φ , the solution ξ satisfies the underlying system dynamics, and the combination of them satisfies the atomic predicate constraint (3).*

Proof. Let $\varphi = \bigvee_{m=1}^M \bigwedge_{n=1}^{N_m} \pi_{m,n}$. For a formula in this form, satisfaction requires that at least one of the conjunctive clauses $\bigwedge_{n=1}^{N_m} \pi_{m,n}$ must be satisfied. In our LNF formulation, constraint (16a) ensures exactly one path (corresponding to one conjunctive clause) is selected.

When a specific path m is selected (i.e., $y_m = 1$), all predicates in the corresponding conjunctive clause must be satisfied. For each non-negated predicate $\pi_j \in P_m$, constraint (16b) enforces $z^{\pi_j} = 1$ since y_m appears on the right-hand side. Similarly, for each negated predicate $\neg\pi_j \in P_m$, constraint (16c) ensures $z^{\pi_j} = 0$.

For paths not selected (i.e., $y_m = 0$), (16d) prevents all predicates in P_m from being simultaneously satisfied, as this would make the right-hand side equal to 1.

Finally, (16e) guarantees that the underlying dynamics and atomic predicates are satisfied.

F.2 Completeness

We show that our planner is complete, meaning it always finds the optimal solution when one exists.

Theorem 5. *If there exists a feasible trajectory satisfying the temporal logic constraint, it corresponds to a set of feasible solutions $(\xi, \mathbf{y}, \mathbf{z}^\pi)$ of the optimization formulation.*

Proof. Let $\varphi = \bigvee_{m=1}^M \bigwedge_{n=1}^{N_m} \pi_{m,n}$. Assume there exists a feasible solution ξ that satisfies one of the conjunctive subformulas $\bigwedge_{n=1}^{N_m} \pi_{m,n}$ for some specific m , hence satisfying φ . We construct \mathbf{z}^π as follows. For each atomic predicate $\pi_j \in \Pi$ and each time step k , define $z^{\pi_j}_k = 1$ if and only if $(\mathbf{a}^{\pi_j})^\top \mathbf{x}_k + b^{\pi_j} \geq 0$, and $z^{\pi_j}_k = 0$ otherwise. This uniquely determines \mathbf{z}^π based on the trajectory ξ .

We show that there exist \mathbf{y} satisfying constraints (16a), (16b), and (16c). Set $y_m = 1$ for the specific m corresponding to the satisfied conjunction, and all other y_m 's to 0. This construction immediately satisfies (16a) since $\sum_{m=1}^M y_m = 1$.

For constraint (16b), consider any non-negated predicate $\pi_j \in P_m$. Since ξ satisfies the conjunction containing π_j , we have $z^{\pi_j}_k = 1$ by the construction of \mathbf{z}^π . The right-hand side of (16b) equals 1. Thus (16b) is satisfied. A similar argument holds for (16c).

For other edges m such that $y_m = 0$, constraints (16b) and (16c) are trivially satisfied as they reduce to $z^{\pi_j}_k \geq 0$ and $z^{\pi_j}_k \leq 1$, respectively.

Since our formulation is a mixed-integer program solved with Branch-and-Bound, the solver guarantees finding this feasible solution.

Theorem 6. *If there exists an optimal trajectory satisfying the temporal logic constraint, it corresponds to a set of optimal solutions $(\xi^*, \mathbf{y}^*, \mathbf{z}^{\pi^*})$ of the optimization formulation.*

Proof. In the proof of Theorem 5, we have already shown that any solution of ξ^* with uniquely determined \mathbf{z}^{π^*} corresponds to (potentially more than one) set of feasible \mathbf{y} 's. Therefore, this theorem is evident since the objective function is independent of \mathbf{y} .